

DOCTOR THESIS

Development of a 100-W Nd:YAG laser
using the injection locking technique
for gravitational wave detectors

Kohei Takeno

January, 2006

Contents

1	Introduction	1
1.1	Gravitational wave detection	2
1.2	Gravitational wave detectors	2
1.2.1	Bar detectors	3
1.2.2	Interferometric gravitational wave detectors	3
1.3	Gravitational wave detection projects	5
1.4	The Japanese next-generation project: LCGT	6
1.4.1	Design of the LCGT interferometer	7
1.4.2	Sensitivity of LCGT	10
1.4.3	Specifications of the LCGT laser	10
1.4.4	Key techniques for the LCGT laser	15
1.4.5	Design of the LCGT laser	16
1.5	Goal of this work	18
1.6	Other high-power, single-frequency lasers	19
1.6.1	Lasers in the current detectors	19
1.6.2	Historical aspect of the development of single-frequency lasers	20
1.7	Other frequency stabilization experiments	21
2	Development of a slave laser	25
2.1	Theoretical background	25
2.1.1	Laser oscillation	25
2.1.2	Stability condition of laser oscillation	27
2.1.3	Thermal distortion and compensation	27
2.2	How to construct a slave laser	29
2.3	Side-pumped Nd:YAG laser module	30
2.4	Preliminary experiment in a linear cavity configuration	31
2.4.1	Design of the linear cavity	31
2.4.2	Results of the linear cavity operation	33
2.5	Design of a slave cavity	33
2.5.1	Ring cavity configuration	33
2.5.2	Results of the ring oscillation and discussions	34
2.6	Unidirectional operation with an intracavity Faraday rotator	37
2.6.1	Experimental setup	37
2.6.2	Characterization of the output	38

2.6.3	Beam propagation profile measurements	39
2.6.4	Relative intensity noise measurement	39
2.7	Discussions	39
2.7.1	Output power	39
2.7.2	Spatial beam quality	39
2.7.3	Polarization	41
2.7.4	Intensity noise	41
2.8	Summary	42
3	Injection locking	43
3.1	Theoretical model of injection locking	43
3.1.1	Master equations	43
3.1.2	Locking range	44
3.1.3	Frequency stability in injection locking	46
3.1.4	Intensity stability in injection locking	47
3.1.5	Pound-Drever-Hall technique	47
3.1.6	Control theory in injection locking using the PDH technique	48
3.1.7	Estimation of frequency stability of an optical cavity	50
3.1.8	Characterization of a spatial mode using a Shack-Hartmann wavefront sensor	50
3.2	Experimental setup of injection locking	52
3.3	Transfer function of stabilization loop with the PDH technique	53
3.4	Frequency spectrum of the injection-locked laser	57
3.5	Output power	58
3.6	Beam quality	60
3.6.1	M^2 measurement	60
3.6.2	Spatial profile	60
3.6.3	Spatial mode analysis with a Shack-Hartmann wavefront sensor	63
3.6.4	Polarization	63
3.7	Intensity stability	66
3.8	Stability of the slave laser cavity	67
3.9	Discussions	68
3.9.1	Injection locking system	68
3.9.2	Output power	68
3.9.3	Beam quality	69
3.9.4	Polarization	70
3.9.5	Intensity stability	70
3.9.6	Frequency characteristics	71
3.10	Summary	71
4	Frequency stabilization	73
4.1	Theoretical model of frequency stabilization	73
4.2	Purpose of frequency stabilization in this work	74
4.3	PMC	76
4.3.1	Cavity design	76
4.3.2	Preliminary tests with the PMC using the master laser	77

4.4	Experiment	80
4.4.1	Experimental setup	80
4.4.2	PDH signal	83
4.4.3	Transmittance of the PMC	84
4.4.4	Transfer function of the feedback loop	87
4.4.5	Frequency stability of the injection-locked laser	88
4.4.6	Expected frequency stability	89
4.4.7	Frequency stability of the master laser	90
4.4.8	Frequency noise spectra for s and p polarization	91
4.5	Discussions	92
4.5.1	Mode cleaning effect of the PMC	92
4.5.2	Frequency stability of the injection-locked laser	92
4.5.3	Possibility for application of the PMC in LCGT	93
4.6	Summary	94
5	Conclusions	95
5.1	Conclusions	95
5.2	Future work	96
A	Other possible light sources for future detectors	97
A.1	Factors to determine the laser configuration	97
A.2	Laser materials	98
A.2.1	Nd-doped materials	98
A.2.2	Yb-doped materials	99
A.2.3	Ceramic materials	99
A.2.4	Diode lasers	99
A.3	Laser configurations	100
A.3.1	Rod lasers	100
A.3.2	Slab lasers	100
A.3.3	Disc lasers	100
A.3.4	Fiber system	100
A.4	Discussion	101
A.5	Conclusion	101
B	Formulas of noise in LCGT	103
B.1	Seismic noise	103
B.2	Thermal noise	103
B.3	Shot noise	104
B.4	Radiation pressure noise	105
	Bibliography	117

Chapter 1

Introduction

Since the first demonstration of laser oscillation in 1960¹⁾, there has been remarkable progress in development of lasers, such as advent of high-power diode lasers with excellent beam quality and long lifetime, short-pulse lasers with high peak power, which are applicable for investigation of non-linear effects, and a variety of fiber lasers, which have the advantages of flexibility and compactness. The coherence property of laser beams has promoted development in the field of solid-state physics, astrophysics, remote communications, medical treatment and industrial processing.

This work is aiming for producing a high-power, continuous-wave radiation at a single frequency with a Nd:YAG laser system, which will be used in a Japanese gravitational wave detection project. Although extensive studies on lasers have been made to date, it is still challenging to build a single-frequency light source required for interferometric detectors. This is because interaction of gravitational waves with matter is so weak that an extremely high-performance laser is required for detectors to reveal its small effects.

Scaling the output power of lasers without degradation of beam quality is the key to building a laser for gravitational wave detectors. In this work, injection locking is the essential technique to scale the output power to 100 W while retaining good beam quality and single frequency property. Detailed description of the construction process of a 100-W, single-frequency laser is given in this thesis, including the theoretical models on which it is based.

In Chapter 1, I will introduce the background of this work and describe the Japanese gravitational wave detection project in which I am involved. In Chapter 2, development of a slave laser for injection locking will be presented. Building high-power lasers is often hindered by degradation of beam quality caused by thermal birefringence and thermal lensing. The results of characterization of the slave laser output will be given in this chapter. In Chapter 3, description of an injection locking system will be given. I have succeeded in generating a 100-W, single-frequency output through injection locking. In Chapter 4, the frequency stabilization experiment of an injection-locked laser will be described. In this chapter, I will discuss the frequency performance of the injection-locked laser. Finally, I will summarize the development of a high-power laser system in Chapter 5. Examination of problems to be solved in the future will be given in this chapter.

The first section in each chapter will give theoretical background of techniques which were used in the described experiments. Additional discussions concerning the possible light sources for gravitational wave detectors and formulas of interferometer sensitivity are given in the Appendix.

1.1 Gravitational wave detection

Detecting a gravitational wave is one of the most exciting topics in physics. A gravitational wave is a small ripple of spacetime, which appears as small displacement of distance^{2,3)}. If a gravitational wave reaches a detector, the proper distance in one direction shrinks, while it expands in the orthogonal direction; in other words, a gravitational wave is quadrupole radiation and changes the metric of spacetime in a differential manner in the orthogonal directions. A theoretical model predicts that there are two independent polarization states for a gravitational wave, as shown in Figure 1.1: the cross mode and plus mode, which are rotated by 45° relative to each other.

Gravitational waves are emitted when a mass accelerates, which is analogous to the radiation of electromagnetic waves from an accelerated charged particle. The amplitude of a gravitational wave is evaluated as a strain $h = \delta l/l$, where δl is the displacement caused by a gravitational wave and l is the length which we are monitoring. The root-mean-square (rms) amplitude of a gravitational wave from a neutron binary system at 200 Mpc* is estimated to be in the order of $h = 10^{-21}$, or equivalently a 10^{-9} nm displacement to 1-km length; this estimation shows that a gravitational wave causes an extremely small effect. Thus, radiation of gravitational waves with practically observable amplitude on the earth can be expected only from violent astronomical phenomena, such as super novae or coalescence of neutron binary stars.

The existence of a gravitational wave was indirectly proved by observing change in the orbital period of the binary pulsar PSR1913+16^{4,5)}, which was in good agreement with a theoretical prediction using the assumption that energy was dissipated by gravitational radiation.

However, despite all efforts to detect a gravitational wave throughout the world, no gravitational wave has been directly detected. This is due to the sensitivity of currently operating detectors being limited by noises at sensitivity levels above the expected signal levels of a gravitational wave, and thus the analysis of experimental data collected with the detectors cannot conclude without ambiguity whether there is no gravitational wave radiation reaching the detector or the gravitational wave signal was just concealed by noise.

The detection of gravitational waves is expected to open a new channel to look at the universe because it conveys to us totally new information concerning astronomical events, which has not been accessed by conventional methods of observing through electromagnetic waves. Detection of gravitational waves will lead to the beginning of gravitational wave astronomy.

Since it is possible to determine the position of a radiation source only when more than three detectors detect a gravitational wave, it is preferable that there are many detectors of the same sensitivity widespread over the world.

1.2 Gravitational wave detectors

In order to detect tiny displacements caused by gravitational waves, two approaches are suggested and investigated: one is a resonant bar detector, which uses elastic oscillation of a massive metal rod or sphere; the other is a large-scale Michelson interferometer, which monitors the arm length and will capture a gravitational wave as perturbation to the arm length.

*1 pc is a distance equal to 3.26 light year.

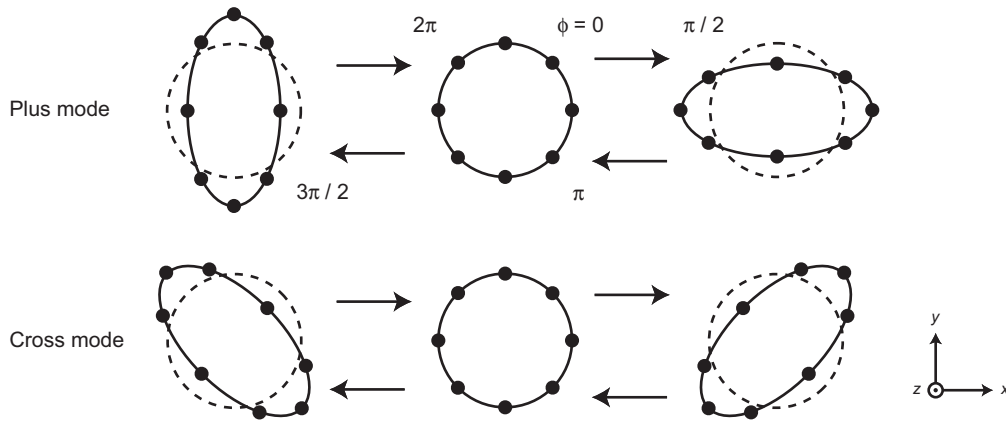


Figure 1.1: Polarization states of a gravitational wave. Filled circles show masses free from any external force except those exerted by a gravitational wave. If a gravitational wave is incident from the z direction, the proper distance between the masses changes as shown in this figure. ϕ is the phase of the incident gravitational wave.

1.2.1 Bar detectors

Detection of a gravitational wave using a resonant bar was first suggested as early as 1960s. The sensitivity of a resonant bar detector, for instance, has been improved to the level of $4 \times 10^{-22} \text{ Hz}^{-1/2}$ over a bandwidth of 2 Hz^6 ; although the bandwidth is limited, the sensitivity is comparable to those of interferometric detectors.

A bar detector consists of a massive aluminum alloy (\sim a few ton) with a high Q value (on the order of 10^6 or higher) and transducers to transform the vibration of the mass caused by a gravitational wave into an electrical signal. A gravitational wave excites one of the vibrational modes of the resonant bar if the frequency falls within the detector bandwidth. Since the high sensitivity of the detector is limited within a few hertz bandwidth in the range of a few kilo-hertz,[†] the target source of the gravitational wave radiation is limited to those which match the resonant frequency.

Several schemes are taken to improve the sensitivity; first, the mass is suspended and isolated from seismic noise. Second, thermal noise is reduced by cooling down to a cryogenic temperature. Also efforts are devoted to improve transducers, for instance, by using double-stage SQUID amplifiers.

1.2.2 Interferometric gravitational wave detectors

The other way to detect a gravitational wave is a large-scale Michelson interferometer. A schematic view of an interferometric detector is shown in Figure 1.2. The light from the laser is split by a beam-splitter and two separated beams travel along each arm, then reflected back by the mirror and combined again at the beamsplitter. If a gravitational wave arrives, the optical path length of the arms is changed in the opposite sign to each other, thus a gravitational wave signal appears in the interference pattern

[†]This bandwidth is mainly determined by amplifier noise, not by the resonance itself.

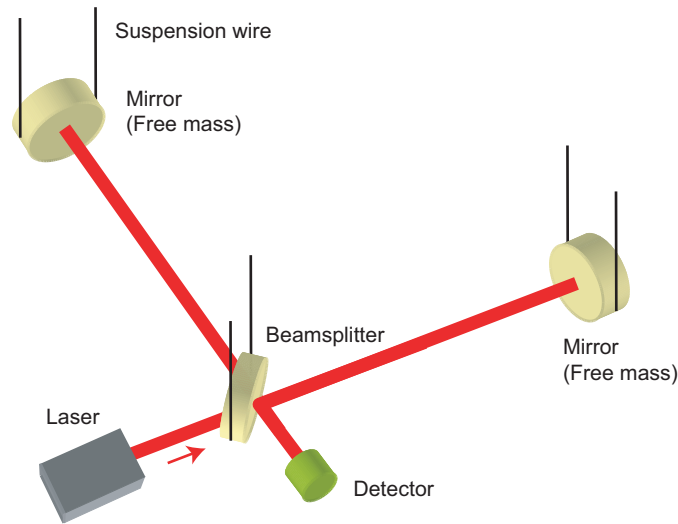


Figure 1.2: Schematic view of a Michelson interferometer as a gravitational wave detector. Mirrors are suspended to isolate from the ground vibration and act as a free mass above the resonant frequency of the pendulum.

and can be detected at the output port of the Michelson interferometer.

As indicated in Figure 1.2, each mirror is suspended by a pendulum to act as a free mass[‡] above the resonant frequency of the suspension system. A typical resonant frequency of a suspension system is a few hertz. Since lower resonant frequency can extend the frequency region over which the mass can act as a free mass, various attempts have been made to pull down the resonant frequency to several hundred milli-hertz^{7,8}).

In detecting a gravitational wave with an interferometric detector, the sensitivity is limited by the following noises:

- Seismic noise
- Thermal noise of mirrors
- Thermal noise of suspensions
- Shot noise
- Radiation pressure noise

Although a suspension system functions as an isolator of seismic noise, the vibration noise from surrounding environment can be detected by the interferometer due to the high sensitivity. Thermally excited vibration of mirrors and suspensions also limits the sensitivity. Since the thermal noise is determined by mechanical loss of mirrors or suspensions, a material with high Q , such as sapphire or fused silica, is used for the interferometer components.

[‡]“Free mass” means that there is no force to swing the mirror except for a gravitational wave.

When seismic noise and thermal noise are suppressed, next comes the theoretical limit given by shot noise and radiation pressure noise. These noises are originated from the particle nature of photons and brought by the optical signal itself; hence, it cannot be eliminated by any means. Since the optical power of lasers in current gravitational wave detectors is not high enough to disclose the effect of the radiation pressure, our concern is mainly focused on shot noise for improving the sensitivity.

The shot noise in a simple Michelson interferometer[§] can be evaluated according to the formula³⁾

$$\delta\phi_{\min} = \sqrt{\frac{2e}{P_{\max}}} \frac{1}{\sin(\Phi_0/2)}, \quad (1.1)$$

where $\delta\phi_{\min}$ is the minimum detectable phase fluctuation determined by the shot noise, e is the elementary charge, P_{\max} is the maximum power at the output port on the constructive interference condition and Φ_0 is the phase at the operating point of the interferometer. According to Equation (1.1), the detectable phase fluctuation is minimized for a condition of $\Phi_0 = \pi$. Under this condition, the lights combined at the beamsplitter destructively interfere: hence it is referred to as the dark fringe condition. Because of the requirement to minimize the shot noise, all interferometric detectors are operated on the dark fringe condition.

1.3 Gravitational wave detection projects

Several research groups are attempting to realize the first detection of a gravitational wave using the interferometric scheme. Table 1.1 lists all interferometric gravitational wave detectors built in the world.

Project name	Country(ies)	Interferometer configuration	Arm length
TAMA	Japan	PRFPM	300 m
LIGO	U.S.A.	PRFPM	2km, 4km×2
VIRGO	France - Italy	PRFPM	3km
GEO 600	Germany - U.K.	Dual recycling	1.2 km
LCGT	Japan	PRFPM + RSE	3km ×2
Advanced LIGO	U.S.A.	PRFPM + D-RSE	4km

Table 1.1: Ground-based interferometric gravitational wave detectors in the world. The upper side shows the current detectors and the lower two rows show future detectors. PRFPM: Power-recycled Fabry-Perot Michelson interferometer, RSE: Resonant sideband extraction, D-RSE: Detuned RSE.

In the Japanese project, TAMA, is a 300-m-arm Michelson interferometer with power recycling that has already been built and developed^{8,9)}. Up to date, nine data-taking runs (DT1 - DT9) have been done to collect experimental data searching for gravitational waves and to verify the performance of the interferometer. Although there was no clear evidence for the detection of a gravitational wave in the collected data, the TAMA interferometer was operated with sensitivity of $h \sim 2 \times 10^{-21} \text{ Hz}^{-1/2}$,[¶] which

[§]The shot noise for LCGT (a Fabry-Perot Michelson interferometer with resonant sideband extraction) is given in Appendix B. Although the configuration considered here is simple, the dark fringe condition is still valid for advanced interferometers.

[¶]Here, h is a linear spectral density of the strain.

was sufficient to detect a gravitational wave from an event in our galaxy, or up to a distance of 72.8 kpc with a signal-to-noise ratio (SNR) of 10 for a binary system with 1.4 solar mass. During DT6 and DT8, TAMA achieved long-term observation of over 1000 hours. TAMA is now in the phase of hunting for noise sources and improving the sensitivity, including new suspension system which is being installed for better seismic isolation.

In the United States LIGO project, there are three interferometric detectors: two interferometers in Hanford with baseline of 2 km and 4 km, and one interferometer with baseline of 4 km in Livingston. The latest experimental results¹⁰⁾ show that the sensitivity of the 4-km interferometer in Hanford has reached $h = 5 \times 10^{-23} \text{Hz}^{-1/2}$ at 100 Hz, which is within the goal sensitivity of LIGO by a factor of 2. The observable distance is 7 Mpc with an SNR of 8. Currently the LIGO interferometer holds the world record of the detector sensitivity.

A collaborative research project between the Italian and French groups is called the VIRGO project^{11,12)}. In this project, a power-recycled Fabry-Perot Michelson interferometer with 3-km arms has been built and developed. Also, there is a joint project between Germany and the United Kingdom, named GEO 600^{13,14)}. GEO 600 is a Michelson interferometer with a dual recycling technique which utilizes the signal recycling technique together with power recycling.

Future detectors projects, large-scale cryogenic gravitational wave telescope (LCGT)^{7,15,16)} and Advanced LIGO¹⁷⁾, are improved versions of the current interferometers; next-generation interferometers are the key to detecting the first gravitational wave, or even further, to achieving a wider range of detection and revealing the details deep in the universe.

There are other projects aiming at gravitational wave detection in space; a European and American joint project called Laser Interferometric Space Antenna (LISA)^{18,19)} and the Japanese space detector project called Deci-hertz Interferometer Gravitational Wave Observatory (DECIGO)²⁰⁾. Both of the projects will launch space crafts equipped with optical components and form an interferometer in space rotating in an orbit around the sun. Since there is no seismic motion in space, low frequency region, at milli-hertz for LISA and deci-hertz for DECIGO, is the observation band. LISA plans to launch a test satellite, named the LISA Pathfinder¹⁹⁾, to investigate the feasibility of the technologies developed so far. DECIGO is now in the stage of designing and planning.

1.4 The Japanese next-generation project: LCGT

As mentioned above, the LCGT project plans to build advanced interferometers to detect gravitational waves. In the current design of LCGT, two power-recycled Fabry-Perot Michelson interferometers with resonant sideband extraction (RSE)^{16,21)} will be constructed in a tunnel of the Kamioka mine. The reason for building two detectors, not one, next to each other is to improve rejection of fake signals.

The Kamioka mine is located 37 km from the Sea of Japan. The interferometers will be built in a tunnel which will be drilled specifically for the LCGT project at 358 m above the sea level and 1000 m under the ground from the peak. Due to the hard, large mass of bedrock, the seismic motion is quiet compared to the TAMA site by two orders of magnitude.

LCGT plans to use cryogenic optical components, which are cooled down to 20 K, to reduce the thermal noise of the mirrors and the suspensions. A project, named cryogenic laser interferometer observatory (CLIO)²²⁾, has built a Michelson interferometer with baseline of 100 m at the Kamioka site and is verifying the feasibility of cooling mirrors and the effectiveness of thermal noise reduction.

Currently, LCGT is in the planning stage and applying for a budget to construct the interferometers. Development and verification of the essential techniques for LCGT are ongoing.

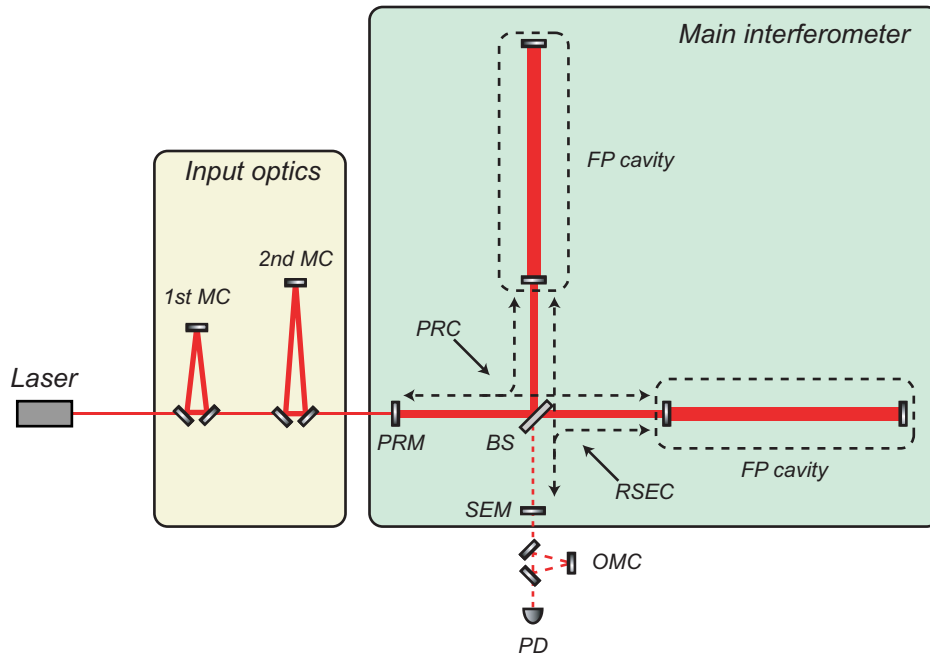


Figure 1.3: Schematic diagram of the interferometer in LCGT. The input optics consist of two mode cleaners. The main interferometer is composed of a FP cavity in each arm, a power-recycling mirror for power recycling and a signal-extraction mirror for resonant sideband extraction (RSE). MC; Mode cleaner, PRM: Power recycling mirror, BS: Beamsplitter, FP cavity: Fabry-Perot cavity, PRC: Power-recycling cavity, SEM: Signal extraction mirror, RSEC: RSE cavity, OMC: Output mode cleaner, PD: photodetector.

1.4.1 Design of the LCGT interferometer

In this section, design of an LCGT interferometer is discussed. A schematic diagram and the specifications of the interferometer are shown in Figure 1.3 and in Table 1.2, respectively.

Laser

A high-power laser is one of essential factors to improve sensitivity of gravitational wave detectors. LCGT requires a 150-W laser of good beam quality at a specific single frequency; details of the specifications for the LCGT laser will be discussed later in Section 1.4.3.

The purpose of this work is to construct a laser which meets all requirements of LCGT. Nd:YAG was chosen as the laser material, due to the preferable characteristics. Other possible light source for LCGT is examined in Appendix A.

Light source	
Laser medium	Nd:YAG
Wavelength	1064 nm
Output power	150 W
Frequency property	Single frequency

Input optics	
Overall power transmittance	50 %
1st mode cleaner (MC1)	
Cavity length	10 m
Cavity Finesse	1700
Free spectral range	15 MHz
Cutoff frequency	4.5 kHz
2nd mode cleaner (MC2)	
Cavity length	180 m
Cavity Finesse	1000
Free spectral range	833 kHz
Cutoff frequency	420 Hz

Main interferometer	
Arm cavity length (L)	3 km
Arm cavity Finesse (\mathcal{F})	1550
Power recycling gain (G_{PR})	11
Signal recycling gain (G_{SR})	15

Arm cavity mirrors	
Substrate material	Sapphire
Weight	30 kg
Temperature	20 K
Dimension	25 cm diameter, 15 cm thickness

Table 1.2: The specifications of LCGT^{16,21}.

Input mode cleaners and an output mode cleaner

At the input optics in Figure 1.3, two optical ring cavities, called mode cleaners (MCs), are used to make the input laser beam a perfect Gaussian mode. Each MC is located in vacuum and the mirrors are independently suspended by inverted pendulums to isolate seismic motion. In addition to the mode cleaning effect, the MCs function as stable frequency references for the stabilization of laser frequency.

Even after the two-stage mode cleaning, imperfection of the main interferometer causes distortion of the wavefront, or equivalently, it generates higher-order Gaussian modes. Since these modes increase the shot noise, another optical ring cavity, an output mode cleaner (OMC), is installed at the output port of the interferometer to reject the higher-order modes^{16,23}. The OMC is designed to be a wide-bandwidth cavity to pass the carrier, modulation sidebands and a gravitational wave signal.

Power recycling

Power recycling is a technique to increase the input power of the interferometer by reflecting the backward light toward the laser source back into the main interferometer²⁴. A power recycling cavity is formed by a power recycling mirror (PRM) located before the beamsplitter and the compound mirror of the Fabry-Perot cavity. In operation of an interferometer with power recycling, the power recycling cavity is kept in resonance with the carrier component of the optical field, which leads to increase of the effective power of the incident light.

Power recycling can be characterized by a parameter of the power recycling gain, G_{PR} . G_{PR} can be tuned by changing the reflection ratio of the power recycling mirror. In LCGT, the expected power recycling gain is 11, and thus the effective power in the interferometer can be increased by the factor of 11.

Resonant sideband extraction (RSE)

RSE is a technique to extract a gravitational wave signal by controlling an RSE mirror (SEM) located at the dark port of the interferometer^{16,25–28}. The RSE cavity is formed by the RSE mirror and the compound mirror of the Fabry-Perot cavity.

Since a gravitational wave signal will be canceled if it is stored in the Fabry-Perot cavity longer than the half cycle of the frequency of the gravitational wave, the finesse of the Fabry-Perot cavity cannot be high. The RSE technique mitigates the limitation of the finesse by extracting the gravitational wave signal before it is cancelled in the Fabry-Perot cavity. As a consequence, the signal bandwidth can be effectively increased by a factor of the signal recycling gain, G_{SR} .

The finesse of an arm cavity can be increased by using RSE when compared to an interferometer of the same sensitivity without RSE. Thus, more power can be stored in the arm cavity while reducing the optical power at the beamsplitter, which allows reduced power transmitting through the front mirrors and reduced thermal load due to absorption. Consequently, heat to be removed in order to keep the cryogenic temperature can be reduced in LCGT.

Results from several studies indicate that the sensitivity of an interferometer can be improved to even below the theoretical limit of the Standard Quantum Limit (SQL) at a narrow frequency bandwidth by detuning the RSE cavity^{26,28}. This technique is to be introduced in LIGO project's next-generation interferometer.

Suspension point interferometer

An active vibration isolation system, named suspension point interferometer (SPI), will be installed in LCGT. The SPI is an auxiliary interferometer formed by intermediate masses of the suspension system. By phase locking the SPI to a laser, the SPI cavity acts as if it were a rigid bar suspending the main interferometer. As a consequence, differential motion caused by seismic noise can be suppressed by the virtual rigid bar. Feasibility of the SPI technique was verified by Aso²⁹⁾ using a prototype system with results that showed the isolation ratio for the final mass of the two-stage suspension was improved by a factor of 100 (40 dB) below 1 Hz.

1.4.2 Sensitivity of LCGT

The goal of LCGT is to detect a gravitational wave from the coalescence of a binary system of neutron stars at 200 Mpc with an SNR of 10^{30} . The required sensitivity to detect the target gravitational radiation is $h_{\text{target}} = 3 \times 10^{-24} \text{ Hz}^{-1/2}$ at 100 Hz and the limitations due to noises should be well below this level.

The designed sensitivity of LCGT is shown in Figure 1.4. Formulas to calculate the sensitivity of LCGT is summarized in Appendix B. The observation frequency band is from several tens of hertz to 1 kHz, in which the sensitivity remains in the order of $h = 10^{-24} \text{ Hz}^{-1/2}$. Due to the cryogenic system introduced in the interferometer, the thermal noise will be reduced below other noises, limiting sensitivity of LCGT only by the quantum noise at the frequency region of our interest.

1.4.3 Specifications of the LCGT laser

In order to achieve the designed sensitivity of LCGT, the light source should fulfill the specifications^{||} as follows:

- Continuous wave with an output power of 150 W
- Single-frequency oscillation,
- No restriction on the absolute frequency, in principle (see Appendix A.1 for a discussion on the wavelength)
- Spatial beam quality of diffraction limit ($M^2 < 1.2$)
- Linearly polarized output
- Relative intensity stability ($\delta P/P$) of less than $10^{-8} \text{ Hz}^{-1/2}$
- Frequency stability ($\delta\nu$) of less than $10^{-8} \text{ Hz Hz}^{-1/2}$ relative to the frequency stability of the main interferometer

^{||}These specifications depend on the actual performance of the MCs and the main interferometer, and the requirements listed here are determined by empirical estimations based on experimental results of the TAMA project and the other interferometric detectors. Thus, there is a possibility that the requirements are relaxed if the interferometer performance is found to be superior to the current detectors, as well as a possibility that they might get even severer.

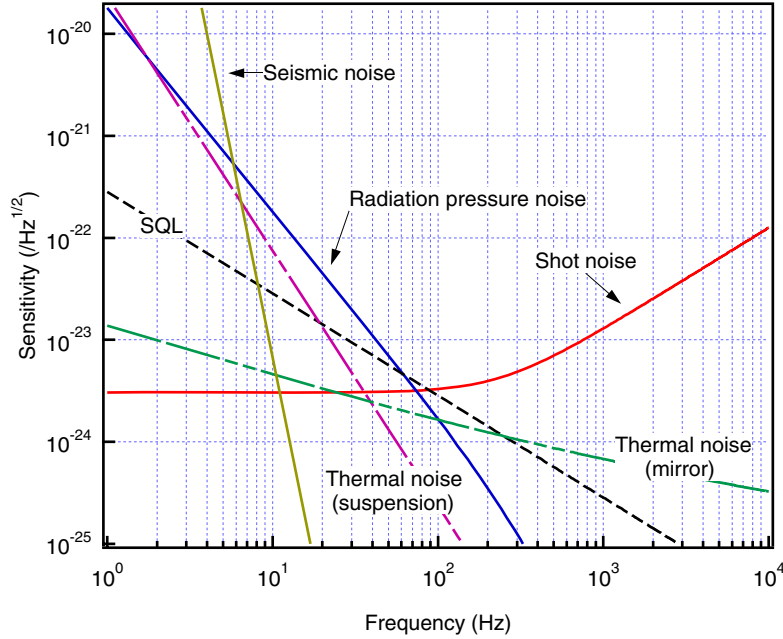


Figure 1.4: Expected sensitivity of LCGT. This plot is based on the calculation performed by Yamamoto³⁰⁾. The uppermost noise determines the sensitivity at each frequency band. In LCGT, the total sensitivity is limited by the seismic noise (below 7 Hz), the radiation pressure noise (from 7 Hz to 70 Hz) and the shot noise (above 70 Hz).

Output power

LCGT will be operated with quantum noise-limited sensitivity at observation frequency. Since the shot noise and the radiation pressure noise is dependent on the output power, the output power of the laser and the power recycling gain G_{PR} determine the overall sensitivity.

If the incident power into an interferometer increases, the recoil force against a cavity mirror exerted by the quanta will be reinforced, while the relative phase fluctuation between the coherent quanta will become faint due to the larger number of photons. An increased output power of the laser will therefore increase the radiation pressure noise while decreasing the shot noise.

For the LCGT configuration, the shot noise is dominant in the observation frequency; the shot noise calculated from Equation (B.13) is

$$h_{\text{shot}} = 2.4 \times 10^{-24} \left[\text{Hz}^{-1/2} \right] \left(\frac{75 \text{ W}}{P} \right)^{1/2} \sqrt{1 + \left(\frac{f}{240 \text{ Hz}} \right)^2} \quad (1.2)$$

where P is the laser power at the beamsplitter. According to Equation (1.2), the sensitivity of the LCGT can reach the goal sensitivity of $3 \times 10^{-24} \text{ Hz}^{-1/2}$ if the incident laser power into the main interferometer is 75 W.

In practice, the laser power undergoes attenuation in the input optics. Assuming that the overall transmittance of the optical power through the input optics is 50 %, the requirement of the output power can be determined to be 150 W.

Beam quality

Spatial beam quality of a laser affects the contrast of an interferometer fringe; and thus the output mode of the laser should be as close to a perfect Gaussian mode as possible. Since non-Gaussian components of light are rejected by input mode cleaners, the effective power will become smaller if the output spatial mode of the laser is distorted. The intensity suppression ratio of the higher-Gaussian modes by a mode cleaner is calculated according to the formula:

$$S_{m,n} = \left[1 + \left(\frac{2\mathcal{F}}{\pi} \sin((m+n)(\cos^{-1} g)) / 2 \right)^2 \right]^{-1}, \quad (1.3)$$

where \mathcal{F} is the finesse of the cavity, $g = 1 - L/R$ is the geometric factor and (n, m) is the order of an Hermite-Gaussian mode. The suppression ratio for the Hermite-Gaussian mode of 1st order in the MC1** is $S_{10} = 60$ dB (10^{-6}) and thus sufficient for our purpose.

If the higher order modes fluctuate, the competition between the modes over the available power will alter into intensity noise of the transmitted light through a mode cleaner. In order to compensate for the effect, intensity should be stabilized after passing through a mode cleaner^{31,32}.

The index factor M^2 is the conventional way to express spatial beam quality^{33,34}. The M^2 of an optical beam is defined by

$$M^2 = \frac{\theta_{ac} w_{ac}}{\theta_{df} w_{df}}, \quad (1.4)$$

where θ_{ac}, w_{ac} are divergence angle and waist size of an actual beam and θ_{df}, w_{df} are the counterparts of an equivalent ideal beam, or a diffraction-limited beam.

Let us consider propagation of a perfect Gaussian mode. The cross product of the beam divergence and the waist size is determined only by the wavelength of the light³⁵:

$$\theta w = \frac{4}{\pi} \lambda \sim \lambda, \quad (1.5)$$

and thus the M^2 value is always unity for an ideal Gaussian beam regardless of the divergence or the beam diameter. However, a real beam is often distorted and diffracted due to, for instance, truncation by an aperture or transmission through a non-uniform gain; thus the M^2 of an actual beam is in general larger than unity.

Although no theoretical model has been established which can predict how much power is transferred to higher order modes at a specific M^2 value, the conventional and somehow arbitrary criterion of the spatial quality is that a laser beam with an M^2 less than 1.2 has a good beam profile.

**Here, $R = 15$ m was assumed.

Intensity stability

In an ideal Michelson interferometer operated on a dark fringe, intensity noise of the laser source shouldn't appear at the output port because common-mode noise will be eliminated due to the destructive interference. However, in a real interferometer, there should exist asymmetry of storage time or finesse and thus the common-mode noise leaks to the output port as if it were differential noise. If the leakage of the common-mode noise is large enough to simulate a gravitational wave signal, there is no distinguishing between a real gravitational wave and the leaked common-mode noise.

Assuming an interferometer with a power-fluctuating laser source ($P(t) = P_0 + \delta P$), the electrical signal e at the output port is

$$e/\eta P_0 = -J_1(m) \left(\sin \Phi_0 \frac{\delta P}{P_0} + \delta\phi(\omega) \cos \Phi_0 \right) + \frac{\delta P}{P_0} \left((1 + J_0(m) \cos \Phi_0) \sin \omega_m t \right), \quad (1.6)$$

where η is a coefficient to transform the detected power at the output port into an electrical signal, Φ_0 is the phase of the operating point ($\sim \pi$), $\delta\phi(\omega)$ is the phase modulation caused by a gravitational wave, J_0, J_1 is the first-kind Bessel function of zeroth and first order, respectively, m is the modulation depth of the phase modulation of the light^{††} and ω_m is the modulation frequency. The frequency ω of a gravitational signal is in the order of several hundred hertz, and the typical modulation frequency is tens of megahertz. The modulation depth m is much smaller than unity, and hence the Bessel functions can be approximated to be $J_0(m) \sim 1$ and $J_1(m) \sim m/2$.

If we assume conditions of $\Phi_0 = \pi$, $\delta P = 0$, Equation (1.6) yields a signal just proportional to the phase correction $\delta\phi$ of the gravitational wave and thus the detection of the gravitational wave signal can be achieved.

However, if there is phase fluctuation $\Delta\Phi$ around the operating point Φ_0 , the first term of the right side of Equation (1.6) indicates that the intensity noise of the laser will be coupled with the fluctuation and cannot be distinguished with the gravitational wave signal:

$$\delta\phi_{\text{int}} = \frac{\delta P}{P_0} \Delta\Phi_0, \quad (1.7)$$

where $\delta\phi_{\text{int}}$ is the equivalent phase fluctuation caused by the intensity noise. Therefore, tight feedback control with a high gain is needed to suppress the phase fluctuation $\Delta\Phi_0$ to remove the spurious effect of the intensity fluctuation.

An expected residual rms fluctuation of the arm length ΔL_{rms} in the LCGT main interferometer is $\Delta L_{\text{rms}} = 1 \times 10^{-13}$ m, which is estimated according to an experimental result of TAMA. In that case, the sensitivity limited by the intensity noise h_{int} can be estimated by

$$h_{\text{int}} = \frac{\delta P}{P_0} \frac{\Delta L_{\text{rms}}}{L} \left[\text{Hz}^{-1/2} \right], \quad (1.8)$$

where L is the length of the arm cavity. Taking account of a safety factor of $F_{\text{safety}} = 1/10$, the requirement of the relative intensity noise $\delta P/P_0$ of LCGT can be determined by comparing the target gravitational wave of $h_{\text{target}} = 3 \times 10^{-24} \text{ Hz}^{-1/2}$ as follows:

$$\frac{\delta P}{P_0} < F_{\text{safety}} h_{\text{target}} \left(\frac{\Delta L_{\text{rms}}}{L} \right)^{-1} = 0.9 \times 10^{-8} \left[\text{Hz}^{-1/2} \right]. \quad (1.9)$$

^{††}Since an interferometric gravitational wave detector is operated on the dark fringe condition, the signal of a gravitational wave is of the second order and thus cannot be extracted without modulation.

Thus, the requirement for the LCGT laser is in the order of $10^{-8}\text{Hz}^{-1/2}$.

The second term on the right side of Equation (1.6) shows the contribution of fluctuation at the modulation frequency (ω_m) to the output signal $e(\omega)$. If the power fluctuation δP has a frequency component of $\delta\tilde{P} \sin((\omega + \omega_m)t + \phi)$, the power fluctuation at the modulation frequency will be down converted to the observation frequency band and appear as a spurious signal of

$$e \propto \delta\tilde{P} (1 + J_0(m)) \cos(\omega t + \phi), \quad (1.10)$$

which cannot be distinguished from a gravitational wave signal with the frequency ω . The intensity noise at modulation frequency should therefore be limited by the shot noise, which is the theoretical limit of the system.

Frequency stability

For the same reason as the intensity noise, the frequency fluctuation of the laser is coupled with the asymmetry of an interferometer and simulates a gravitational signal even though it is a common-mode noise. The frequency stability requirement for the LCGT laser can be estimated by the following relation:

$$\frac{\delta\nu}{\nu} = \frac{H_{\text{signal}}}{H_{\text{noise}}} h_{\text{target}}, \quad (1.11)$$

where H_{signal} is the transfer function of a gravitational signal to the output of the interferometer and H_{noise} is the transfer function of the frequency noise to the output of the interferometer. In the LCGT geometry (PRFPM+RSE), the transfer functions can be approximated by

$$\frac{H_{\text{signal}}}{H_{\text{noise}}} \sim \frac{1}{\epsilon} \frac{f_{\text{cavity}}}{f_{\text{PR}}} \frac{1 + i(f/f_{\text{PR}})}{1 + i(f/f_{\text{RSE}})}, \quad (1.12)$$

where ϵ is the common-mode rejection ratio of the interferometer, f_{cavity} is the cut-off frequency of the arm cavity, f_{PR} is the cut-off frequency of the power recycling cavity (~ 20 Hz) and $f_{\text{RSE}} = G_{\text{SR}} \times f_{\text{cavity}}$ is the bandwidth of the RSE with the recycling gain of G_{SR} . With an empirical prediction of the common-mode rejection ratio of $\epsilon = 100$, substituting the parameters of LCGT (see Table 1.2) and the target sensitivity $h_{\text{target}} = 3 \times 10^{-24} \text{ Hz}^{-1/2}$ into Equation (1.12) yields the frequency stability requirement at 100 Hz as follows:

$$\delta\nu \sim 3.4 \times 10^{-8} \left[\text{Hz Hz}^{-1/2} \right] \quad (1.13)$$

where a safety factor of 10 was taken into account. According to the result, the frequency stability should be in the order of $10^{-8} \text{ Hz Hz}^{-1/2}$.

In order to achieve the frequency stability required for LCGT, a multi-stage frequency stabilization technique is proposed^{16,36–38}. The laser is first phase locked to the MC1 and the error signal is fed back to frequency actuators of the laser system; the laser frequency is stabilized with the MC1 as a frequency reference. Then, the transmitted light through the MC1 will be, again, phase locked to the MC2, which has better frequency stability. The error signal with respect to the MC2 is fed back to a frequency actuator of the MC1 at low frequency region (up to 1kHz), and is injected into the MC1 feedback loop at the error signal point in the higher frequency region. A similar procedure is taken for the main interferometer; the error signal in the lower frequency region is fed back to a frequency

actuator of the MC2 while also fed back to the error signal point of the MC2 feedback loop in the higher frequency.

Since the laser is phase locked to the main interferometer and the differential motion of the interferometer arms is the signal which we need to detect, the absolute frequency of the laser is not a significant factor. Also, the final goal of the frequency stability should be measured relative to the frequency stability of the main interferometer.

1.4.4 Key techniques for the LCGT laser

It is not easy to answer the question how to construct a laser which fulfills all the requirements aforementioned. Since thermal problems in laser medium will become more serious as pumping power increases, it would not be a solution just to pump a laser medium harder or add other active laser materials in the cavity; these efforts for high-power, single-frequency oscillation would end in vain.

In developing a laser system for LCGT in this work, two techniques are the key to scaling the output power at a single frequency: One is master-oscillator power-amplifier (MOPA) and the other is injection locking³⁹.

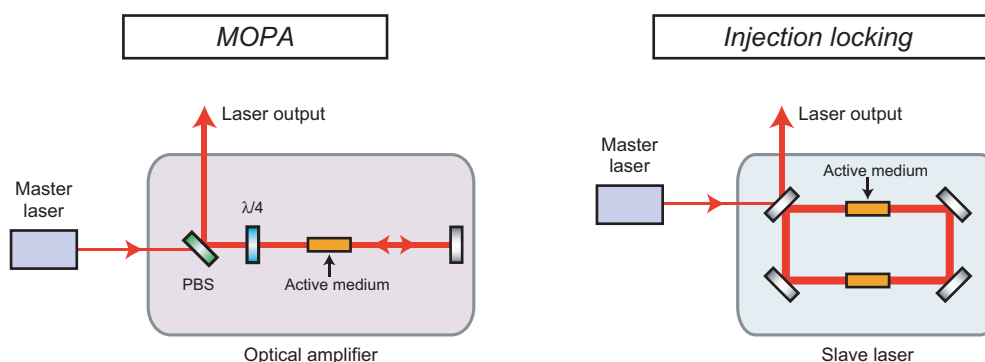


Figure 1.5: Schematic illustration of MOPA in a double-pass configuration (left) and injection locking with two active laser media (right). PBS: Polarizing beamsplitter, $\lambda/4$: Quarter wave plate.

MOPA

MOPA uses optical amplifiers to increase master laser power and is a rather simple way to scale up the output power of a laser at a single frequency. However, the simple geometry, in turn, raise problems of wavefront distortion and amplified spontaneous emission (ASE) during the amplification process.

Wavefront distortion is caused by either non-uniform distribution of gain or a mode mismatch between amplifier and master laser. Since degradation of beam quality results in reduction of the effective laser power, compensation of these effects is essential. There are two possible methods to restore distorted wavefront; one is adaptive optics with a deformable mirror; the other is to use a phase conjugate mirror. These devices might be used for the LCGT laser if wavefront distortion is the primary factor to improve the laser performance.

Even when uniformity of the pumping profile might be perfect, there is an unavoidable effect of thermally induced birefringence, which causes depolarization in a transmitted light. Compensation of the depolarization is also indispensable.

Excess gain in an active medium, which is not consumed in amplification, contributes to ASE. Degradation of beam quality due to ASE becomes more evident for the case of power amplification with high gain, in which spontaneously emitted light can easily be amplified to the power level comparable to the master laser. Or even less desirable, the ASE can cause self-sustained oscillation, called parasitic oscillation, which limits the usefulness of MOPA in an unsaturated configuration.

ASE can be reduced by operating an amplifier with a strong optical field focused in the medium, called saturated amplification. The saturation of an amplifier gain can be expressed by⁴⁰⁾

$$g(I) = \frac{g_0}{1 + I/I_{\text{sat}}}, \quad (1.14)$$

where g_0 is the unsaturated gain, I is the light power per unit area in the laser medium and I_{sat} is the saturation power density. In amplification with a highly saturated gain, the master light no longer grows exponentially as the unsaturated amplification does, but the active medium adds the power to the master field efficiently. In this sense, saturated amplification can be considered to be a power addition process rather than power multiplication.

Injection locking

Injection locking is a technique to operate a high-power slave laser at a single frequency by injecting a stable, single-frequency master laser. In contrast to the MOPA technique, the spatial mode of the injection-locked output is selected by the slave laser cavity. Thus, an output of a good beam profile of diffraction limit can be achieved through this technique.

The frequency bandwidth over which a slave laser is kept injection-locked is called the locking range, which can predict the maximum drift of frequency difference between master and slave laser. The full width of the locking range can be estimated by the formula:

$$\Delta\nu_{\text{lock}} = 2 \delta\nu_{\text{slave}} \sqrt{\frac{P_{\text{master}}}{P_{\text{slave}}}}, \quad (1.15)$$

where $\delta\nu_{\text{slave}}$ is the linewidth of the slave cavity, P_{master} , P_{slave} are the output power of the master laser and the slave laser, respectively. According to Equation (1.15), the locking range depends on the power ratio between the master and the slave laser; therefore, it is difficult to control a high-power slave laser with a master laser of small output power. The lower limit of the power ratio $P_{\text{master}}/P_{\text{slave}}$ is not obvious; and the current reported ratios range from from $1/14$ ⁴¹⁾ to $1/222$ ⁴²⁾.

Further discussion of injection locking is given in Section 3.1.

1.4.5 Design of the LCGT laser

I designed a Nd:YAG laser system for LCGT, which uses two-stage power amplification, as shown in Figure 1.6. In the first amplification stage, injection locking is used to generate a single-frequency output with an output power of 100 W; then, the injection-locked laser is amplified to the required output power of 150 W in the second amplification stage.

The frequency of the laser system is stabilized by locking to a reference frequency^{37,38,43)} using the Pound-Drever-Hall technique⁴⁴⁾; the control loop for the frequency stabilization is shown in the upper

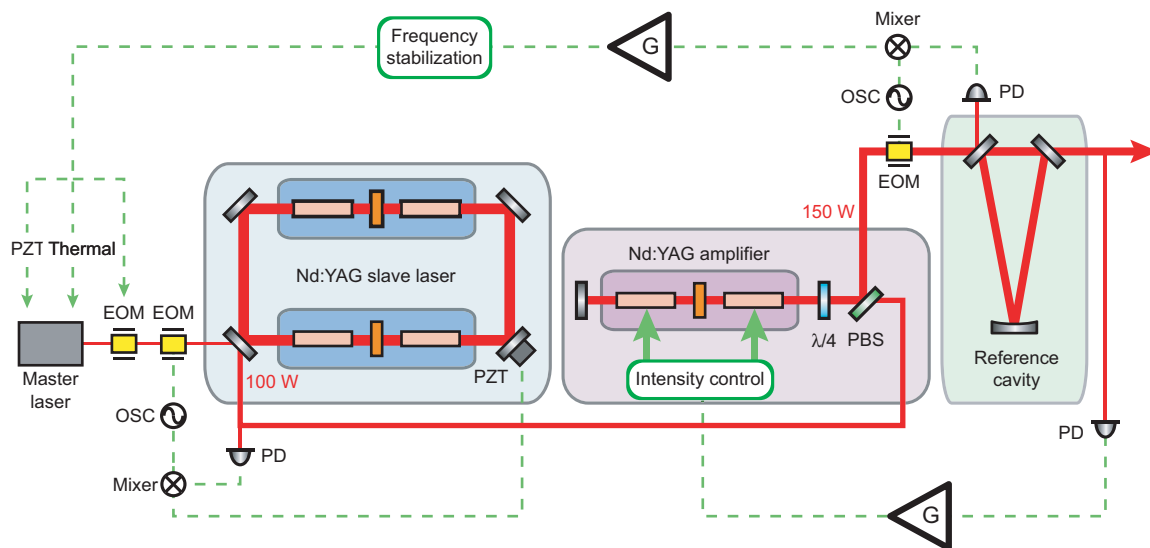


Figure 1.6: Design of the LCGT laser. EOM: Electro-optic modulator, OSC: Electrical oscillator, PZT: Piezo-electrical transducer. The triangle denotes a feedback servo filter with a transfer function of G .

broken line in the diagram. The feedback signal is applied to the master laser of the injection locking and the MOPA, which controls the overall frequency characteristics of the system. The frequency of the master laser is actuated by a piezo-electric transducer (PZT) and a temperature controller, which are built-in functions of the master laser. An external electro-optic modulator (EOM) is used to extend the bandwidth of the feedback servo to a few megahertz^{45,46}.

The intensity fluctuation of the laser output is suppressed by controlling the amplification ratio of the MOPA system. A fraction of the transmitted light through a mode cleaner is picked off and the AC signal of the intensity fluctuation is amplified and negatively fed back to the amplifiers.

Together with direct current modulation, shunting of the injected current into the pumping diode of the laser head is used to control the amplification ratio⁴⁷. With this technique, intensity noise suppression of a 10-W laser to $10^{-8} \text{ Hz}^{-1/2}$ was reported⁴⁸. Since the power fluctuation to be stabilized in this work is higher than the previous experiment, the feasibility of the current shunting technique of this power level has not been proven yet.

Another possible method to control the intensity is to use an external acousto-optic modulator (AOM) or an electro-optic modulator (EOM), which have a wide control bandwidth. However, since the laser power to be used in a future detector is on the order of 100 W, there is no crystal for these devices that has such a high thermal fracture limit.

For the design shown in Figure 1.6, I took advantages of both injection locking and MOPA: injection locking is suitable to generate an output power of 100 W of excellent beam quality, while MOPA can amplify the output to the required power just by adding amplifiers to the system; the simplicity and

Project	Laser	Power	Configuration
TAMA	Nd:YAG ($\lambda = 1064$ nm)	10 W	Injection-locked, end-pumped rod
LIGO	Nd:YAG ($\lambda = 1064$ nm)	10 W	Double-pass MOPA
VIRGO	Nd:YVO ₄ ($\lambda = 1064$ nm)	20 W	Injection-locked, end-pumped rod
GEO 600	Nd:YAG ($\lambda = 1064$ nm)	14 W	Injection-locked, end-pumped rod

Table 1.3: Lasers in the current detectors.

ately to the laser constructed in this work. Performance of the TAMA, LIGO, VIRGO, GEO 600 lasers is examined in Section 1.6.1.

The requirements for the free-running laser in this work are as follows:

- Continuous wave with an output power of 100 W
- Single-frequency oscillation
- Spatial beam quality of diffraction limit ($M^2 < 1.2$)
- Linearly polarized output
- Intensity stability comparable to those of the current lasers: at the level of 10^{-5} Hz^{-1/2} without intensity stabilization
- Frequency stability limited by the master laser for an unstabilized injection-locked laser

The overall optical layout of the experiments in this thesis is shown in Figure 1.7. If these specifications are fulfilled, further improvements of the performance can be made by applying the same technique as those used in the current detectors.

There is another purpose for this work: it is to evaluate the frequency controllability of a high-power, injection-locked laser. Since no experiment on stabilization of such a high-power laser has been reported, it is crucial to confirm to what extent frequency of a high-power laser can be controlled by the same technique used for the current lasers.

1.6 Other high-power, single-frequency lasers

For reference, I will review high-power, cw, single-frequency, 1- μ m lasers reported in this section.

1.6.1 Lasers in the current detectors

The lasers in the current gravitational wave detectors are summarized in Table 1.3.

The TAMA laser is a 10-W, injection-locked Nd:YAG laser at wavelength of 1064 nm, constructed by SONY corporation⁴⁹). The frequency of the laser is stabilized by a multi-stage stabilization technique in which an optical cavity and the main interferometer are used as stable frequency references^{37,38,50}). As a result, frequency stability of 10^{-6} Hz Hz^{-1/2} at 100 Hz relative to that of the main interferometer has been achieved, satisfying the requirement for the TAMA interferometer.

The intensity stability of the 10-W laser in the TAMA interferometer is on the order of $10^{-5} \text{ Hz}^{-1/2}$ at 100 Hz without stabilization, and $3 \times 10^{-8} \text{ Hz}^{-1/2}$ was achieved when the laser was stabilized with an external intensity modulator³⁷⁾.

Recently, another 10-W, injection-locked Nd:YAG slab laser has been installed in TAMA, which was developed by a research group at the University of Adelaide⁵¹⁻⁵⁴⁾. The slave laser consists of a coplanar folded zigzag slab and diode laser arrays for side pumping and is injection locked to a 700-mW master laser. Temperature of the slave laser is controlled by a conduction cooling system with an air flow cooled heat sink. The intensity stability of the laser is on the level of $10^{-5} \text{ Hz}^{-1/2}$ without stabilization, limiting the frequency stability by the master laser.

The LIGO laser is using a MOPA scheme, which consists of a 700-mW master laser and double-pass amplifiers with four end-pumped Nd:YAG rods^{32,47,48,55)}. The intensity noise in free running is at the level of $10^{-5} \text{ Hz}^{-1/2}$ at 100 Hz and suppressed to $10^{-8} \text{ Hz}^{-1/2}$ at an out-of-loop photodetector using a premode cleaner and current actuators.

Advanced LIGO will use an end-pumped 180-W Nd:YAG rod laser, which has been proposed by a research group at Laser Zentrum Hannover⁴¹⁾.

An end-pumped Nd:YAG laser system is being used in GEO 600^{56,57)}. The laser generates an output power of 14 W with an M^2 value of 1.1. The polarization is better than 1:49, and optical-optical efficiency reaches 40 %.

The eigenfrequency fluctuations of the slave laser cavity is on the order of $10^4 \text{ Hz Hz}^{-1/2}$ at 100 Hz, falling at higher frequency. The intensity fluctuation of $10^{-6} \text{ Hz}^{-1/2}$ in free running was stabilized to approximately $10^{-7} \text{ Hz}^{-1/2}$, measured at an out-of-loop detector.

Initially, an injection-locked, 10-W Nd:YAG laser was used in the VIRGO project⁵⁸⁾ which exhibited the intensity stability of $10^{-5} \text{ Hz}^{-1/2}$ at 100 Hz. An injection-locked Nd:YVO₄ laser, which can deliver an output power of 20 W at 1064 nm, has been replaced for the 10-W laser since 2002¹²⁾.

1.6.2 Historical aspect of the development of single-frequency lasers

In recent years, there has been progress in development of high-power, single-frequency lasers; Figure 1.8 shows a historical chart of the development for single-frequency lasers with an output power over 10 W.

Although not shown in the chart, one of the most efficient and stable Nd:YAG lasers at a single frequency is the non-planar ring oscillator (NPRO)⁵⁹⁾, which is now commercially available and widely used in many laboratories. This laser makes use of Faraday rotation to enforce unidirectional oscillation and exhibits excellent stability due to the monolithic structure. Currently, the end-pumping configuration limits the maximum available power to 2 W⁶⁰⁾, which is strong enough for the use in most experiments.

As shown in the chart, several groups have been developing single-frequency lasers with injection locking^{41,61-67)} or MOPA⁶⁸⁻⁷¹⁾. It is noticeable that the output power of a single-frequency laser has rapidly increased within the past few years, exceeding an output power of 100 W. At the end of 1980s, flash lamp pumped lasers were taken over by diode laser pumped lasers⁷²⁾, increasing the output power of pumping lasers to several hundred watts; therefore, reduced thermal load and low intrinsic noise of the diode laser output enabled efficient and stable oscillation at a single frequency.

1.7 Other frequency stabilization experiments

At the early stage of optical cavity frequency stabilization experiments, gas or dye lasers were used as the laser sources⁷³⁻⁷⁵.

The first demonstration of frequency stabilization with a diode-pumped Nd:YAG laser to an optical cavity was reported by Shoemaker⁴³). Several groups have investigated the frequency spectrum of stabilized diode-pumped Nd:YAG lasers^{37,38,45,46,76-81}). The frequency stability in these experiments is summarized in Figure 1.9. The frequency stability shown in the graph is the best value in each experiment, and thus the frequency region for the best stability is different between experiments.

Nagano³⁸) reported an experiment to stabilize the 10-W laser of TAMA to the main interferometer, which achieved the lowest frequency fluctuation at an output power of 10 W. In the experiment, a two-stage frequency stabilization technique was applied to the laser resulting in a frequency stability of $10^{-6} \text{ Hz Hz}^{-1/2}$.

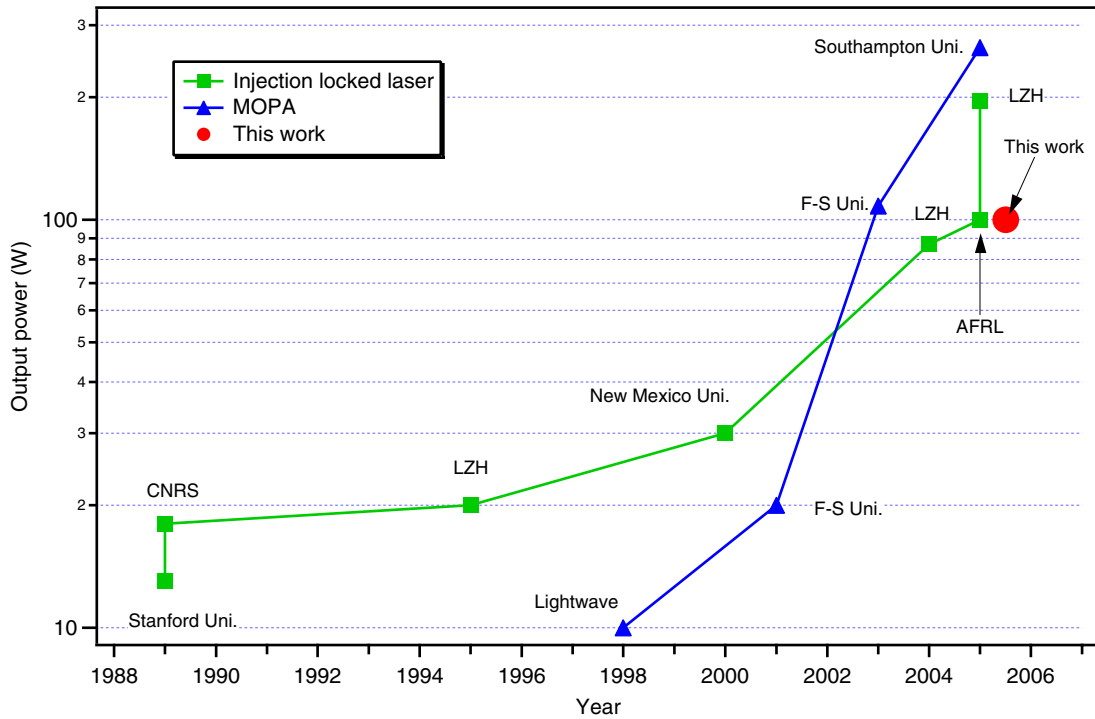


Figure 1.8: Chart of the history of development of single-frequency lasers. The line with filled squares shows the output power of injection-locked lasers, and the line with triangles shows the output power of MOPA systems. The abbreviated terms are respectively; CNRS: Centre national de la recherche scientifique (France), LZH: Laser Zentrum Hannover (Germany), Lightwave: Lightwave Electronics Corporation (U.S.A.), F-S Uni.: Friedrich-Schiller University (Germany), AFRL: Air Force Research Laboratory (U.S.A.).

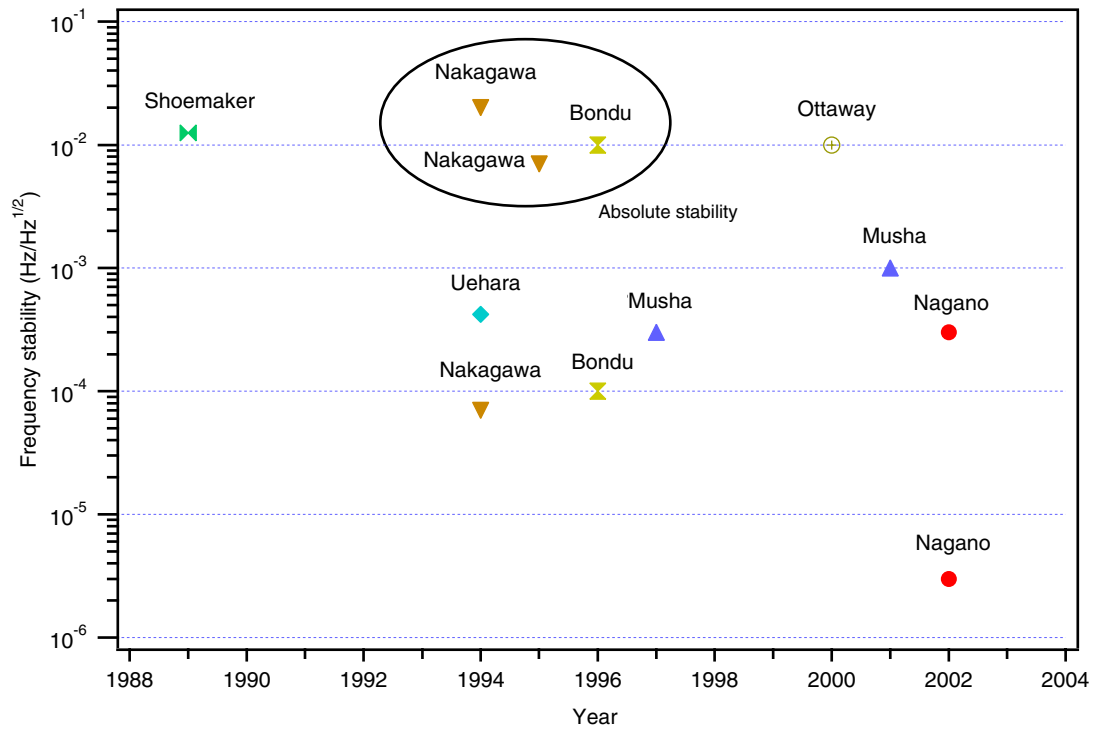


Figure 1.9: Frequency stability ever reported, which was measured as linear spectral density. Note that the frequency stability was measured in absolute unit for the results of Nakagawa^{46,77} (upper markers) and Bondu⁷⁸ (upper marker). The other results were evaluated with respect to reference stability.

Chapter 2

Development of a slave laser

The final goal of this work is to develop a 100-W, single-frequency laser of excellent beam quality. Nd:YAG was chosen as the laser medium due to the intrinsic low noise of the laser output and preferable characteristics of the host material. The achieved results so far are: (1) construction of the first amplification stage of the LCGT laser with injection locking and (2) success in generating an output power of 100 W at a single frequency with properties of a good spatial mode and linear polarization. The following two chapters describe the construction process of the 100-W, injection-locked Nd:YAG laser.

2.1 Theoretical background

Theoretical models of laser oscillation are given in texts^{34,35,39}. I will review the models in this section.

2.1.1 Laser oscillation

Laser oscillation occurs through three processes: spontaneous emission, amplification by stimulated emission and feedback by a laser cavity.

Spontaneous emission, stimulated emission and stimulated absorption can be expressed in a quantum-mechanical model of energy transfer between two energy levels. In stimulated emission, other quanta are added to the spontaneously emitted quanta coherently, or in an indistinguishable way from the original quanta. Then, the identical quanta are reflected back by cavity mirrors and again undergoes amplification by stimulated emission. This process occurs in the laser cavity repeatedly; as a consequence, the light is infinitely amplified and laser oscillation results.

Once laser oscillation is achieved, the round-trip gain is clamped at the point where the gain and the total internal loss are in balance, that is

$$\frac{g_0}{1 + I_{\text{circ}}/I_{\text{sat}}} = \delta_{\text{total}}. \quad (2.1)$$

Here, g_0 is the small signal gain, I_{circ} is the power density of the circulating light at the laser medium, I_{sat} is the saturation intensity and δ_{total} is the total internal loss.

Linear cavity configuration

A linear cavity laser consists of two mirrors facing to each other and a laser medium placed between the mirrors. The output power from a linear cavity laser is expressed in the form

$$\begin{aligned} P_{\text{out}} &= \left(\frac{1-R}{1+R} \right) AI_{\text{sat}} \left(\frac{2\eta_u \eta_B P_{\text{ab}}}{(\delta - \ln R) AI_{\text{sat}}} - 1 \right), \\ &= \sigma_S (P_{\text{in}} - P_{\text{th}}), \end{aligned} \quad (2.2)$$

where R is the reflectivity of the output coupler, δ is the internal loss excluding output coupling, A is the cross section area of the laser medium, η_u is the quantum efficiency of the laser medium, η_B is the beam overlap efficiency between the pumping profile and the resonator mode. In Equation (2.2), σ_S is the slope efficiency and P_{th} is the threshold of the laser oscillation: σ_S is expressed by

$$\begin{aligned} \sigma_S &= \frac{2(1-R)}{(1+R)(\delta - \ln R)} \eta_P \eta_T \eta_a \eta_u \eta_B, \\ &\approx \frac{T}{T + \delta} \eta_P \eta_T \eta_a \eta_u \eta_B, \end{aligned} \quad (2.3)$$

where T is the transmittance of the output coupler ($T + R \sim 1$), η_P is the pump source efficiency, η_T is the radiation transfer efficiency, η_a is the efficiency of the absorption of useful pump radiation. P_{th} is expressed in the form

$$P_{\text{th}} = (\delta - \ln R) \frac{AI_S}{2\eta_P \eta_T \eta_a \eta_u \eta_B}, \quad (2.4)$$

$$\approx (\delta + T) \frac{AI_S}{2\eta_P \eta_T \eta_a \eta_u \eta_B}. \quad (2.5)$$

According to these relations, the slope efficiency and the threshold of laser oscillation are dependent on the internal loss and the reflectivity of the output coupler. The optimum coupling coefficient is estimated by the formula

$$T_{\text{opt}} = \left(\sqrt{2g_0 L / \delta} - 1 \right) \delta, \quad (2.6)$$

where L is the length of the laser medium.

Previous experimental results have demonstrated that Equation (2.6) is valid to predict behavior of laser oscillation⁸². However, Equation (2.6) is helpful only when the internal loss remains relatively at a constant value; for instance, the equation is applicable to the case when radius of curvature of cavity mirrors is large compared to cavity length.

As will be seen in Section 2.5.2, the internal loss of the laser cavity in this work changed drastically according to the pumping power and thermal lensing. Thus, the behavior of the output power of the laser couldn't be predicted simply by Equation (2.2), but was rather complicated in increasing the output power.

Ring cavity configuration

In order to injection lock a slave laser to a master laser, the injection port of the master laser and the output port of injection locking should be separated; the slave laser should be constructed in a

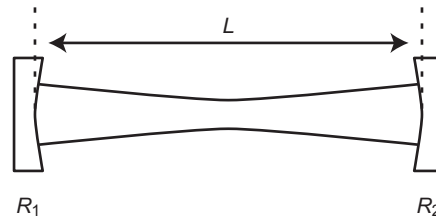


Figure 2.1: Linear cavity with length L and mirrors with radius of curvature R_i .

ring cavity configuration. In a free running state, a ring laser oscillates both in the counter-rotating directions and the output power is extracted from the two output ports.

Circulating light in a ring cavity passes through the laser medium only once; thus, the model of a linear cavity cannot simply be applied to a ring cavity. However, the ring cavity built in this work used two laser modules of the same specification and the model of the linear cavity could be applied to the design of the ring cavity.

A ring cavity laser has the advantage of hole-burning free oscillation, in principle, due to the traveling wave configuration which eliminates spurious effects of gain competition and parasitic oscillation.

2.1.2 Stability condition of laser oscillation

The stability condition of a Fabry-Perot cavity (without a gain medium) can be expressed by the geometric factor g as:

$$0 < g_1 g_2 < 1, \quad (2.7)$$

where $g_i = 1 - L/R_i$, L is the cavity length and R_i is the radius of curvature of the cavity mirror^{35,83}. If the condition is met, the internal field travels back and forth with little fraction of the field escaping out of the cavity.

The actual configuration of the linear cavity laser built in this work is complicated, as the cavity contains two thermal lens media in a cavity and the stability condition cannot be expressed in such a simple way as that of a Fabry-Perot. Thus, I used the results of the analysis performed by Konno⁸⁴) in which the stability condition was numerically analyzed by modeling the laser cavity with ABCD matrices.

2.1.3 Thermal distortion and compensation

When building a high-power laser, thermal lensing and thermal birefringence limit the maximum output power available from a laser medium. Both of the effects become more and more serious as pumping power increases further; thus, they should be compensated for with adequate methods so as to extract as much power as possible from a laser medium.

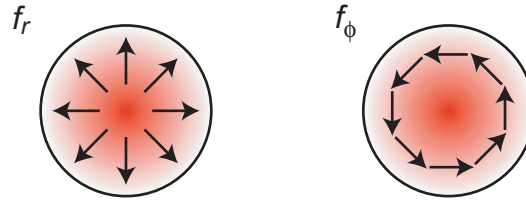


Figure 2.2: Independent polarization states in the cross section of a uniformly pumped rod.

Thermally induced bifocusing

Let us consider a uniformly pumped Nd:YAG rod which is cooled by coolant flow on the surface: this is the case with the laser head used in this work. The Nd:YAG rod is cut in the (111)-direction, and I estimate thermal effects accordingly.

Due to quantum defect and other heating processes, thermal load in a rod-shaped laser medium causes parabolic gradient of the refractive index across the cross section. In addition to the temperature dependence of the refractive index, the thermo-optic coefficient of the Nd:YAG rod is different in the radial and tangential directions in the rod cross section.

When fractions of pumping power are dissipated as heat in a uniformly pumped Nd:YAG rod (with length L and diameter of the cross section $2r_0$), the distribution of the refractive index in the Nd:YAG rod is

$$n(r) = n_0 \left[1 - \frac{P_a}{2\pi r_0^2 L \kappa} \left(\frac{1}{2n_0} \frac{dn}{dT} + n_0^2 \alpha C_{r,\phi} \right) r^2 \right], \quad (2.8)$$

where n_0 is the refractive index of Nd:YAG, κ is the thermal conductivity, dn/dT is the temperature dependence of the refractive index, α is the thermal expansion coefficient and C_r , C_ϕ are the functions of the elasto-optical coefficients of Nd:YAG.

The equivalent focal length, $f_{r,\phi}$, of a lens-like medium with a parabolic distribution of the refractive index as shown in Equation (2.8) is

$$f_{r,\phi} = \frac{\kappa A}{P_a} \left(\frac{1}{2} \frac{dn}{dT} + n_0^3 \alpha C_{r,\phi} \right)^{-1}. \quad (2.9)$$

According to Equation (2.9), the focal length of the thermal lens is inversely proportional to the dissipated power in the rod, or to the absorbed power if we can assume a constant mode matching for all pumping power. The focal length of the thermal lens becomes shorter as the laser medium is pumped harder; it is difficult to achieve laser oscillation for thermal lensing with a too short focal length compared to the cavity length.

Equation (2.9) also shows that the thermal lensing is different in the radial direction and the tangential direction, and thus the laser cavity possesses two independent cavity polarization states with the different focusing profiles called thermally-induced bi-focusing. Table 2.1 compares the relative strength of each term in the bracket of Equation (2.9); the diopter of the focal length can be different by 20 % between the radial and tangential direction in the rod cross section. Without compensation for

Term in Equation (2.9)	$\frac{1}{2} \frac{dn}{dT}$	$n_0^3 \alpha C_r$	$n_0^3 \alpha C_\phi$
Amplitude	3.6×10^{-6}	7.4×10^{-7}	-1.1×10^{-7}
Ratio	1	0.2	-0.03

Table 2.1: Comparison between the terms of the thermal lensing. The ratio shows the relative strength of the thermal lensing effect to the temperature dependence of the refractive index.

the thermal bi-focusing, the cavity polarization modes compete against each other and thus intensity of the laser output becomes unstable.

Compensation for the thermal effect

A technique to compensate for the thermal bi-focusing is to use a polarization rotator to exchange the radial and the tangential components of the polarization and then pass the light through the same bi-focusing medium^{85–87}). As a result, the light undergoing the double-pass compensation is phase-shifted by the same amount for any polarization state and the polarization of the transmitted light suffers from no depolarization.

In order to compensate correctly for the depolarization with this technique, the spatial distribution of the electric field in the first gain should be reproduced in the second gain in exactly the same way. Imaging optics to transfer the principle plane of a gain medium to the second medium was suggested to overcome the problem of reproducing the electric field⁸⁸). The feasibility of the technique was proved experimentally with a high power laser system⁴¹).

In this work, laser media were located close to each other and thus no imaging optics was required to achieve the thermal effect compensation. It is preferable to dispense with another intracavity components from viewpoint of reducing possible internal loss.

2.2 How to construct a slave laser

To achieve single-frequency oscillation by injection locking, I should construct a ring laser with an output power of 100 W and beam quality of diffraction limit.

In an ideal case, injection locking controls not only frequency, but also spatial profile and polarization⁸⁹) due to the indistinguishability of quanta in stimulated emission. However, in practical situations, mode-mismatched gain can cause laser oscillation even in the presence of a strong master field circulating in the slave laser cavity. The spatial profile of the slave laser thus should be diffraction-limited; otherwise, the slave laser cannot be mode matched to a master laser no matter how well one may design the imaging optics. Mismatching between the laser modes leads to degradation of the spatial mode and polarization of an injection-locked output due to the uncontrolled components of the slave laser. It can even trigger laser oscillation in the backward direction.

Due to thermal problems, the output power of a low-power laser cannot be scaled easily to over 100 W while retaining good beam quality; thus I followed three processes to construct a slave laser. The flow chart is shown in Figure 2.3 and the processes are as follows:

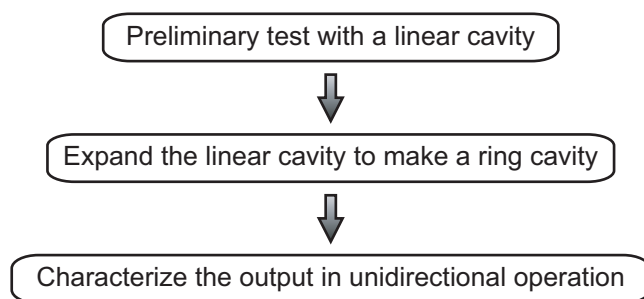


Figure 2.3: Flow chart of the construction process of a high-power ring laser.

1. Built a laser in a linear cavity configuration, and optimize the parameters of the cavity length and the reflectivity of the output coupler.
2. Expanded the linear cavity to a ring cavity so that the laser could be used as the slave laser in injection locking; the design of the ring cavity was based on the optimized parameters of the linear cavity.
3. Characterized the output mode of the ring cavity; since the intensity of the free-running laser was not stable enough to measure the beam quality, the ring laser was enforced unidirectional oscillation with an intracavity Faraday rotator.

The first process has already been investigated intensively by a Mitsubishi Electric Corporation research group^{84, 90–93}, of which I made use of the results. The second and third processes are ideas developed in this work.

2.3 Side-pumped Nd:YAG laser module

In order to construct a slave laser, a commercially available Nd:YAG laser module ($\lambda = 1064$ nm) developed by the Mitsubishi high-power laser group was used. The side view and the cross section of the laser module is shown in Figure 2.4 and Figure 2.5, respectively. The module was originally developed for the purpose of industrial processing, and thus no attention was devoted for the frequency property of the laser output.

One laser module consists of two identical Nd:YAG rods (4 mm in diameter and 7 cm in length) and a quartz rotator. The quartz rotator is placed between the Nd:YAG rods in order to compensate for the thermally induced birefringence in each rod by rotating the polarization and cancel out the depolarization.

The Nd:YAG rod is placed in a ceramic chamber and side-pumped by diode laser arrays. The pumping light is diffused in the ceramic chamber and absorbed by the Nd:YAG rod. This scheme was proved to be highly effective and feasible to pump the rod medium uniformly⁹⁰.

The laser module is cooled by a primary-secondary water cooling system. The temperature of the secondary circulating water, which removes the heat from the Nd:YAG rods and diode lasers, is kept at

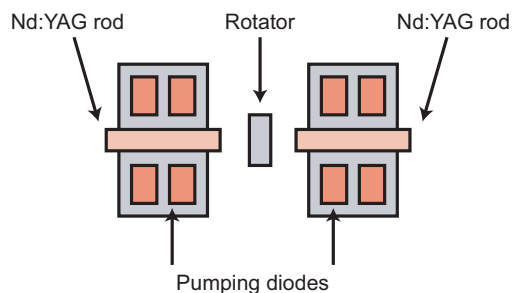


Figure 2.4: Side view of the laser module. The laser module consists of two Nd:YAG rods and a quartz rotator.

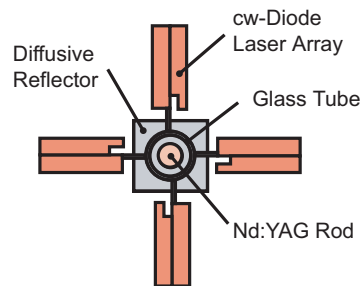


Figure 2.5: Cross section of the laser pumping module and the Nd:YAG rod. The Nd:YAG rod is placed in a ceramic chamber.

25°C. Since conduction cooling by a thermo-electric cooler cannot remove the thermal load of several hundreds of watts, water cooling is the only way to stabilize the temperature for the laser module. The vibration caused by water turbulence is thus inevitable for this laser system.

2.4 Preliminary experiment in a linear cavity configuration

A linear cavity laser was constructed and tested with the laser module. The cavity geometry was based on the design by Konno⁸⁴.

2.4.1 Design of the linear cavity

In the design of a linear cavity laser proposed by the Mitsubishi group, the stable region of the linear cavity can be shifted to higher pumping region by using convex mirrors with radius of curvature of 20 cm; each mirror is located at 45 cm from the end of the rod. The schematic diagram of the linear cavity laser is shown in Figure 2.6.

Figure 2.7 shows the result of a mode simulation of the linear cavity. Thermal lensing with a focal length of 50 cm in each rod was assumed; the focal length was an average value of f_r and f_ϕ at the operating pumping power.

In order to improve the beam quality, a Brewster plate and an aperture were placed in the laser cavity. The Brewster plate discriminates the p- and s-polarized light due to the different reflection coefficient between the two polarization states. As a consequence, the p-polarized light, which can travel along the round trip with less internal loss, can predominantly oscillate.

The aperture truncates the high-order Gaussian modes, whose spatial profiles are extending further compared to that of the fundamental Gaussian mode, and only the component of the diffraction-limited mode can survive in the laser cavity. The aperture size was chosen to be approximately 1.6 times larger

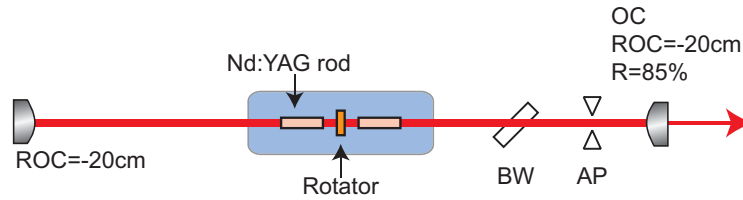


Figure 2.6: Schematic diagram of the linear cavity. OC: Output coupler, ROC: Radius of curvature, BW: Brewster window, AP: Aperture. The negative value of the ROC indicates a convex mirror.

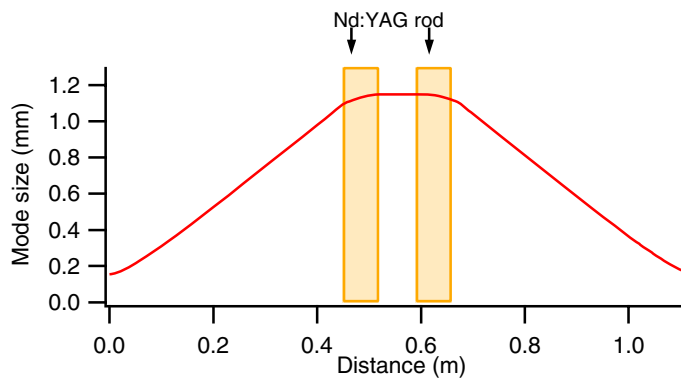


Figure 2.7: Simulation of the cavity mode in the linear cavity configuration. The filled square shows the position of the Nd:YAG rod.

Output power	60 W
Spatial mode	Single transverse mode
M^2 in the horizontal plane	1.12
M^2 in the vertical plane	1.13
Polarization of the output	Linearly polarized
Polarization state	Vertically (s-) polarized
Polarization ratio	1:40

Table 2.2: Characteristics of the output of the linear cavity laser with the Mitsubishi laser module.

than the size of the diffraction-limited mode by adjusting the position of the aperture along the optical axis.

2.4.2 Results of the linear cavity operation

The linear cavity laser generated an output power of 60 W with a linearly polarized, diffraction-limited mode. The output power and the beam quality of the linear cavity laser is summarized in Table 2.2. The M^2 was measured with Coherent's ModeMaster PC.*

According to the result, high output power of good beam quality (a single transverse and linearly polarized mode) was achieved in a linear cavity configuration.

2.5 Design of a slave cavity

I designed a ring cavity laser based on the result of the linear cavity experiment.

2.5.1 Ring cavity configuration

If a linear cavity laser is expanded to a ring cavity just by detouring the return path of the circulating light, a single pass through the laser medium in a round trip results in a different circulating power and different thermal lensing. The cavity mode in the ring cavity, therefore, will become totally different from the mode in the linear cavity.

The problem of how to expand the linear cavity was circumvented by using another laser module of the same property; the schematic diagram of the ring cavity is shown in Figure 2.8.

In the ring cavity with two laser modules, the circulating light undergoes amplification twice in each round trip and the total internal power becomes exactly the same as that of a linear cavity for either case in free running or injection locking. The extracted power from each module and the thermal lensing also coincides with those of the linear cavity. Therefore, the design of the optimized linear cavity can be applied to the ring cavity without any changes.

The schematic drawing of the actual ring cavity is shown in Figure 2.9. The parameters of the ring cavity are the same as those of the linear cavity; the reflectivity of the output coupler is 85 %, two

*The M^2 is approximately 1.3 without an internal aperture in specification.

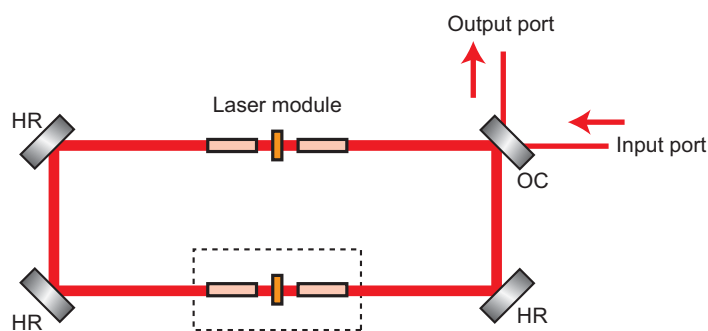


Figure 2.8: Schematic diagram of the ring cavity, which is an expanded version of the optimized linear cavity. By using another laser module (in the open square of broken line), the circulating light experiences double-pass amplification and thus the intracavity power and thermal lensing is the same as that in the linear cavity.

convex mirrors with the radius of curvature of 20 cm are used and the round trip length of the ring cavity is adjusted to coincide with that of the linear cavity by less than a few cm.

Since convex mirrors with a short radius of curvature are used in a ring cavity, the beam path of the ring cavity is folded in a zigzag shape in order to avoid astigmatism due to the reflection on the convex mirror. One of the cavity mirrors is small (half inch in diameter, 1/8 inch in thickness), and is attached to a piezo-electric transducer (PZT) with epoxy. The mirror-attached PZT is fixed to an aluminum block. The cavity length can be controlled by applying voltage to the PZT; this actuator will be used in injection locking.

The mode simulation of the ring cavity is shown in Figure 2.10. As expected, the mode size in the ring cavity is an expanded version of the linear cavity. Also, the mode is symmetric with respect to the quartz rotator, and thus the compensation for the thermal birefringence should function correctly.

Another possible configuration for the ring cavity, instead of Figure 2.9, is to use a flat mirror with partial reflectance as the output coupler. The mode matching between the ring laser and a master laser would be simple in that configuration. The reason for using an output coupler with curvature was simply a practical issue with no significant meaning.

2.5.2 Results of the ring oscillation and discussions

The output power of the ring laser in free running is shown in Figure 2.11. The maximum output power of 121 W and the optical-to-optical efficiency of 13 % were achieved. Since the maximum output power is twice of the output power from the linear cavity laser, it has been proven to be feasible to expand a linear cavity with the same parameters to a ring cavity by using two identical laser modules.

By fitting the plot of the output power with a line, the slope efficiency was found to be approximately 120%, well above the threshold, indicating that more power could be extracted as the laser output than the injected power. This result disagrees with Equation (2.3) which restricts the slope efficiency less than unity.

The result is not surprising, however, because the mode stability in this design is limited within

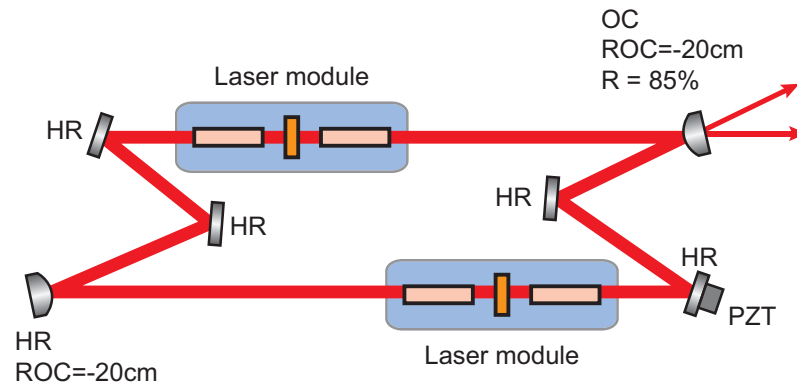


Figure 2.9: Schematic drawing of the ring laser.

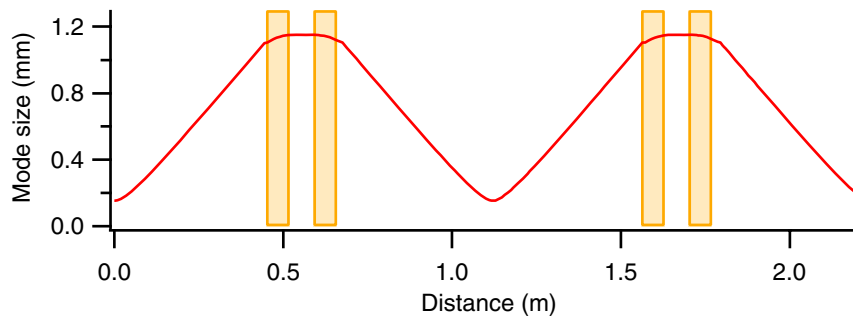


Figure 2.10: Simulation of the cavity mode for the ring cavity configuration shown in Figure 2.9.

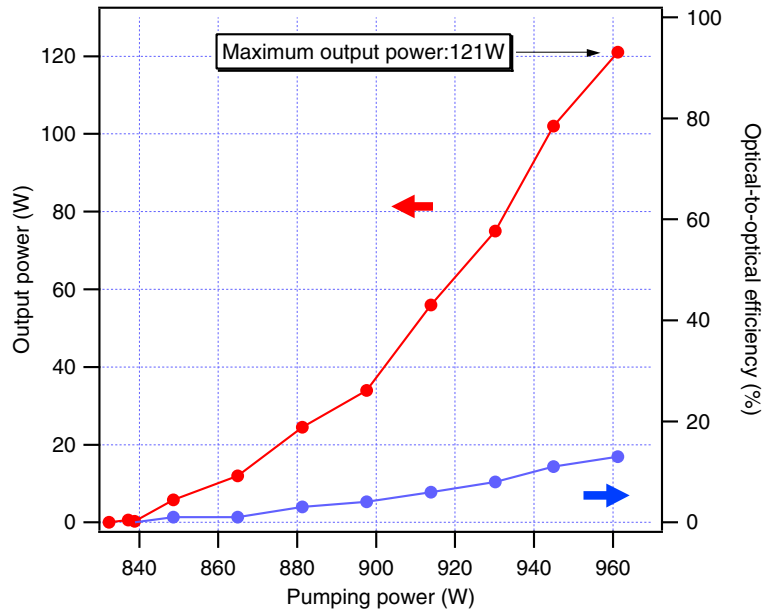


Figure 2.11: The output power of the ring laser in free running.

a narrow region of strong pumping, where the diffraction loss drastically decreases due to the thermal lensing. Therefore, the stored energy in the laser medium suddenly started to build up the laser oscillation, resulting in steep increase of the output power.

The parameters of the cavity loss δ and the overlap efficiency η_B are strong functions of the pumping power P_{pump} . The actual slope efficiency and the oscillation threshold calculated by Equation (2.3) and Equation (2.5) are thus changing according to the pumping power.

The rather low optical-to-optical efficiency of 13 % for a laser-diode pumped Nd:YAG laser is due to the design of the long laser cavity to truncate the high-order spatial modes. Since a diffraction-limited output is needed for our purpose, the decrease in the efficiency is inevitable.

Figure 2.12 shows the output power (in arbitrary units) in one of the two output ports. The power was measured by a photodetector. The result shows that the intensity of the ring cavity was quite unstable and the power was flipping many times during a period of as little as 10 seconds. This instability was caused by the gain competition between the counter-rotating waves.

The total output power stayed relatively constant when measured with a power meter with a slow response time of approximately 1 second. On the other hand, the intensity fluctuation became evident when the light from an output port was measured with a fast-response photodetector.

Intensity noise of the ring laser in free running could not be characterized for two reasons: first, the averaged output power was not determined due to the large power fluctuation (see Figure 2.12), making it impossible to calibrate a measured spectrum to the relative intensity noise; second, a measured spectrum was so chaotic and thus didn't have any structure of useful meaning.

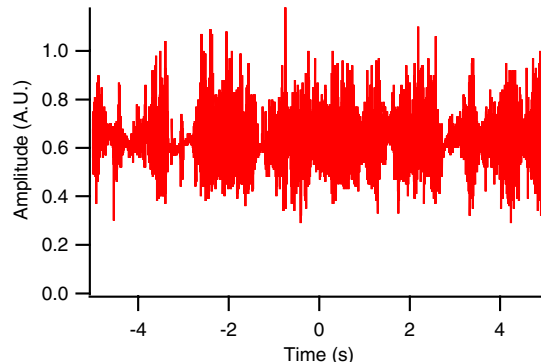


Figure 2.12: Fluctuation in the output power of the ring laser in free running measured with a photodetector.

2.6 Unidirectional operation with an intracavity Faraday rotator

When the ring cavity laser was to be characterized in free running, it was impossible to measure the output mode due to large intensity fluctuation. Since the fluctuation was caused by gain competition between the counter-rotating modes in the ring cavity, the conflicting modes should be removed to stabilize the ring laser output.

In order to suppress the gain competition and characterize the output of the ring laser, I enforced unidirectional oscillation of the ring laser by using an intracavity Faraday rotator.

2.6.1 Experimental setup

The Faraday effect rotates the polarization of light irreversibly⁹⁴; if a Faraday rotator is placed in a ring laser cavity, the polarization in a direction can be compensated by a half wave plate, whereas the polarization in the opposite direction is deteriorated. Thus, inserting a Faraday rotator causes a polarization-dependent loss and enables unidirectional oscillation suppressing the reverse wave.

A schematic diagram of the unidirectional ring laser is shown in Figure 2.13. The Faraday rotator used in this experiment was commercially available from OFR Ltd. The Faraday crystal in the device was Terbium Gallium Garnet (TGG), which has a large Verdet constant, but exhibits rather large absorption. An intracavity half wave plate was used to compensate for the Faraday rotation in one direction. As shown in the diagram, two plane-parallel plates of fused silica were placed at the Brewster angle to better discriminate the polarization-dependent loss. The open-angle geometry of the Brewster plates compensated for the deflection of the optical path due to the oblique incidence on the dielectric surface.

Two types of Faraday rotator were tested. I will refer to them as FR1 and FR2 respectively. FR1 has a large aperture of 5 mm and a small rotation angle of 3° , while FR2 has an aperture of 3 mm and a large rotation angle of 10° . Due to optical power absorption in the TGG crystal, the rotator was heated to 80°C even when it was cooled with a fin attached on the top of it.

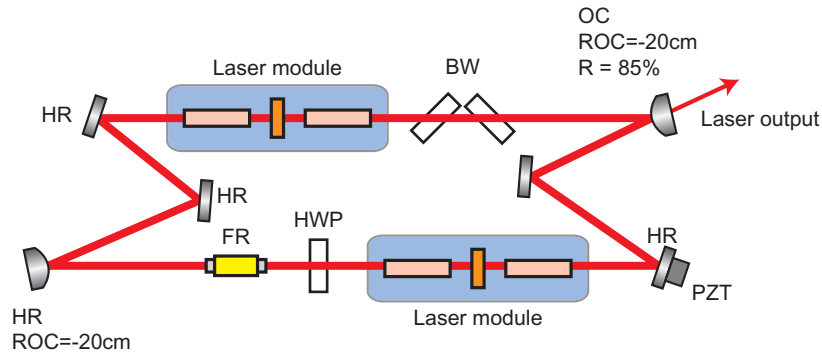


Figure 2.13: Schematic diagram of the ring cavity in unidirectional operation. FR: Faraday rotator, HWP: Half wave plate, BW: Brewster window.

According to the mode simulation of the ring cavity (see Figure 2.10), the mode size at the FRs is approximately 1.2 mm in diameter; thus, the size of the cavity mode is sufficiently small to the aperture of the FRs and no clipping by the FR aperture should result.

2.6.2 Characterization of the output

When a Faraday rotator, a half wave plate and a Brewster window were placed in the laser cavity, the reverse wave was completely suppressed and the gain competition vanished. Unidirectional oscillation was achieved by using either FR1 or FR2. As a consequence, the intensity stability was improved to the level sufficient for characterization of the output mode. Results of the measurements are summarized in Table 2.3.

	FR1	FR2
Diameter of the aperture (mm)	5	3
Rotation angle (°)	2-3	10
Output power (W)	65	46
Pumping power (W)	962	924
Optical-to-Optical efficiency (%)	6.8	5.0
M^2 in the horizontal plane	1.12	1.14
M^2 in the vertical plane	1.26	1.07
Polarization ratio	1:16	>1:100

Table 2.3: Results of the unidirectional operation of the ring laser.

2.6.3 Beam propagation profile measurements

The beam profiles of the output mode along the optical axis were measured with ModeMaster PC. The results are shown in Table 2.4. According to the results, the output modes for the FR1 and the FR2 coincides with each other.

	FR1	FR2
In the horizontal plane		
Diameter of the beam waist (mm)	0.342	0.346
Position of the beam waist from the OC (cm)	8	8
In the vertical plane		
Diameter of the beam waist (mm)	0.349	0.346
Position of the beam waist from the OC (cm)	7	6

Table 2.4: Results of beam profile measurements of the unidirectional ring laser.

2.6.4 Relative intensity noise measurement

Figure 2.14 shows relative intensity noise ($\delta P/P$) of the unidirectional ring lasers. Also shown in the graph is the intensity noise of the linear cavity laser.

According to the result, the intensity noise of the unidirectional ring laser was comparable to that of the linear laser, which indicates that the reverse wave was suppressed and the intensity noise was limited by fluctuation inherent in the laser module.

2.7 Discussions

2.7.1 Output power

The output power of the unidirectional oscillation decreased in both cases. The main causes are absorption of the Faraday crystal (specification of $\sim 1\%$), reflection loss on the surface of the wave plate ($< 0.5\%$ in total for both sides) and the reflection loss of the Brewster window. The output power decreased to 84 W for an operation with the intracavity waveplate and Brewster and without the Faraday rotator.

The discrepancy in the power decrease for FR1 and FR2 is most likely attributable to loss difference due to the crystal length of the TGG since the medium in FR2 is longer than the one in FR1. The narrower aperture for FR2 possibly contributed to additional loss, but it is not the primary factor to limit the cavity mode as explained below.

2.7.2 Spatial beam quality

The measured M^2 values for operations with FR1 and FR2 showed that the spatial modes of the unidirectional oscillation were diffraction-limited regardless of the FR apertures. This result indicates that the mode selectivity was provided by the aperture of the Nd:YAG rod itself. Although there was no internal aperture, which was inserted in the linear cavity laser, diffraction-limited oscillation was achieved. The reason is as follows:

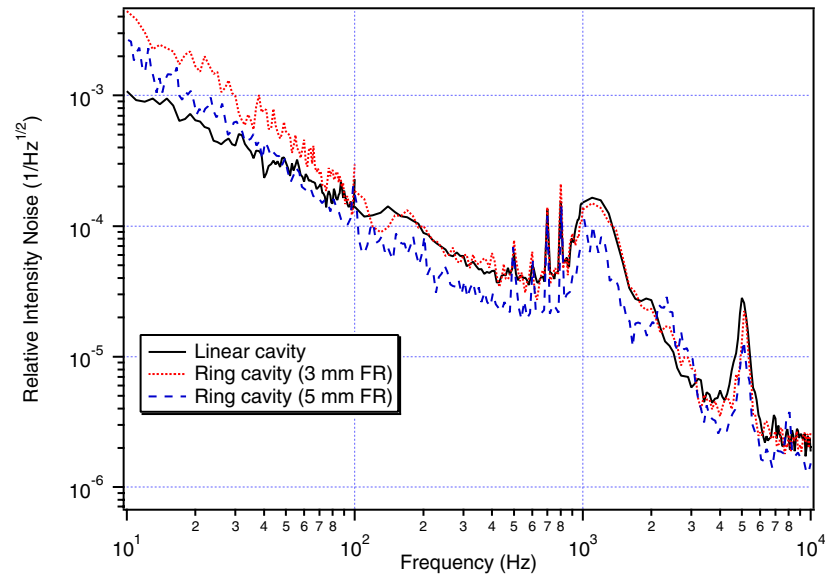


Figure 2.14: Relative intensity of the unidirectional ring laser.

Increased internal loss due to the intracavity components results in less internal power and thus decreased output power, according to Equation (2.1). A fraction of the excess power is stored as thermal load in the laser medium, which leads to stronger thermal lensing.

Figure 2.15 shows a mode simulation of the ring cavity for different thermal lensing. Stronger thermal lensing expands the cavity mode size at the rods, which clips the internal field more effectively and causes additional loss to it.

The single transverse mode was therefore achieved in the unidirectional operation due to the slight expansion of the mode size by additional thermal load, which was originated from the internal loss caused by the intracavity components.

The assumption can also explain the saturation of the power for FR2 at lower pumping power. Since the laser cavity with FR2 possessed much loss, thermal load stored in the media increased more rapidly than the laser with FR1. The pumping power was thus limited by the maximum expansion of the cavity mode at the rod aperture. Further pumping pulled the ring cavity into the unstable region.

Beam profiles for FR1 and FR2 coincided; although, the pumping power and the thermal lensing were different. The cavity mode was clamped at the point where thermal lensing and the internal loss balanced for each operation condition.

Since additional thermal load should be stored to operate in a single transverse mode without an internal aperture, this experimental result cannot conclude that the slave laser in free running is oscillating in a diffraction-limited mode. However, since the cavity mode size was proven to be comparable to the rod aperture in the experiment, the free-running mode can be expected to be almost diffraction-limited.

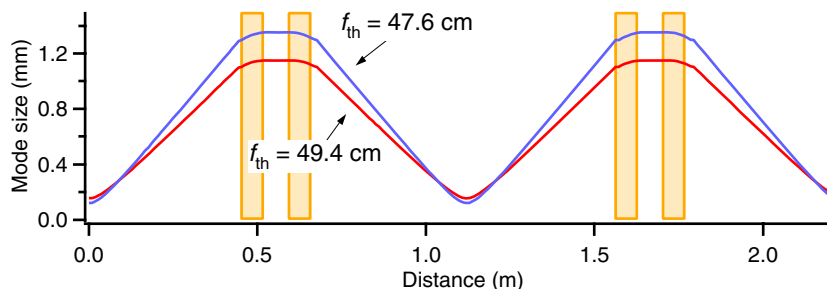


Figure 2.15: Cavity mode for different thermal lensing with focal length of f_{th} .

2.7.3 Polarization

The polarization ratio for FR2, which had larger rotation angle, was better than FR1. This is a reasonable result since the larger rotation angle provided the better discrimination of the loss between the polarization states.

However, this result doesn't lead immediately to a conclusion that an intracavity polarizer should be used to improve a polarization property because inserting optical elements lead to significant decrease of the output power in this experiment.

Since injection locking improves the polarization of a free-running ring laser, as mentioned in Section 2.2, the decision whether to use a polarizer or not should be based on results of injection locking.

2.7.4 Intensity noise

The spectra of intensity noise in the linear cavity laser and the unidirectional ring lasers were coincident with one another, showing that the intensity noise in unidirectional operation was limited by the fluctuation inherent to the laser head.

The broad peak at 1 kHz in the spectra is caused by water flow of the cooling system. The reason is as follows: Figure 2.16 shows a spectrum of acceleration, which was measured by placing a detector on a water flow divider. The water flow divider is used to divide the circulating water into two flow tubes for cooling of each Nd:YAG rod and pumping diodes in a laser module. The spectrum shows that there are large peaks appearing around 1 kHz when water circulation is turned on. Since the peaks in the acceleration spectrum agree with the broad peak in the intensity noise, the intensity fluctuation at 1 kHz can be attributed to the turbulence of the water flow.

This result indicates that fluctuation of the cooling system with water flow was coupled with the intensity fluctuation of the laser output. Since the temperature cannot be stabilized for the power level of the laser module by conduction cooling, this fluctuation is inevitable.

There is another steep peak in the spectrum at 5 kHz that appears at the same frequency regardless of cavity configurations. Although the cause has not clearly been identified, it is most likely that intensity fluctuation of pumping diodes was transferred to the output of the laser oscillation.

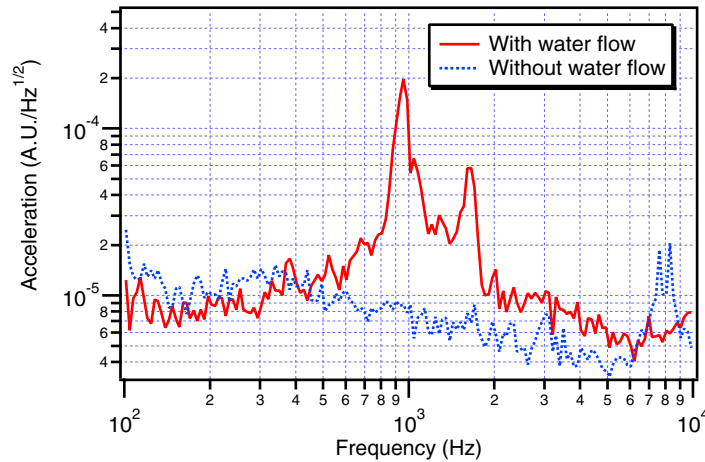


Figure 2.16: Acceleration measurements on the flow divider.

The intensity stability is $10^{-4} \text{ Hz}^{-1/2}$ at 100 Hz and the floor level rolls off by approximately f^{-1} . This level is one order of magnitude higher than the TAMA laser in free running. Since the intensity noise was invariant for different geometry (the linear cavity and the ring cavity), the intensity fluctuation in the current laser is not sensitive to the cavity length fluctuation or the mirror vibrations. Thus, little cross coupling between the intensity fluctuation and the frequency fluctuation is expected accordingly.

Only by replacing the current pumping source with a more stable pumping one can further improve the intensity stability. However, since the laser module is a commercial one and remodeling it is not a practical solution, an external modulator to stabilize the intensity is the best to achieve the required intensity stability.

2.8 Summary

I have achieved the followings:

- The 60-W, linearly polarized, diffraction-limited output from the linear cavity laser
- The ring laser with the output power of 121 W
- Unidirectional ring laser with the output power up to 65 W, whose intensity stability was limited by the intrinsic noise of the laser module

The goal to construct a 100-W ring laser of good beam quality has been fulfilled by the technique to expand an optimized linear cavity into a laser in a ring configuration.

Chapter 3

Injection locking

The ring laser was injection locked to a 2-W master laser to generate an output power of 100 W at a single frequency. The intracavity components for unidirectional oscillation were removed in this experiment because of the large power decrease caused by the loss of the components. Without aid of these devices, unidirectional oscillation was achieved by injection locking. In this chapter, details of the injection-locked laser is presented.

3.1 Theoretical model of injection locking

Theoretical models of injection locking were intensively investigated by Siegman³⁹⁾ and Farinas⁹⁵⁾ extended the discussions further. Experiments of injection locking in this work are based on these models.

Laser oscillation is in general originated from spontaneous emission in an active laser medium which grows with time by getting through stimulated emission. In injection locking, however, there is a circulating master field, which is much stronger than spontaneously emitted light. Thus, the cavity mode seeded by the strong master radiation predominantly depletes the available gain of active laser media and oscillates only at the master frequency while suppressing the other oscillating modes. This non-linear effect of extinguishing the other modes makes injection locking of great use in constructing a high-power, single-frequency laser.

3.1.1 Master equations

The master equations to describe injection locking are as follows:

$$\frac{d\tilde{E}(t)}{dt} + [\gamma_c/2 + i(\omega - \omega_c)]\tilde{E}(t) = -i\frac{\omega}{2\varepsilon}\tilde{P}(t) + \left(\frac{2\gamma_e}{\varepsilon V_c}\right)^{1/2} \tilde{E}_e(t), \quad (3.1)$$

$$\frac{d\tilde{P}(t)}{dt} + [\Delta\omega_a/2 + i(\omega - \omega_a)]\tilde{P}(t) = -i\frac{\kappa}{2\omega V_c}\Delta N(t)\tilde{E}(t), \quad (3.2)$$

$$\frac{d\Delta N(t)}{dt} + \gamma_2\Delta N(t) + R_p(t) = i\frac{V_c}{4\hbar}[\tilde{E}(t)\tilde{P}^*(t) - \tilde{E}^*(t)\tilde{P}(t)], \quad (3.3)$$

where ε is the dielectric constant of a laser medium, κ is a coupling efficiency of external signal to a polarization, \tilde{E} is injection-locked field with oscillating frequency ω , V_c is the mode volume of the

laser medium, \tilde{E}_e is injected external field, \tilde{P} is atomic polarization, ΔN is inverted population and R_p is pumping rate. ω_a and $\Delta\omega_a$ are the center frequency and the linewidth of the laser gain, respectively. The decay rate of the cavity δ_c can be expressed as $\delta_c = L_{\text{total}}/\tau$, where τ is the round-trip time and L_{total} is the total internal loss including the loss due to external coupling. The decay rate γ_e due to external coupling is T/τ , where T is the transmission of the output coupler. A perfect mode matching is assumed in the following calculations.

In Nd:YAG, atomic polarization decays much faster than internal field in a laser cavity and inverted population^{96–98}, and \tilde{P} can be derived in the form

$$\tilde{P}(t) = -i \frac{\kappa}{\omega \Delta\omega_a V_c} \frac{1}{1 + 2i(\omega - \omega_a)/\Delta\omega_a} \Delta N(t) \tilde{E}(t). \quad (3.4)$$

Next, let us consider injection of external field, or master field with oscillating frequency ω_m , which is in the form

$$\tilde{E}_e(t) \equiv E_m(t) \exp(i\phi(t)). \quad (3.5)$$

When the master field is injected into a slave cavity, the master equations yield

$$\frac{dE(t)}{dt} + \frac{\gamma_c - \gamma_0}{2} E(t) = \gamma_e E_m \cos[\phi(t) - \phi_m], \quad (3.6)$$

$$\frac{d\phi(t)}{dt} + \omega_m - \omega_s(t) = -\gamma_e \frac{E_m(t)}{E(t)} \sin[\phi(t) - \phi_m(t)], \quad (3.7)$$

$$= -\Delta\omega_{\text{lock}} \sin(\phi(t) - \phi_m(t)), \quad (3.8)$$

where a slowly varying envelope approximation was applied to reduce the master equations. $\Delta\omega_{\text{lock}}$ is the angular frequency bandwidth of the lock range, which is equivalent to Equation (1.15).

In steady state, Equation (3.8) yields

$$\omega_m - \omega_s + \Delta\omega_{\text{lock}} \sin(\Delta\phi) = 0, \quad (3.9)$$

where $\Delta\phi$ is the phase difference between the master and the slave field. In order to obtain a result of a physical meaning, the frequency of the master field and the injection-locked field should fulfill the relation

$$-\Delta\omega_{\text{lock}} \leq \omega_s - \omega_m \leq \Delta\omega_{\text{lock}}. \quad (3.10)$$

3.1.2 Locking range

Equation (3.10) predicts that the frequency of the master laser should stay within a frequency band, called a locking range, to that of the slave laser to maintain injection locking. The expression of the locking range has been already shown in Equation (1.15). There is a limitation on the power ratio of the master and the slave laser output power, as noted before.

A model of how a master laser injection locks a slave laser is depicted in Figure 3.1. Let us consider a circulating field of frequency ω in a laser cavity with a gain medium. The amplitude gain \tilde{g} of the ring cavity can be expressed in the form

$$\tilde{g}(\omega) \sim \frac{1}{\sqrt{R}} \frac{1 - R}{1 - g + ig\tau(\omega - \omega_0)}, \quad (3.11)$$

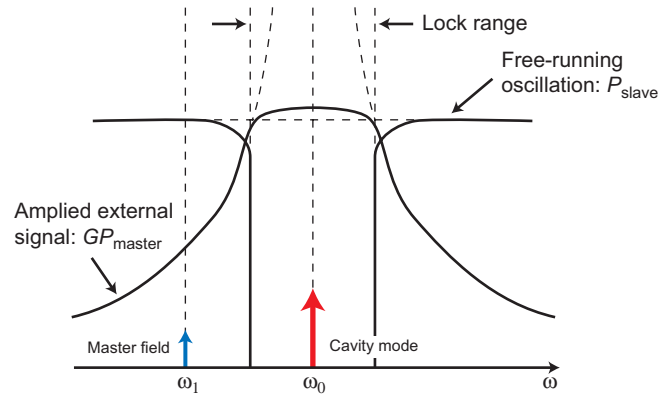


Figure 3.1: Schematic drawing of locking range (this illustration is a modified version of a drawing in the Siegman's text³⁹).

where R is the reflectivity of the output coupler, τ is the round-trip time, g is the net round-trip gain and ω_0 is the frequency of a cavity mode. In laser oscillation, the net gain g is clamped at unity and R can be approximated to be unity; as a consequence, the intensity gain $G = |\tilde{g}|^2$ can be expressed as follows:

$$G \sim \frac{\gamma^2}{(\omega - \omega_0)^2}, \quad (3.12)$$

where $\gamma = (1-R)/\tau$ is the cavity decay rate. According to Equation (3.12), the circulating field in a laser cavity will grow infinitely as the frequency of the external field gets closer to that of a cavity mode. If the frequency difference between the external signal and the cavity mode falls within the locking range, the cavity mode, which is an amplified field of the spontaneous emission, will be extinguished, and the amplified external signal will grow until the available power is all consumed on the amplification of the field.

In this description, the factor to achieve injection locking is only the frequency difference. Thus, a master laser can control the frequency of a slave laser completely as long as the frequency of the slave laser is sufficiently stable to stay close to that of the master laser. However, large fluctuation exists in a high-power slave laser. In general, a technique to stabilize the relative frequency is needed to keep the slave laser injection locked.

For a laser with an output power up to several watts, temperature control using conduction cooling is a feasible way to stabilize the frequency of a slave laser⁶⁰. However, there is limitation on this technique; for even higher-power laser the temperature cannot be controlled by conduction cooling due to large thermal load.

Thus, in this work, phase locking of a slave laser to a master laser with the Pound-Drever-Hall (PDH) technique was used to stabilize the relative frequency between the master and the slave laser. Details of the PDH technique is given in Section 3.1.5.

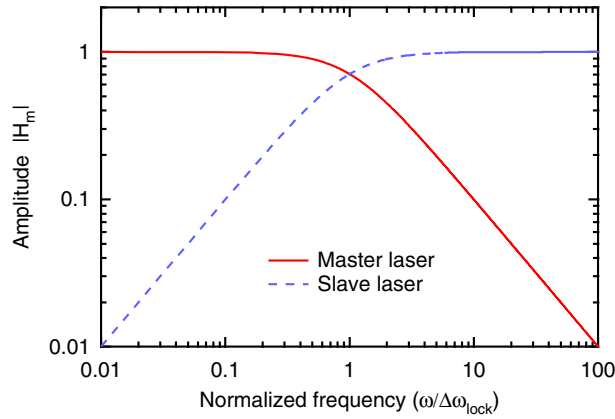


Figure 3.2: Transfer function of frequency fluctuation to the output of an injection-locked output.³⁹⁾

3.1.3 Frequency stability in injection locking

In injection locking, the frequency property of a master laser is transferred to a slave laser. The transfer function of the frequency perturbation of a master laser can be expressed as follows⁹⁵⁾:

$$H_m(\omega) = \frac{1}{1 + i \left(\frac{\omega}{\Delta\omega_{\text{lock}} \cos \Delta\phi} \right)}, \quad (3.13)$$

$$\sim \frac{1}{1 + i(\omega/\Delta\omega_{\text{lock}})}, \quad (3.14)$$

where $\Delta\phi$ is

$$\Delta\phi = \sin^{-1} \left(\frac{\omega_s - \omega_m}{\Delta\omega_{\text{lock}}} \right). \quad (3.15)$$

Since the frequency difference between the master and the slave laser can be ignored in injection locking, $\cos \Delta\phi$ can be approximated to be unity.

The frequency fluctuation of a slave laser is transferred to the frequency of the injection-locked output following the relation

$$H_s(\omega) = \frac{(\omega/\Delta\omega_{\text{lock}})}{1 + i(\omega/\Delta\omega_{\text{lock}})}. \quad (3.16)$$

Plots of these transfer functions are shown in Figure 3.2.

According to Equation (3.14) and Equation (3.16), the frequency fluctuation of the master laser is dominant at frequency below the locking range due to the low-pass filtering of the transfer function while the frequency fluctuation of the slave laser is suppressed by the high-pass filtering. Therefore, the frequency stability of an injection-locked laser should be the same as that of the master laser and frequency tuning of the master laser will be reproduced in the frequency of the injection-locked laser.

3.1.4 Intensity stability in injection locking

Intensity fluctuation of a pumping laser will appear in the output of an injection-locked laser⁹⁵). This pump-modulation transfer function can be expressed as

$$G_p(\omega) = \frac{1}{\gamma_c} \frac{\omega_{sp}^2}{\omega_{sp}^2 - \omega^2 + 2i\omega\gamma'_{sp}}, \quad (3.17)$$

where ω_{sp} is the spiking frequency of the slave laser and γ'_{sp} is the spiking decay rate. They are derived by the following relations

$$\omega_{sp}^2 \sim (r-1)\gamma_2\gamma_c, \quad (3.18)$$

$$\gamma'_{sp} \sim \frac{r\gamma_2}{2} + \gamma_e \left(r \frac{\gamma_2}{\gamma_c} + 1 \right) \sqrt{\frac{P_m}{P_s}}. \quad (3.19)$$

where r is the number of times above threshold, γ_2 is the decay rate of the upper state of the laser transition. Plots of Equation (3.17) for several power ratio P_m/P_s is shown in Figure 3.3.

The transfer function of intensity noise in the master laser to the injection locked laser output is

$$G_m(\omega) = r\gamma_2\gamma_c \sqrt{\frac{P_m}{P_s}} \frac{\left(1 + i\frac{\omega}{r\gamma_2}\right)}{\omega_{sp}^2 - \omega^2 + 2i\omega\gamma'_{sp}}. \quad (3.20)$$

Plots for Equation (3.20) are shown in Figure 3.4.

According to the theoretical predictions of Equation (3.17) and Equation (3.20), intensity noise of an injection-locked laser is determined by the slave laser within the locking range. The steep spike, or the resonant relaxation oscillation (RRO) of the slave laser, which typically appears at several hundred hertz, will be suppressed by injection locking.

On the other hand, the RRO of the master laser will be transferred to the output of the injection-locked laser with no suppression, and thus the RRO of the master laser should be suppressed before injection locking. In this experiment, the RRO of the master laser was suppressed by a built-in noise eater.

3.1.5 Pound-Drever-Hall technique

The PDH technique is used to extract a signal of the frequency difference between an optical cavity and an incident laser^{44,99,100}).

A schematic diagram of the PDH technique is shown in Figure 3.5; the electric field E_{inc} of a phase-modulated laser can be expressed as

$$E_{inc}(t) \sim E_0 \left[J_0(m)e^{i\omega t} + J_1(m)e^{i(\omega+\omega_{mod})t} - J_1(m)e^{i(\omega-\omega_{mod})t} \right], \quad (3.21)$$

where E_0 is the time-invariant amplitude of the field, $J_i(m)$ is the first-kind Bessel function of i -th order, m is the modulation depth, ω is the optical frequency and ω_{mod} is the modulation frequency. The first term on the right side of Equation (3.21) is the same component as the laser, which is called carrier, and the second and the third terms are called the upper side band and the lower side band, respectively.

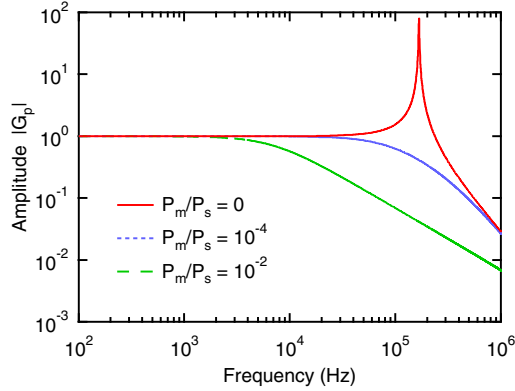


Figure 3.3: Transfer function of the pumping fluctuation of the slave laser to the output of the injection-locked laser.

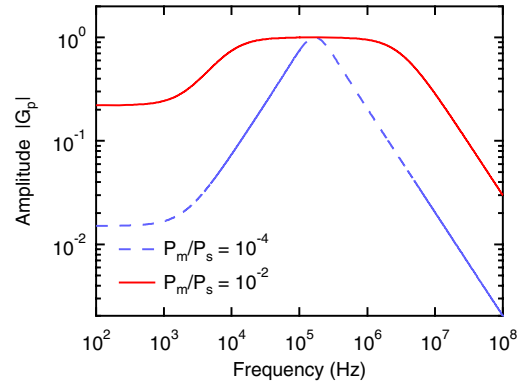


Figure 3.4: Transfer function of the intensity fluctuation of the master laser to the output of the injection-locked laser.

When the phase-modulated light is incident on an optical cavity, with linewidth much narrower than the modulation frequency, only the carrier component falls in resonance with the optical cavity while the other sidebands remain off resonant. The reflected light from the optical cavity is detected by a photodetector, as shown in Figure 3.5, and mixed by the local oscillator signal. The output signal yields

$$e(\omega) = 8\eta \sqrt{P_c P_s} \frac{\delta\nu}{\nu_{\text{FSR}}}, \quad (3.22)$$

where $\delta\nu$ is the fluctuation of the laser frequency, ν_{FSR} is the free spectral range of the optical cavity and η is a transform coefficient of a detected power into an electrical signal. According to Equation (3.22), the demodulated signal is proportional to the frequency fluctuation $\delta\nu$ and thus gives information how much the frequency of the laser fluctuates.

Figure 3.6 shows a simulation of an error signal of the PDH technique. In this simulation a linear cavity with mirrors of impedance matched amplitude reflection ($r_1 = r_2 = 0.9$) was assumed. The modulation frequency was assumed to be tenth of the free spectral range of the cavity ($\nu_{\text{mod}} = \nu_{\text{FSR}}/10$). The slope of the dispersion curve at each zero-crossing point is in the opposite sign between the carrier and the sidebands, and thus the carrier of a master laser can be locked to a cavity resonance while the sidebands are kept out of the resonance.

3.1.6 Control theory in injection locking using the PDH technique

An error signal of the frequency fluctuation can be obtained by the PDH technique, as shown in Equation (3.22). The error signal can be used to stabilize the laser frequency by amplifying and feeding back

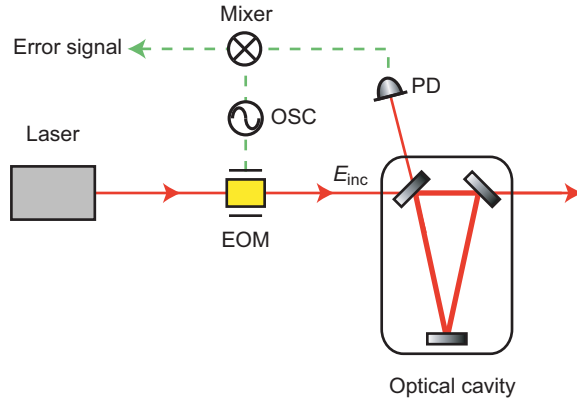


Figure 3.5: Schematic diagram of the PDH technique.

to a frequency actuator of the laser⁹⁹). A schematic diagram of the stabilization control loop is shown in Figure 3.7.

In Figure 3.7, K , G , D are the conversion coefficients of a frequency actuator of the laser, servo filter and the discriminator of the PDH technique, respectively.

The noises added to the control loop at the points of A, B and C in Figure 3.7 are referred to as $\delta\nu_{laser}$, δV_{disc} , δV_{servo} , respectively. The total noise at the output can be expressed as

$$\delta\nu = \frac{\sqrt{|\delta\nu_{laser}|^2 + |K\delta V_{servo}|^2 + |KG\delta V_{disc}|^2}}{|1 + KGD|}. \quad (3.23)$$

When the feedback gain of the open loop transfer function KGD is sufficiently larger than unity, the residual noise, which appears at the output of the stabilized laser, is

$$S \sim \frac{\delta V_{disc}}{D}. \quad (3.24)$$

Therefore, the frequency noise of an stabilized laser is determined by the noise of the discriminator and the feedback gain. In an ideal case, the discriminator noise is limited by the shot noise of the incident light in the photodetector. The spectral density of the shot noise, which is white noise, can be expressed as

$$\delta V_{disc} = R\sqrt{2} \sqrt{2e \left(2J_1^2(m) \frac{e\eta P_0}{h\nu} \right)}, \quad (3.25)$$

where R is the transimpedance of the photodetector. The shot-noise-limited fluctuation of the stabilized laser is

$$\delta\nu = \frac{\delta\nu_c}{J_0(m)} \sqrt{\frac{h\nu}{8\eta P_0}}. \quad (3.26)$$

Here, I ignored the frequency response function of the cavity because the cut off frequency is far above the frequency of our interest.

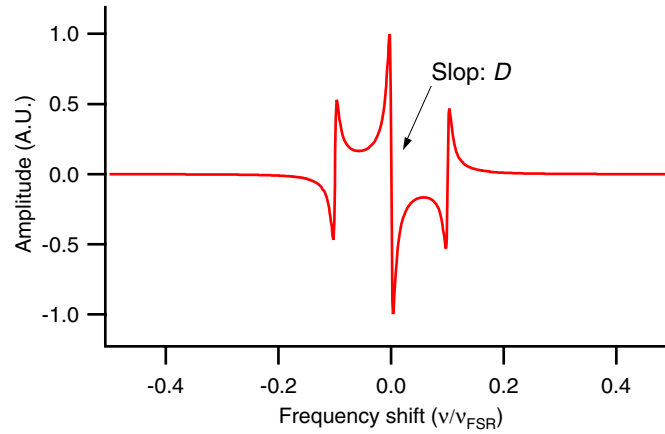


Figure 3.6: A calculated error signal of the PDH technique. The slope D is the discrimination coefficient of the PDH signal which convert the frequency shift ($\delta\nu$) to voltage.

3.1.7 Estimation of frequency stability of an optical cavity

Assuming the frequency noise $\delta\nu_{\text{laser}}$ of a laser is dominant, the signal at point C in Figure 3.7 can be expressed as

$$\delta V_C = \frac{DG\delta\nu_{\text{laser}}}{|1 + DKG|}, \quad (3.27)$$

$$\sim \frac{\delta\nu_{\text{laser}}}{K}, \quad (3.28)$$

where the feedback gain $|G|$ is sufficiently larger than unity. According to Equation (3.28), the frequency noise of the laser can be evaluated by measuring the spectrum at the actuation point and calibrating the actuation coefficient of the laser frequency with dimension of Hz V^{-1} .

This fact shows that fluctuation of a laser can be suppressed by applying a signal of the same amplitude and the opposite sign, which agrees with intuitive understanding that a number subtracted by itself makes zero.

3.1.8 Characterization of a spatial mode using a Shack-Hartmann wavefront sensor

Spatial beam quality of a laser output can be estimated by measuring wavefront distortion^{101–103}. In this work, a HASO wavefront sensor of Imagine Optic was used to evaluate the aberrations of the injection locked laser.

A Shack-Hartmann wavefront sensor uses two-dimensional microlens arrays to analyze wavefront. The microlens arrays divide wavefront into small segments and focus the pieces of the light on a detector behind the lens arrays. In this configuration, tilt of the segmented wavefront can be measured by calibrating the displacement of the focusing points. The actual wavefront of the incident laser can be reproduced by integrating the tilts over spot region on the pupil.

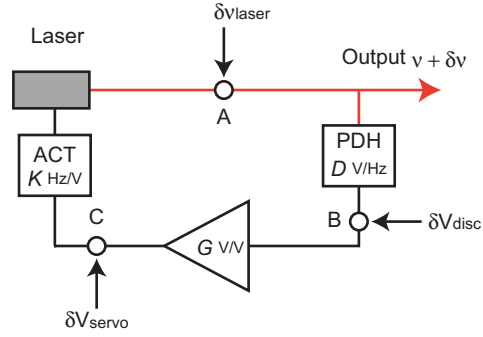


Figure 3.7: Schematic diagram of the control loop of the PDH technique in injection locking. The open square of ACT shows a frequency actuator of the laser with a transform coefficient of K with a dimension of Hz V^{-1} .

Representing wavefront with Zernike circle polynomials, which is analogous to the Seidel aberrations and has the smallest rms distribution for an aberration of a given order,* will give us a convenient way to analyze wavefront distortion¹⁰⁴.

According to the diffraction theory of aberrations, normalized intensity at a converging point, or Strehl intensity, can be expressed as

$$i \sim 1 - \left(\frac{2\pi}{\lambda}\right)^2 (\Delta\Phi)^2, \quad (3.29)$$

$$= 1 - \left(\frac{2\pi}{\lambda}\right)^2 \left(\overline{\Phi^2} - \overline{(\Phi)}^2\right), \quad (3.30)$$

where $\Delta\Phi$ is the mean-square deformation of the wavefront. Even in the case of non-uniform illumination of the pupil, Equation (3.29) can still be applied by taking into account a weighted amplitude of the deformation^{102,103}. For the case of a Gaussian beam, $\overline{\Phi^n}$ is expressed in the form

$$\overline{\Phi^n} = \frac{1}{\pi} \int_0^1 \int_0^{2\pi} \exp(-\rho^2) \Phi^n \rho d\rho d\theta, \quad (3.31)$$

where ρ is normalized with the radius of the exit pupil.

Table 3.1 summarizes formulas for tilt, focus and higher-order aberrations. Substituting each aberration into Equation (3.31) yields effective power decrease at the waist position due to the aberration, which will give us a good criterion for spatial beam quality.

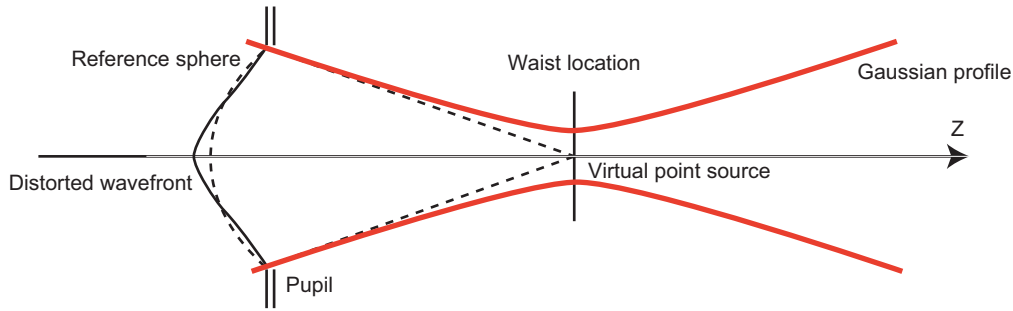


Figure 3.8: A Gaussian mode with distorted wavefront converging to a virtual point source.

3.2 Experimental setup of injection locking

The experimental setup to injection lock the 121-W slave laser to a 2-W master laser is shown in Figure 3.9.

A 2-W NPRO (Innolight, model Mephisto 2000 NE) was used as a master laser. The frequency of the NPRO can be controlled by applying voltage to the PZT, which is attached to the Nd:YAG crystal and change the frequency by pressing the crystal against the crystal mount. The Nd:YAG crystal and the diode lasers are temperature-stabilized by conduction cooling. The M^2 of the master laser was 1.11 in the horizontal plane and 1.03 in the vertical plane, which I measured with ModeMaster PC.

Two Faraday isolators, each of which consisted of a Faraday rotator (OFR) with rotation angle of 45° and two thin film plate polarizers (CVI, TFPs), were inserted to protect the master laser against the reverse wave from the free-running slave laser. The damage threshold of the TFP is 1 MW cm^{-2} , which is high enough to resist the high intensity of the optical power of the reverse wave.

The master light was phase-modulated by an EOM at a modulation frequency of 15 MHz. I used a signal generator AFG320 (Tektronix) to drive the EOM. AFG320 has two output channels with independently adjustable phase.

A mode matching lens was placed before the output coupler of the slave laser. The mode of the master laser was measured after reflected by the OC; the result is shown in Table 3.2. When compared to the results in unidirectional operation of the slave laser (see Table 2.4), the mode of the master laser matches that of the slave laser within the uncertainty of the experiment (including the tolerance of the ModeMaster PC of 5 % and uncertainty of my length measurement with a ruler).

The optical power of the master laser measured before the output coupler was 1.38 W. Throughput of the input optics was 69 %.

The parameters of the slave laser is shown in Table 3.3. The FSR was calculated by measuring the beat signal of the longitudinal modes in the output of the free-running slave laser. The reflectivity of the OC is a specification value.

Taking into account the master power of 1.38 W and the output power of 100 W of the slave laser,

*An aberration can be compensated by balancing with the lower aberrations, and expanding wavefront with the Zernike polynomials can automatically solve the balancing problem.

Order	#	Aberration	Formula
2	1	Tilt at 0°	$\rho \cos(\theta)$
	2	Tilt at 45°	$\rho \sin(\theta)$
	3	Focus	$2\rho^2 - 1$
4	4	Astigmatism at 0°	$\rho^2 \cos(2\theta)$
	5	Astigmatism at 45°	$\rho^2 \sin(2\theta)$
	6	Coma at 0°	$(3\rho^2 - 2) \cos(\theta)$
	7	Coma at 45°	$(3\rho^2 - 2) \sin(\theta)$
	8	3rd order spherical aberration	$6\rho^4 - 6\rho^2 + 1$
6	9	Trefoil at 0°	$\rho^3 \cos(3\theta)$
	10	Trefoil at 45°	$\rho^3 \sin(3\theta)$

Table 3.1: Representation of tilt, focus and higher-order aberrations. The assigned number # will be used in Section 3.6 to refer to each aberration.

the estimated lock range is

$$\Delta\omega_{\text{lock}} = \gamma_e \sqrt{\frac{P_{\text{master}}}{P_{\text{slave}}}}, \quad (3.32)$$

$$= 0.15 \times 123.7 \text{ MHz} \times \sqrt{\frac{1.38 \text{ W}}{100 \text{ W}}}, \quad (3.33)$$

which yields $\Delta\omega_{\text{lock}}/2\pi = 0.35 \text{ MHz}$; this is the half width of the full locking range and the full lock range is approximately 1 MHz for the injection locking system in this work.

The output power of the injection-locked laser was put into a power meter (Newport, model 1835 with a detector head of model 818-T) by reflecting with a mirror of 95.6-% reflection at the output port. The output power of the injection-locked laser in this thesis is calibrated by the reflection ratio to give the actual power leaving the output coupler. The leak light through the pick-off mirror was used for demodulation of the PDH technique and for analysis of the output characteristics.

A fraction of the picked-off output was detected by a photodetector and the AC signal was mixed with a local oscillator signal. The demodulation phase of the local oscillator was adjusted by tuning the settings of AFG320.

The cavity length of the slave laser was controlled by the mirror-attached PZT. A high-voltage PZT driver (Mess-Tek, model M-2663) was used to apply voltage to the PZT. The voltage range of the PZT driver is from -11 V to 170 V, the signal bandwidth is 100 kHz. The output resistor is 22 Ω , which is sufficiently low to drive the PZT with high capacitance of 285 nF (measured value).

3.3 Transfer function of stabilization loop with the PDH technique

Injection locking of the slave laser was stabilized by using the PDH technique.

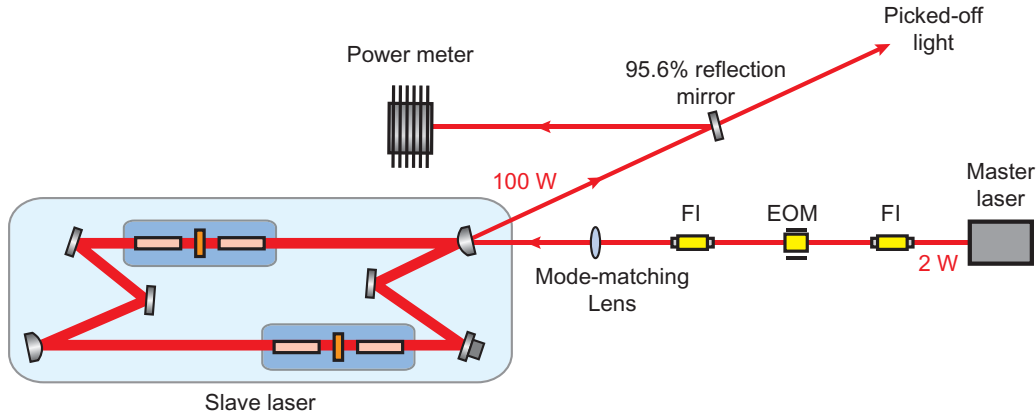


Figure 3.9: Schematic diagram of injection locking. FI: Faraday isolator, EOM: Electro-optic modulator.

		Mode of the master laser
In the horizontal plane		
Diameter of the beam waist (mm)		0.314
Position of the beam waist from the OC (cm)		7
In the vertical plane		
Diameter of the beam waist (mm)		0.322
Position of the beam waist from the OC (cm)		8

Table 3.2: Beam propagation of the master laser after reflected by the OC of the slave laser.

The error signal of injection locking is shown in Figure 3.10, which is in good agreement with the calculated signal of Figure 3.6. This signal was measured by sweeping the slave cavity by applying a triangle voltage to the PZT. Since the slave laser was operated in free running, the relative amplitude between the carrier and the sidebands were not accurate due to large intensity fluctuation of the laser output. For the same reason, the carrier and the sidebands were not separated by equal intervals, which should be the same corresponding to the modulation frequency of 15 MHz.

The open-loop transfer function of the stabilization servo is shown in Figure 3.11. Since the sinusoidal signal applied to measure the system response function was amplified by the high gain at lower frequency, making the injection-locking system unstable, the transfer function could not be measured correctly below 1 kHz. The smooth curve shown in Figure 3.11 is the designed transfer function of the servo filter, which was fitted to the measured plot with the gain as a fitting parameter. The result shows that the servo filter is working as designed.

A PZT resonance at 42 kHz, which limited the control bandwidth and gain, was suppressed by a notch filter. The transfer functions of the feedback loop with and without the notch filter are shown

FSR	123.7 MHz
Round-trip length	2.43 m
Reflectivity of the OC	85 %
Finesse	21
Linewidth	5.9 MHz

Table 3.3: Cavity parameters of the slave laser.

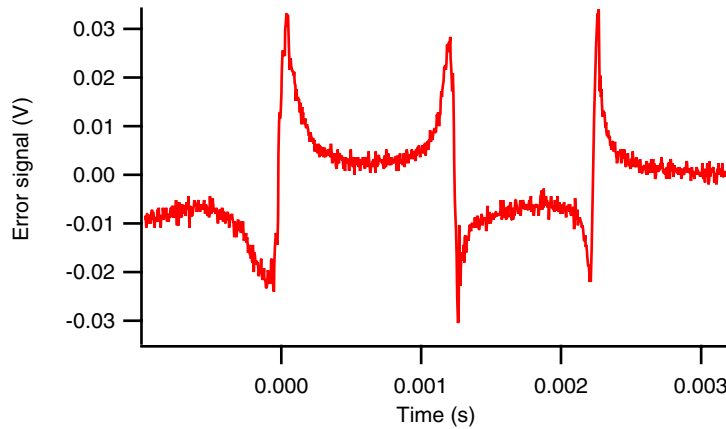


Figure 3.10: Error signal of the PDH technique for the injection locking. The bottom axis shows sweeping time.

in Figure 3.12. By suppressing the resonance peak, the gain at frequency below the resonance was increased by a factor of 2. As a result, the unity gain frequency of the control loop reached 15 kHz for the maximum gain operation.

The gain at 100 Hz was close to 80 dB (10^4 V/V), which was the limit for a filter with a slope of 40 dB/dec. The phase margin is largest at 5 kHz in the current servo, and thus I need to re-design the filter by shifting the phase margin closer to the unity gain frequency to improve the stability. The phase margin for Figure 3.11 is 10° .

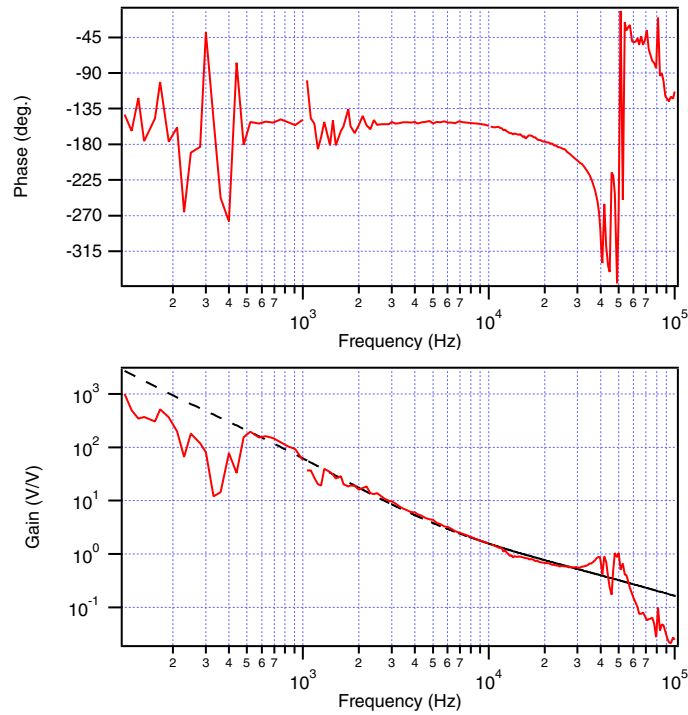


Figure 3.11: Open-loop transfer function of the stabilization loop of the injection locking using the PDH technique. Also shown in the lower graph is a fitting curve of the gain.

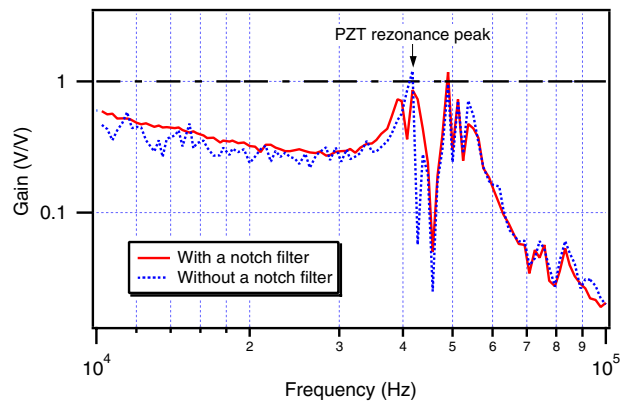


Figure 3.12: Notch filtering of the PZT resonance peak.

3.4 Frequency spectrum of the injection-locked laser

Frequency spectrum of the picked-off light from the injection-locked laser was analyzed with a scanning Fabry-Perot cavity with a Finesse of 9200, free spectral range of 46 GHz, and consists of two concave mirrors with a radius of curvature of 1 m. Transverse modes are separated by 1.15 GHz to adjacent modes.

The result is shown in Figure 3.13. The spectrum of the free-running slave laser shows multi-longitudinal mode oscillation, while the spectrum of the injection-locked laser shows that the laser is oscillating at a single frequency.

The amplitude of the trace (it is in an arbitrary unit but the same scale for the free running and the injection locking) reveals that the intensity of the free-running modes were concentrated into the injection-locked mode.

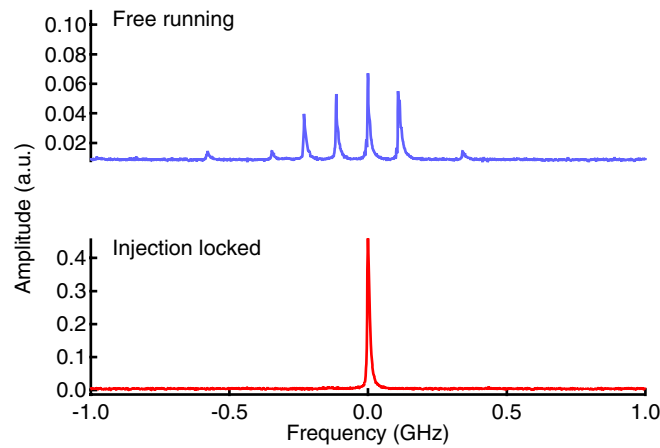


Figure 3.13: Longitudinal modes spectrum measured with a scanning Fabry-Perot cavity. The upper trace shows longitudinal modes of the slave laser in free running and the lower trace shows a longitudinal mode in injection locking.

3.5 Output power

I successfully injection-locked the slave laser to the master laser for over 10 hours. Figure 3.15 shows the time trace of the output power of the injection locked laser. Also shown in the graph are the reverse wave of the slave laser and voltage to the PZT of the slave cavity. The pumping power during the operation was 960 W and the optical-optical efficiency was 11%.

On the left edge of the PZT voltage plot, the voltage is steeply decreased: this was caused by manual tuning of the master frequency. No tuning had been made since after the frequency adjustment; the unlocks around 83 minutes were recovered spontaneously.

The output power remained over 100 W during the operation and no drift was observed. The reverse wave of the free-running slave laser was suppressed when the slave laser was injection locked. The voltage applied to the PZT shows that the frequency of the slave laser drifted during the operation.

An analysis shows that the average power for the period from 150 to 800 minutes is 105.1 W, with the rms value of the output power of 105.1 W, the standard deviation of 0.601 W, the minimum power of 102.2 W, the maximum power of 107.4 W and the peak-to-peak amplitude of 5.2 W. The slope of the output power trace is -0.00035, which supports that there was no drift of the output power.

The output power was monitored with a photodetector, whose response is much faster than the power meter; the result is shown in Figure 3.14. According to the graph, there is large fluctuation with time variation in the order of one second in the output power. The peak amplitude of the fluctuation is 15% of the DC power.

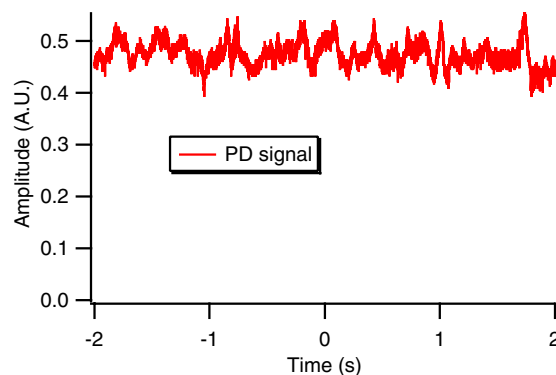


Figure 3.14: Output power as a function of time, measured by a photodetector.

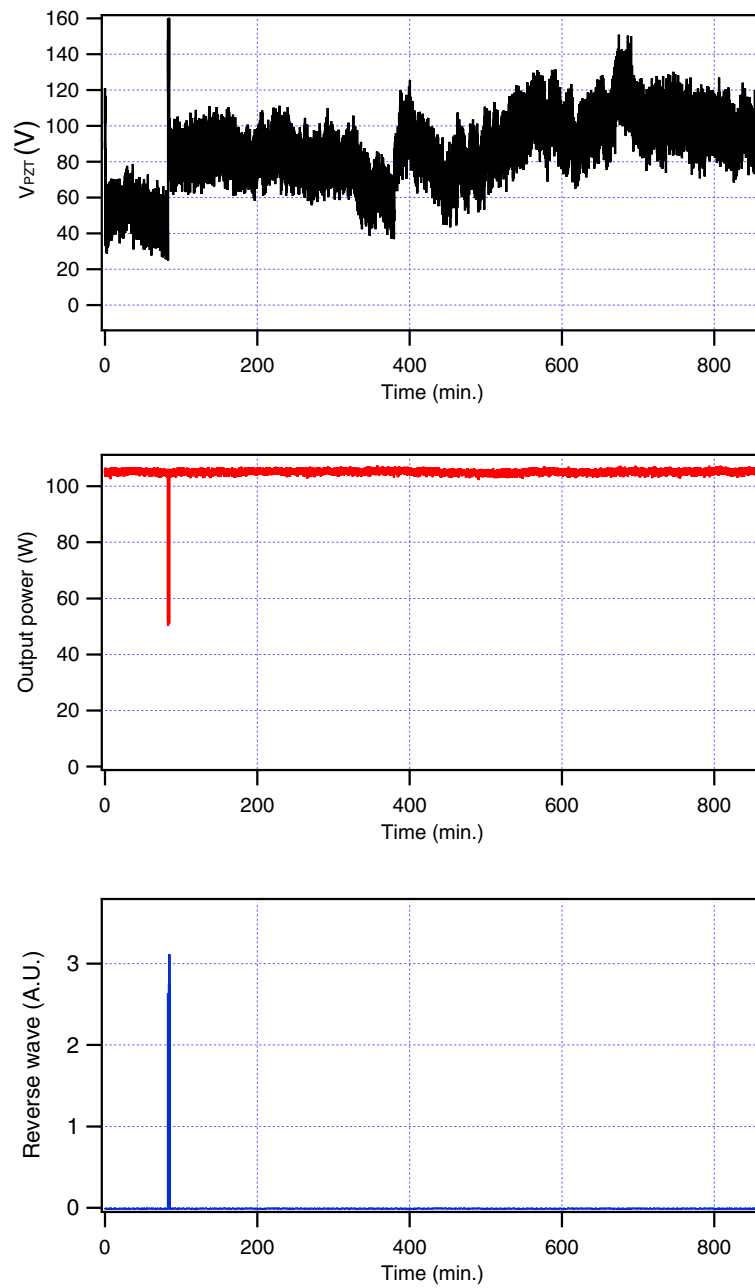


Figure 3.15: Output power (in the middle), the voltage applied to the PZT of the slave cavity (upper trace) and the reverse wave (lower trace) of the injection-locked laser.

3.6 Beam quality

The spatial mode of the injection-locked output was characterized by means of M^2 , CCD images, polarization and wavefront distortion.

3.6.1 M^2 measurement

M^2 of the injection-locked laser was measured with ModeMaster PC. A fraction of the transmitted light through the pick-off mirror (see Figure 3.9) was put into the instrument. The result is shown in Table 3.4, which proves the spatial mode of the injection-laser is diffraction-limited.

M^2 in the horizontal plane	1.11
M^2 in the vertical plane	1.13

Table 3.4: M^2 values measured for the output modes of the injection-locked laser.

3.6.2 Spatial profile

Spatial intensity distribution in the cross section of the beam was measured on a CCD camera (Spiricon): the result is shown in Figure 3.16. The beam shape is round and little distortion is observed in the image.

The beam profile in the vertical plane, which contains the intensity peak, was fitted with a Gaussian function, as shown in Figure 3.17. The result shows that the output mode of the injection-locked laser can be considered to be a fundamental Gaussian mode.

Let us define an index factor of distortion ratio $R_{\text{distortion}}$ of a Gaussian beam as

$$R_{\text{distortion}} = \frac{A_{\text{measured}} - A_{\text{fitting}}}{A_{\text{fitting}}}, \quad (3.34)$$

where A_{measured} is the measured intensity profile and A_{fitting} is the fitted profile of the Gaussian mode. Substituting the result of the fitting into Equation (3.34), the distortion ratio of the laser was less than 30% across the cross section, as shown in Figure 3.17; thus there is little distortion of the wavefront.

For comparison, CCD images of the master laser and the free-running slave laser are shown in Figure 3.18 and Figure 3.20, respectively. The distortion ratios for these lasers are less than 30% as well, and thus the profile is an ideal Gaussian.

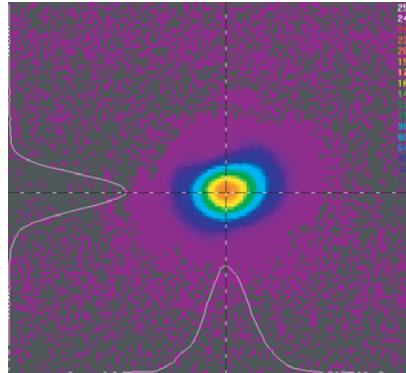


Figure 3.16: Spatial distribution of the Gaussian mode of the injection-locked laser.

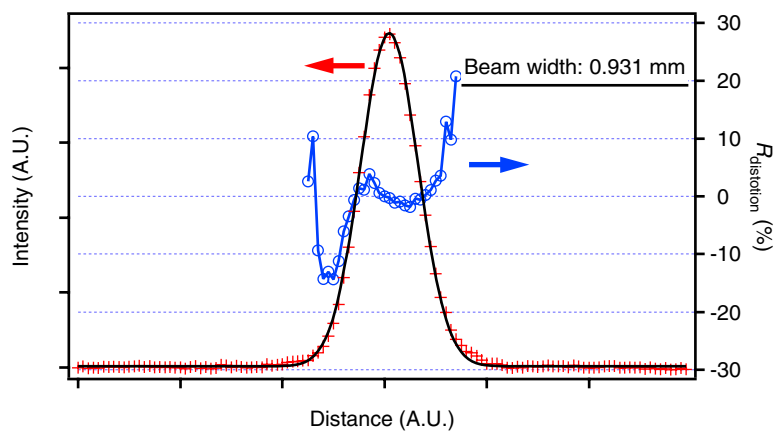


Figure 3.17: Gaussian fitting of the spatial profile of the injection-locked output at the peak value in the vertical plane.

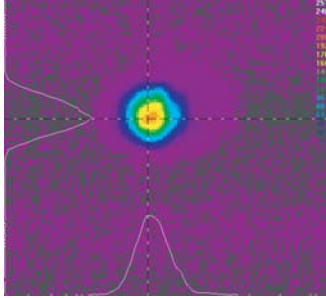


Figure 3.18: CCD image of the master laser mode.

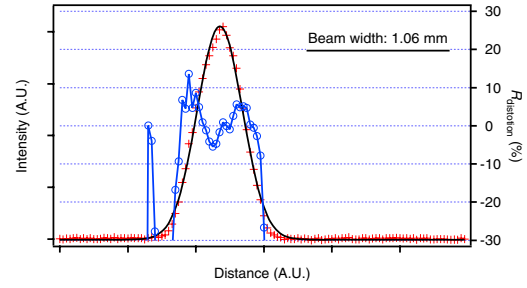


Figure 3.19: Gaussian fitting of the master laser mode.

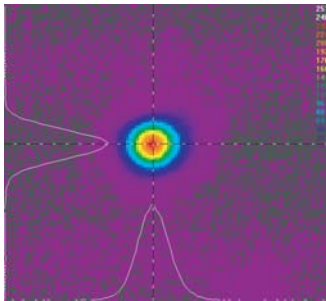


Figure 3.20: CCD image of the free-running slave laser mode.

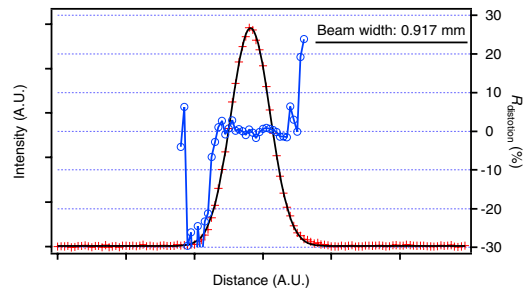


Figure 3.21: Gaussian fitting of the free-running slave laser mode.

3.6.3 Spatial mode analysis with a Shack-Hartmann wavefront sensor

Wavefront distortion of the injection-locked laser was analyzed with a HASO wavefront sensor. A fraction of the light (less than 1 mW) was picked-off and the put into the instrument. The pupil size in the measurement was 1.56 mm in diameter.

Figure 3.22 shows the result of the wavefront distortion measurement. The plot shows coefficients of Zernike polynomials to reproduce the wavefront of the laser mode. The bottom axis corresponds to the number in Table 3.1. The first three terms (tilts and focus) are not shown in Figure 3.22 since they are not aberrations.

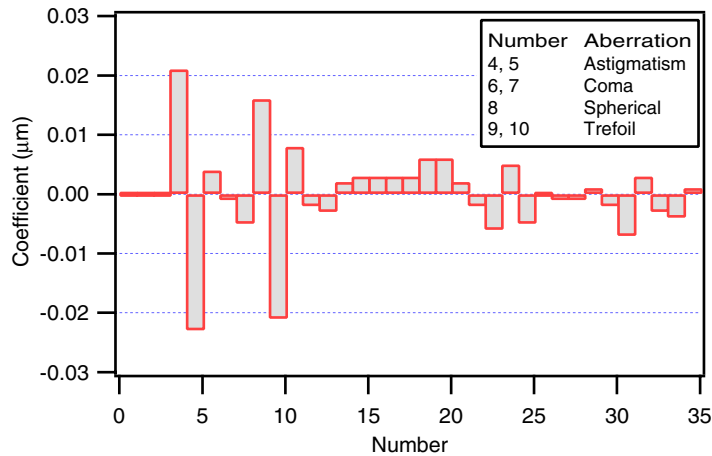


Figure 3.22: Coefficients of the Zernike polynomials for the wavefront of the injection-locked laser. Some aberrations have two coefficients, which correspond to the aberration at 0° and 45° , respectively. Coefficients for the first three terms are tilt at 0° , tilt at 45° and Focus, which are not aberrations but parameters of the reference sphere itself, and these terms are not shown.

According to the result, the aberrations are on the order of $\lambda/100$ (it is the sensitivity limit of the instrument) and thus are negligible in practice. In order to estimate the wavefront distortion, decrease of the Strehl intensity due to the aberrations was calculated for the astigmatism, coma, spherical aberration and trefoil: the result is summarized in Table 3.5.

The Strehl intensity of the laser was $1 - 0.0048 = 0.995$: thus, taking the even higher-order aberrations into account, more than 99% of the power can be effectively focused to the waist while up to 1% power will escape from the focusing point.

3.6.4 Polarization

Polarization ratio of the injection-locked laser was measured. A schematic of the experimental setup of the polarization measurement is illustrated in Figure 3.23. The polarization of picked-off light from the injection-locked output was rotated by a half wave plate, and the transmitted light of the PBS was measured with a photodetector.

Order	#	Aberration	Intensity decrease (%)
4	4	Astigmatism at 0°	0.14
	5	Astigmatism at 45°	0.17
	6	Coma at 0°	0.005
	7	Coma at 45°	0.0003
	8	3rd order spherical aberration	0.012
6	9	Trefoil at 0°	0.058
	10	Trefoil at 45°	0.10

Table 3.5: Decrease in Strehl intensity due to each aberration.

The result is shown in Figure 3.24. The error bar is half of the peak-peak amplitude of the light detected by a photodetector. Fluctuation of the injection-locked laser is so large (see Figure 3.14) that the accuracy of this measurement was limited by the intensity noise.

When the HWP was removed, the amplitude of the transmitted light matched the maximum of the curve, and thus the light was linearly polarized in the vertical plane (p-polarization).

The fitting curve of the amplitude (A) is

$$A = 0.790 + 0.763 \times \sin(0.0706 \times \theta + 3.03). \quad (3.35)$$

According to the result, the ratio of the minimum power to the maximum power is 1/58. When the intensity fluctuation, which is ~ 0.017 at the smallest amplitude at the rotation angle of 200 degrees, is taken into account, the lower limit of the polarization ratio is 1/35. The actual polarization should be equal to or better than this polarization ratio.

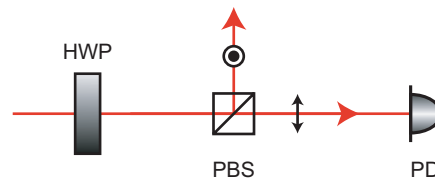


Figure 3.23: Schematic diagram of the polarization measurement. Extinction ratio of the PBS is 1:100 (specification).

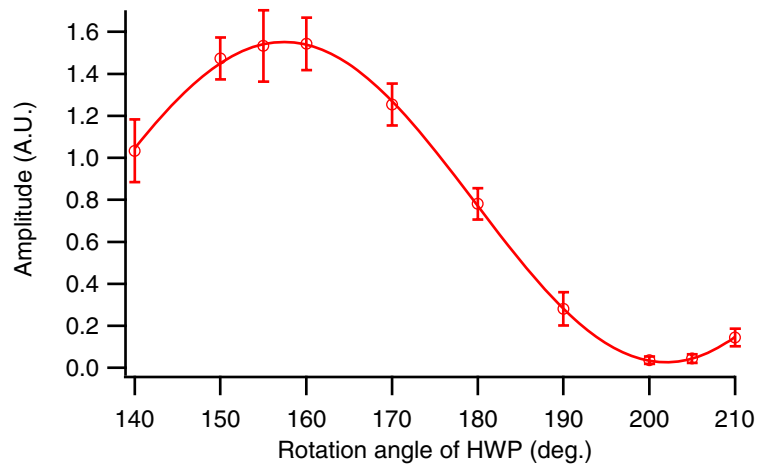


Figure 3.24: Result of the polarization measurement and a fitting curve with a sinusoidal function.

3.7 Intensity stability

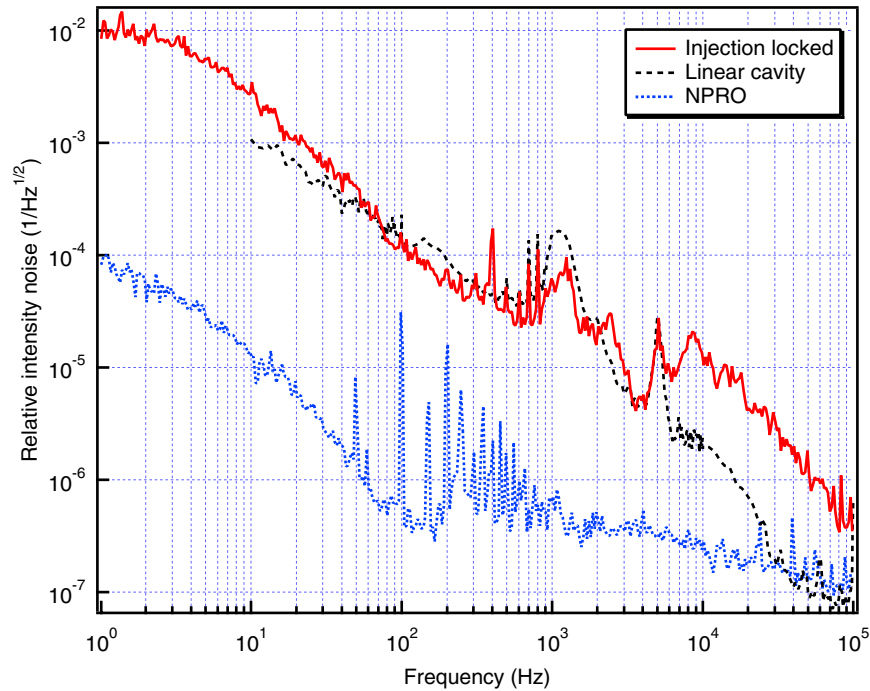


Figure 3.25: Relative intensity noise of the injection-locked laser, the linear cavity laser examined in Section 2.4 and the master laser.

Relative intensity noise (RIN) of the injection-locked laser was measured. Figure 3.25 shows the intensity noise spectrum of the injection-locked laser. Also shown in the graph is the intensity noise of the linear cavity laser and the master laser (NPRO).

The RIN of the injection-locked laser matched the RIN of the linear cavity laser. This proves that the reverse wave of the free-running slave was suppressed and the noise was limited by the inherent fluctuation of the laser module.

The peaks in the RIN of the master laser are the harmonics of the power line noise (50 Hz). The RIN of injection-locked laser is two orders higher than the RIN of the master laser.

3.8 Stability of the slave laser cavity

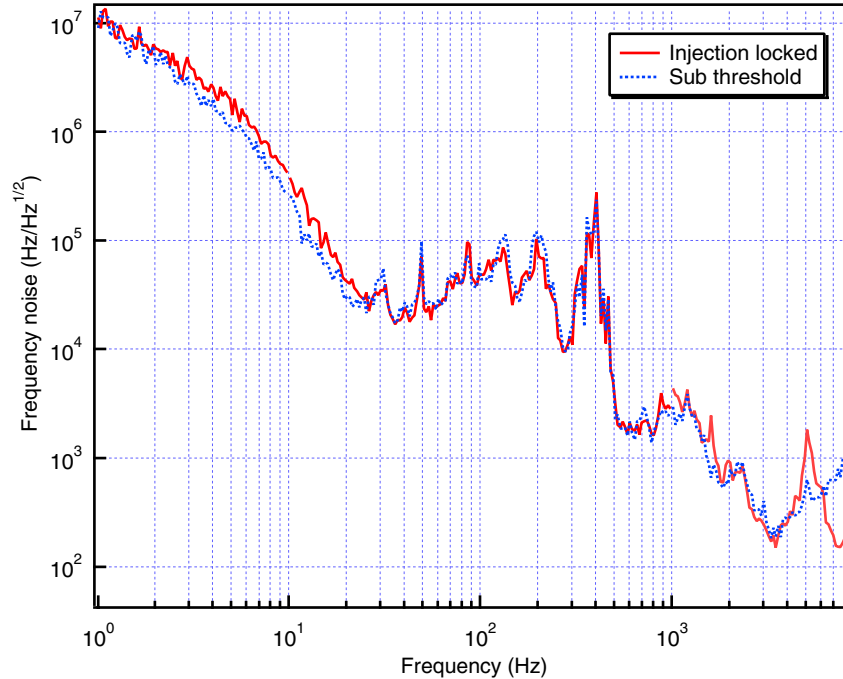


Figure 3.26: Stability of the slave cavity, which was evaluated from the signal applied to the PZT of the slave cavity.

Stability of the slave cavity was evaluated by measuring the signal applied to the PZT of the slave cavity, as discussed in Section 3.1.7.

The result is shown in Figure 3.26. The solid line plot in the graph shows the frequency stability of the slave cavity in injection locking; the broken line plot was measured below the oscillation threshold of the slave laser. Since the stability of the laser oscillation is determined by thermal lensing, the measurement for the sub-threshold condition was conducted just below the oscillation threshold. The unity gain frequency for the measurement was 8 kHz.

The transform coefficient to calibrate the voltage signal into the absolute frequency was 7.5 MHz/V. It was estimated from the frequency spectrum of the master laser transmitted through the slave laser cavity. The frequency interval between the adjacent longitudinal modes corresponds to the FSR of the slave cavity, and the voltage applied to the PZT to sweep the cavity was measured.

According to the result, the stability of the slave cavity in injection locking coincided with that for the subthreshold; that is, the fluctuation of the laser cavity was independent of the laser oscillation.

3.9 Discussions

3.9.1 Injection locking system

The 100-W slave laser was directly injection locked to the master laser; while Frede⁴¹⁾ reported a multi-stage injection locking system, which uses an intermediate 12-W laser and produces an output power of 195 W. The advantage of the direct injection of the master laser is the wide control bandwidth; the bandwidth of the frequency actuator is not limited by the preceding feedback system. Also the whole system is simple and compact without another 10-W laser.

On the other hand, the intermediate laser can increase the locking range: for the case of the 195-W laser, it is increased by a factor of 4. This leads to robustness and reliability of the injection locking, whereas it adds certain complexity to the system.

Since the performance of the 100-W injection-locked laser was confirmed to be sufficient in the experiments, there is no need to use a medium-power laser to increase the locking range at the moment. In the future, however, it could be possible to use one when the laser power is to be scaled to even higher.

3.9.2 Output power

The injection-locked laser produced an output power of 100 W: thus, the output power requirement of the first amplification stage of the LCGT laser has been fulfilled.

Injection locking was achieved only at the pumping power just above the threshold (~ 20 W for the injection-locked output) and at the operation power of the 100 W injection-locked output. In the medium pumping power region (from 20 W to 80 W for the weakly injection-locked output), the master laser could not suppress the other cavity modes completely and the reverse wave started to oscillate.

The scenario for the behavior is as follows (see Figure 3.27[†]):

In the lower pumping power region, the gain for slave cavity modes were not sufficient to survive in the presence of the strong master field and thus suppressed.

At the intermediate region, however, the mode matching between the master and the slave was not established due to the weak thermal lensing and the relatively high gain remained unconsumed in the laser materials, resulting in the reverse wave oscillation by depleting the excess gain. Since the gain distribution is different between the modes, the injection-locked mode and the reverse wave were independent of each other, and thus the both wave can exist at the same time: for this reason the cavity mode could be weakly injection-locked by the master.

The mode matching got closer to perfect at higher pumping power, and the master field started to occupy the whole gain in the media and suppressed the reverse wave.

Since the unstable geometry of the slave cavity is compensated for by the drastically changing thermal lensing, the mode matching to the master laser also changes rapidly. This is the primary factor to determine the operational point of injection locking. In this work, I designed the operational point to be achieved at the highest pumping power.

[†]This diagram is not precise, since the uncontrolled gain exists in the cross section of the laser medium, not in the beam profile along the optical path. However, it can schematically illustrate that there is uncontrolled profile in the cavity, which is sufficient for the present purpose.

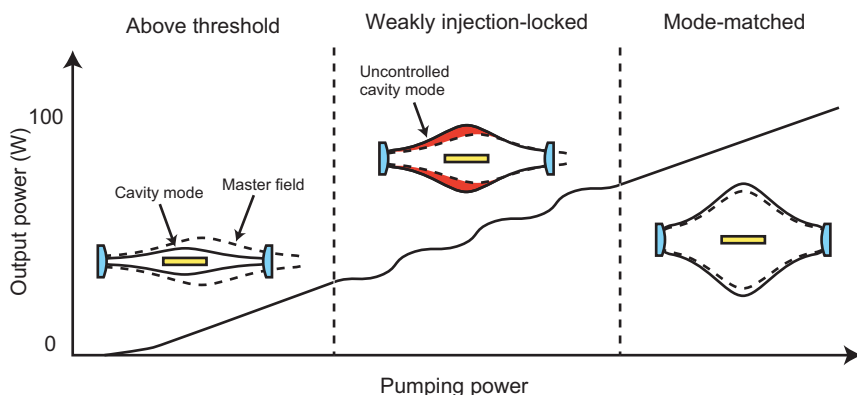


Figure 3.27: Schematic diagram of the mode matching between the master and the slave laser. In the drawings of the slave cavity, the solid curve shows beam profile of a cavity mode with sufficient gain and the broken curve shows the beam profile of the injected master laser. The internal mode of the master laser also changes according to the thermal lensing. The filled region for the weakly injection-locked condition shows the uncontrolled cavity mode, which has no overlap over the master field.

According to Siegman³⁹⁾, the output power of an injection-locked laser will increase than the total power of the free-running slave laser due to the additional power of the master laser. In this work, however, the output power did not reach the output power of 121 W. Although the reason has not been identified, a possible cause for the power drop is a mode mismatching between the master and the slave laser, including when the master controlled the slave with excellent stability at 100 W with sufficient mode matching.

3.9.3 Beam quality

The spatial beam quality of the injection-locked laser has been proven to be excellent in the experiments.

The good M^2 was achieved due to the design of the long cavity length, which was sufficient to truncate high-order Gaussian modes. According to the discussion in Section 2.7.2, additional thermal load contributes to improvement of the spatial mode quality, which was the case in the injection locking since the diffraction-limited operation was achieved without an internal aperture.

The injection-locked laser exhibits a good beam profile without mode cleaning. However, the CCD image and the profile plot of the injection-locked laser in Figure 3.16 show that the output mode has slightly distorted side lobe around the beam. The Gaussian fitting of the profile also indicates the distortion.

Although the distortion is rather exaggerated due to the small values on the periphery of the Gaussian profile, the distortion should be removed by mode cleaners. Willke³¹⁾ reported that spatial profile of a Gaussian beam can be improved by using an optical cavity, which resulted in residual distortion of

less than 1% for the stabilized Gaussian mode. The result of a mode cleaning experiment in this work is given in Section 4.4.3.

3.9.4 Polarization

The polarization ratio of the injection-locked laser was better than 1:35. The output beam was linearly polarized in the horizontal plane (p-polarization).

Injection locking was achieved only for p-polarization at the 100 W operation. Although the reason is not clear, it is most likely that the loss difference between the polarization modes determined the optimum oscillation condition and thus the output polarization. In that case, the polarization-dependent loss was caused by the oblique reflection of the six mirrors. If this assumption is true, the result indicates that the polarization of the injection-locked laser can be selected by a mirror which possesses polarization-dependent loss. Further investigation is required.

As mentioned in Section 2.7.3, another possible scheme to improve the polarization is to insert an intracavity polarizer, which could improve the output polarization to the level of 1:100. However, the polarization of the injection locking was proven to be sufficiently excellent without any intracavity elements, and can be improved by using an external polarizer. Therefore, no polarizer is needed in the slave cavity which will cause a power decrease due to the additional loss.

3.9.5 Intensity stability

The intensity noise of the injection-locked laser was characterized. The noise spectrum is comparable to that of the linear cavity (and thus the unidirectional ring laser), and two orders of magnitude higher than the master laser at 100 Hz. The intensity noise of the injection-locked laser was limited by the fluctuation of the slave laser: this is in agreement with the theoretical model discussed in Section 3.1.4.

However, since the RIN of the master laser is far below the RIN of the slave, this result is not the immediate proof of the theoretical model. If I should try to prove the model experimentally at the power level of 100 W at frequency below the RRO, I would need to use a slave laser more stable in intensity than a master laser. It is not a practical situation.

Compared to the noise level of $10^{-5} \text{ Hz}^{-1/2}$ for the TAMA laser (refer to Section 1.6.1), the noise floor for the injection-locked laser is one order of magnitude higher. Although there is certain discrepancy between the spectra, the intensity stability of the injection-locked laser can well be considered to be sufficient for the free-running performance at the output power of 100 W.

A problem to face in the future is that we should achieve a feedback gain higher than the current system by an order. In the design of the intensity stabilization (see Figure 1.6), current modulation of amplifiers are to be used to suppress the fluctuation. Further investigation is needed to prove that this technique is feasible even for a high-power laser system, in which considerable current should be modulated.

3.9.6 Frequency characteristics

The frequency stability of the slave laser cavity in free running was $10^5 \text{ Hz Hz}^{-1/2}$ at 100 Hz. This is the length fluctuation of the slave cavity itself and thus the frequency stability of the injection-locked laser should be evaluated by comparing a stable frequency reference. The result of such measurements will be presented in the next chapter.

Ottaway⁸⁰⁾ conducted a similar experiment: he evaluated the free-running frequency noise of a 5-W injection-locked ring laser, which gave $10^4 \text{ Hz Hz}^{1/2}$. The ring laser used in the experiment was temperature controlled by conduction cooling. Taking account of the difference of the configurations, the stability of the cavity of the 121-W slave laser can be considered to be good enough for the preliminary experiments.

At the lower frequency (less than 10 Hz) in Figure 3.26, the curve is steeper than a typical slope of frequency noise (f^{-1}) and thus the stability is highly degraded by environmental noise sources. Since the laser is located on an optical table in a clean booth without any covering, the optical path in the laser cavity is directly exposed to the air flow. Also the cavity mirrors are independently fixed on the optical table with conventional clamps, and thus the stability of the cavity length is limited by the fluctuations of the mirrors.

As is the same with the intensity noise, there is a broad peak around 1 kHz, caused by the coolant water flow.

The result shows that the cavity length fluctuation is independent of the laser oscillation. Thus, it is not the thermal fluctuation in the laser media, but external noise sources, such as the mirror vibration and acoustic noise, that determines the stability of the slave laser cavity.

Monolithic structure of a laser cavity was found to be effective to improve the cavity stability⁵⁶⁾. The slave laser will therefore be constructed in a monolithic structure in the future.

Figure 3.28 shows a transfer function measured for the sub-threshold oscillation (broken curve) together with the result of the injection locking (the same as Figure 3.11). According to the result, the transfer functions were not changed between injection locking and sub-threshold oscillation.

Frequency behavior of an injection-locked laser was discussed in Section 3.1.3. According to the theory, the master laser controls the frequency property of the injection-locked output within the locking range. Since the locking range in this work is $\omega_{\text{lock}}/2\pi = 0.35 \text{ MHz}$, which is much larger than the bandwidth of 10 kHz for the control servo, there was no difference between the transfer functions.

If we are supposed to increase the control bandwidth for injection locking to several hundred kilohertz, the locking range should be increased as well to expand the available frequency band. Hence, the wider locking range is also desirable in this perspective and the power ratio $P_{\text{master}}/P_{\text{slave}}$ cannot take a small value for this reason.

3.10 Summary

I have achieved the following performances of the laser:

- CW operation with an output power of 100 W
- Single-frequency oscillation

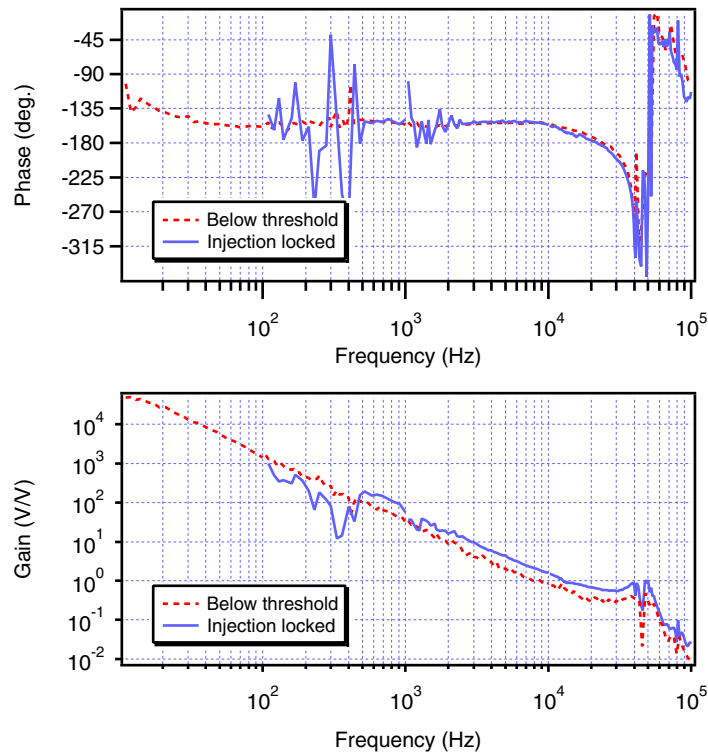


Figure 3.28: Comparison of the transfer functions for below-threshold and the injection-locked operation.

- Spatial beam quality of diffraction limit ($M_{\text{hor}}^2 = 1.11$, $M_{\text{ver}}^2 = 1.13$)
- Linearly polarized in the horizontal plane at the polarization ratio better than 1:35
- Intensity stability of $10^{-4} \text{ Hz}^{-1/2}$ at 100 Hz

Compared to the list in Section 1.5, all requirements except the intensity noise have been fully achieved. Though the intensity stability was not totally comparable to the current lasers, the performance is sufficient for future stabilization experiments. Characterization of the frequency performance will be presented in the following chapter.

Chapter 4

Frequency stabilization

I have succeeded in injection locking the slave laser to the master laser, generating an output power of 100 W. The output power is sufficient for the first amplification stage of the LCGT laser design (see Figure 1.6).

In order to investigate the laser performance, I measured frequency stability of the injection-locked laser by frequency locking to an optical cavity. Results of the frequency stabilization experiments are presented in this chapter.

4.1 Theoretical model of frequency stabilization

Frequency of a laser can be stabilized by locking to a stable optical cavity. Figure 4.1 shows a schematic diagram for frequency stabilization of a laser.

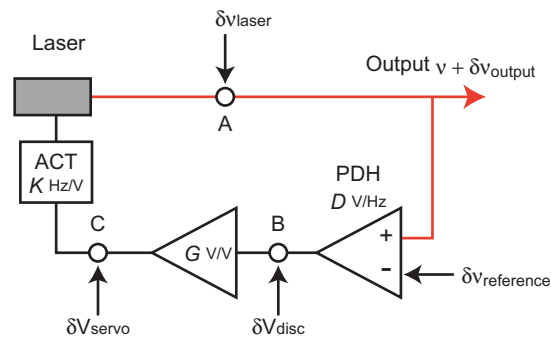


Figure 4.1: Schematic diagram of frequency stabilization. This diagram is the same as Figure 3.7 except that frequency stability of the reference is taken into account.

In Figure 4.1, the frequency stability of a laser ($\delta\nu_{\text{laser}}$) is compared to that of a frequency reference ($\delta\nu_{\text{reference}}$) with the PDH technique, which yields an error signal of the frequency fluctuation with respect to the frequency reference. The error signal is amplified by an electrical servo and fed back to

an actuator of the laser frequency.

The frequency stability of the laser output ($\delta\nu_{\text{output}}$) in this feedback system is expressed in the form

$$\delta\nu_{\text{output}} \sim \frac{\delta\nu_{\text{laser}}}{G} - \delta\nu_{\text{reference}} + \delta\nu_{\text{shot}}, \quad (4.1)$$

within the feedback bandwidth. $\delta\nu_{\text{shot}}$ is the detection noise determined by the shot noise.

The first term on the right side in Equation (4.1) shows that the frequency noise of the laser can be suppressed by the feedback gain; and thus, G should be as large as possible. The second term is the frequency stability of the frequency reference, which limits the total frequency stability. Thus we need to use a highly stable frequency reference in stabilizing the laser frequency as well as design a feedback system with a high gain G .

Fluctuation of the laser frequency without stabilization can be evaluated from the signal at the actuating point (the point C in the diagram)^{80, 105}. At frequencies where the feedback gain is sufficiently larger than unity, the voltage signal (V_{act}) can be approximated as

$$V_{\text{act}} = \frac{GD(\delta\nu_{\text{laser}} - \delta\nu_{\text{reference}})}{|1 + KGD|}, \quad (4.2)$$

$$\sim \frac{\delta\nu_{\text{laser}}}{K}. \quad (4.3)$$

Here, $\delta\nu_{\text{reference}}$ was ignored because the frequency stability of the reference should be better than the unstabilized laser ($\delta\nu_{\text{reference}} \ll \delta\nu_{\text{laser}}$). Equation (4.3) indicates that the unstabilized frequency noise is calculable from the actuator voltage V_{act} and the coefficient K .

The theoretical limit of frequency stabilization with an optical cavity is determined by the shot noise of the laser, expressed in the form

$$\delta\nu_{\text{shot}} = \Delta\nu_{\text{ref}} \sqrt{\frac{h\nu}{8\eta P}}, \quad (4.4)$$

where P is the incident power of the optical cavity and $\Delta\nu_{\text{ref}}$ is the linewidth of the reference. According to Equation (4.4), the theoretical limit of frequency stability depends on the linewidth of the cavity and the incident power of the laser; thus, either narrowing the linewidth or increasing the laser power can lower the limit. In order to achieve the narrower linewidth, it is necessary to use an optical cavity with a higher Finesse or longer cavity length.

In general, the optical cavity used in a stabilization experiment possesses a high Finesse and is vulnerable to environmental perturbations due to the high sensitivity. Possible causes to deteriorate the stability of a frequency reference $\delta\nu_{\text{reference}}$ are thermal fluctuation, acoustic noise and seismic noise. The optical cavity to be used for frequency stabilization should therefore be isolated from these fluctuations.

4.2 Purpose of frequency stabilization in this work

In the current design of the LCGT interferometer (see Figure 1.3), two mode cleaners with long baseline will be used as frequency references. As stated in Section 4.1, a longer baseline will give narrower linewidth and thus a lower theoretical limit due to the shot noise.

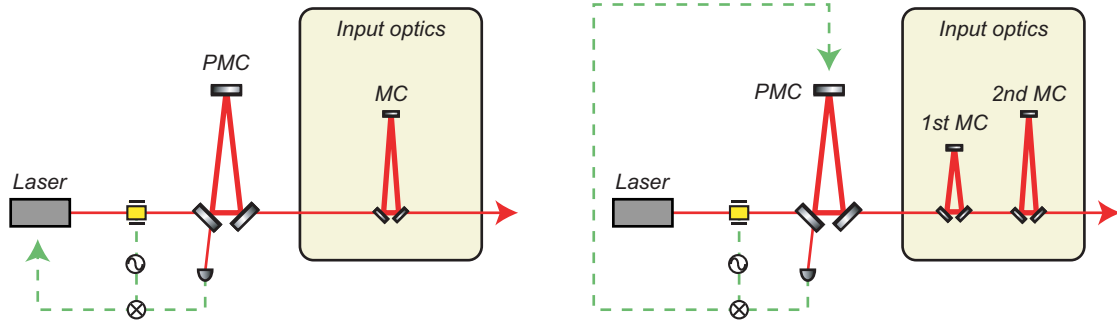


Figure 4.2: Schematic diagrams of the possible configurations for a premode cleaner in the LCGT interferometer.

However, there is another proposal¹⁶⁾ to use a short-baseline optical cavity, called a premode cleaner (PMC), to stabilize frequency of the LCGT laser. Schematic diagrams of the LCGT interferometer with a PMC are shown in Figure 4.2.

There are two possible topologies for the frequency control with the PMC: (1) The error signal of the PDH technique is fed back to the laser, or the laser is frequency-stabilized to the PMC. The PMC provides an alternative frequency reference and thus can replace one of the mode cleaners. (2) The error signal is fed back to a frequency actuator of the PMC. The PMC is controlled by the laser frequency stability and thus only the mode cleaning effect can be achieved in this topology.

Although linewidth will become broader for a shorter round-trip length, a premode cleaner has the advantages of as follows:

1. Higher stability at lower frequency (less than a few hertz) than long-baseline cavities with suspended mirrors
2. Suppression of intensity noise at RF modulation frequency (\sim MHz)
3. Wide control bandwidth due to the large linewidth
4. Improvement of pointing stability
5. Compact and simple to handle

Higher stability at low frequency can be expected due to the monolithic structure of a PMC. A spacer made of a low-expansion material causes little drift and hence the stability can be improved. A glass-ceramic compound material, ULE, which has an expansion coefficient of less than 3×10^{-8} /K, is a promising material for the spacer of the PMC. In contrast to the PMC architecture, thermally induced drift of the cavity length is inevitable for an optical cavity whose mirrors are independently suspended.

Also, a PMC has the advantage of reducing intensity fluctuation at RF frequencies^{31,106)}. The transfer function of the amplitude of an electric field can be expressed as

$$H_{\text{amplitude}} = \frac{1}{1 + i2\omega/\Delta\omega}, \quad (4.5)$$

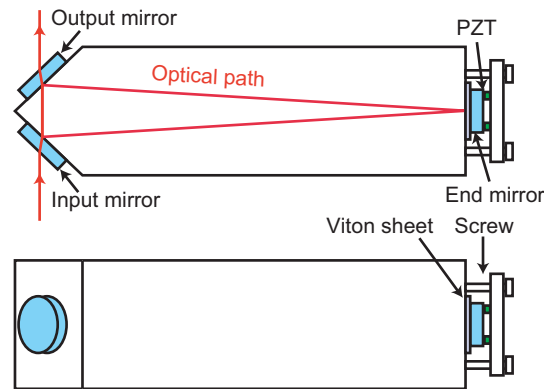


Figure 4.3: Schematic drawing of the premode cleaner. The spacer has the dimensions of 20 cm in length, 50 cm in height and 60 cm in width and is tabletop size.

where $\Delta\omega/2$ is the half linewidth of the optical cavity. Intensity of power fluctuation can be suppressed according to

$$H_{\text{intensity}} = \frac{1}{1 + (2\omega/\Delta\omega)^2}. \quad (4.6)$$

When a PMC with a half linewidth of 100 kHz is used to phase lock a laser, intensity noise at RF frequency (10 MHz) will be suppressed by a factor of 10^4 . As mentioned in Section 1.4.3, the intensity noise at RF frequency will appear at the output signal by coupling with rms fluctuation of the main interferometer, and therefore the intensity noise of the laser should be suppressed before the phase modulation.

Due to the short round-trip length (L), the large FSR is an advantage from the viewpoint of a wide control bandwidth; whereas the same reason makes PMC vulnerable to environmental perturbation as the frequency fluctuation is increased according to $\delta L/L$.

4.3 PMC

4.3.1 Cavity design

Figure 4.3 shows the design of the PMC used in this work. It consists of three mirrors and a spacer made of super invar. Three PZTs support the end mirror by pressing it against the cavity spacer. A 1-mm thick Viton rubber is put between the spacer and the end mirror. The PZTs are used to sweep the cavity length.

Although the design would be similar to the PMC in this work, another PMC would be actually used in LCGT, if to be installed. In that case, the cavity spacer should be made of ULE instead of super invar. The PMC in this work is only for the preliminary experiments to study the laser performance and the cavity characteristics.

Parameters of the PMC		
Round-trip length (designed)	$L =$	42 cm
Round-trip time	$\tau =$	1.4 ns
FSR	$\nu_{\text{FSR}} =$	714 MHz
Radius of curvature of the end mirror (designed)	$R =$	30 cm
Rayleigh range	$z_R =$	0.137 m
Waist size of the cavity mode in diameter	$2w_0 =$	0.431 mm
Linewidth for p-polarization (measured)	$\Delta\nu_p =$	3.24 MHz
Finesse	$\mathcal{F}_p =$	220
Reflectivity of the cavity mirrors for p-polarization	$R_p =$	0.986
Linewidth for s-polarization (measured)	$\Delta\nu_s =$	0.253 MHz
Finesse	$\mathcal{F}_s =$	2900
Reflectivity of the cavity mirrors for s-polarization	$R_s =$	0.999
Frequency interval between adjacent transverse modes	$\delta\nu_{\text{TM}} =$	112 MHz
Equivalent phase shift	$\delta\phi =$	0.99 rad

Table 4.1: Parameters of the PMC.

4.3.2 Preliminary tests with the PMC using the master laser

PMC performances were characterized with the NPRO, or the master laser of the injection locking. Parameters of the PMC are summarized in Table 4.1.

Figure 4.4 shows reflected light spectra of the PMC. Since NPRO typically has linewidth of at worst 10 kHz, Figure 4.4 is the spectra of the cavity itself. The transmission ratios evaluated by the spectra are 86% for p polarization and 77% for s polarization.

Transmitted light spectra for s- and p-polarized light are shown in Figure 4.5. The linewidth for the s- and p-polarized light is 0.253 MHz and 3.24 MHz, respectively. The finesse for s polarization \mathcal{F}_s is 2900, and for p polarization is $\mathcal{F}_p = 220$. Total reflection of the mirrors is 98.6% for p polarization and 99.9% for s polarization.

The total transmission efficiency of a cavity (η_{tr}) can be expressed by the relation

$$\eta_{\text{tr}} = \left(\frac{T}{T + A} \right)^2, \quad (4.7)$$

where T is total intensity transmittance of the constituent mirrors and A is the total intensity loss. Substituting the PMC parameters into Equation (4.7) yields the cavity loss: 140 ppm for s polarization and 1100 ppm for p polarization. Since the cavity loss is estimated by the reflection spectrum, the calculation gives only the order of the actual loss: more precise cavity transmission should be estimated with the transmission spectrum. Also power distribution among the higher-order modes and the sidebands should be taken into account to precisely calculate the transmission ratio.

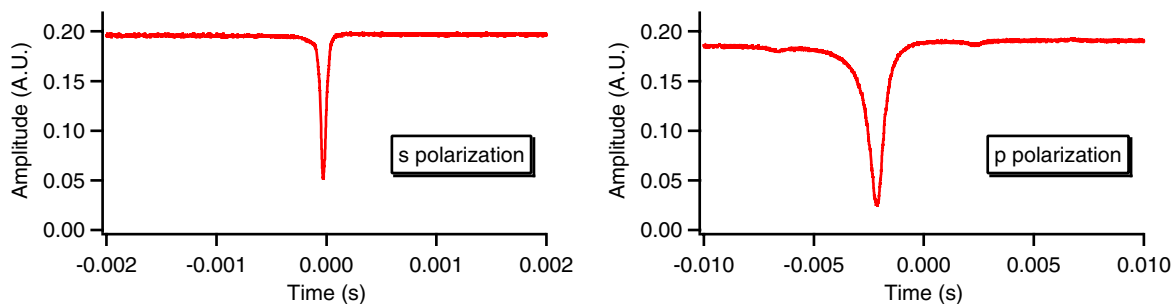


Figure 4.4: Reflected light from the PMC for s-polarized (left) and p-polarized (right) master laser.

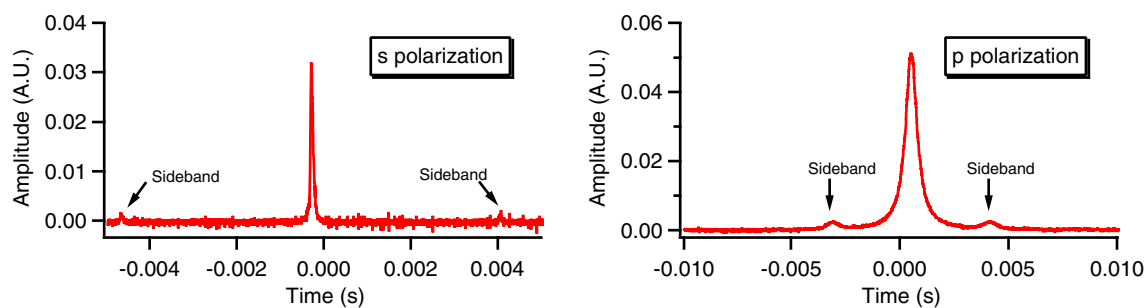


Figure 4.5: spectra of transmitted light of the master laser, which were measured for s-polarized (left) and p-polarized (right) light. There are 18-MHz sidebands on both sides for each spectrum. The linewidth can be calibrated by the frequency interval to the sidebands.

Figure 4.6 shows a spatial beam profile of the transmitted master laser. Compared to the profile before transmitting (see Figure 3.19), $R_{\text{distortion}}$ got slightly better to achieve the distortion range of $\pm 10\%$.

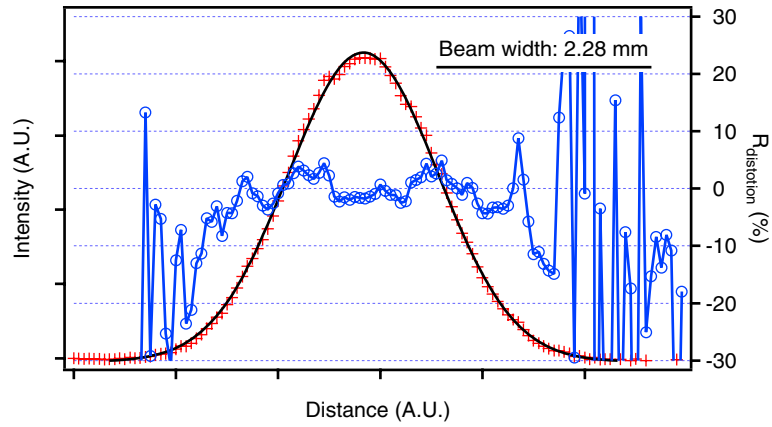


Figure 4.6: Spatial distribution of the master laser after transmitting through the PMC.

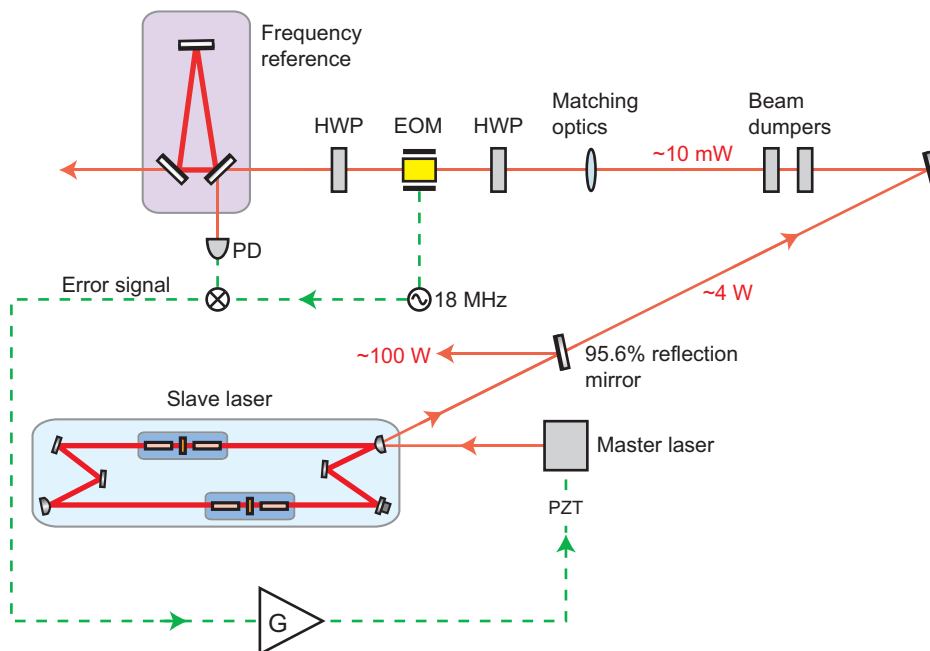


Figure 4.7: Experimental setup of the frequency stabilization experiment.

4.4 Experiment

The 100-W injection-locked laser was stabilized to the PMC and characterized in terms of frequency stability.

4.4.1 Experimental setup

A schematic diagram of the experimental setup for frequency stabilization is shown in Figure 4.7.

The 100-W output of the injection-locked laser was picked off by a mirror with 95.6% reflectivity and the light was attenuated further by partial reflectance mirrors (illustrated as beam dumpers in the diagram) to the 10-mW power level. The Gaussian profile of the light was transformed by a mode-matching lens in order to match the PMC mode.

The incident light into the PMC was phase-modulated at 18 MHz for the PDH technique. An EOM (NovaPhase) was used to impose the phase modulation. The HWP in front of the EOM was used to adjust the incident polarization to the modulator polarization (s polarization), and the HWP after the EOM was to rotate the incident polarization into the PMC (either s- and p-polarized). I used a signal generator from Tektronix model AFG3022, which has two output channels with independent phase adjustment, to drive the EOM. The demodulation phase was adjusted by changing the oscillation phase of the signal generator.

The error signal of the PDH technique was amplified by servo filters and fed back to the PZT of the master laser. The frequency actuator of the NPRO has modulation coefficient of approximately 1

MHz/V and a bandwidth of more than 100 kHz. A PZT driver of model F30PV (FLC Electronics) was used to apply voltage. It has a voltage range of ± 35 V and a wide bandwidth of a few megahertz.

In order to facilitate the locking procedure, a certain DC voltage was applied to the PMC PZTs to sweep the resonant frequency and find a TEM₀₀ mode. One of the three output channels of the Mess-Tek PZT driver, the one used for the injection locking, was used to generate the DC voltage up to 150 V.

At first, the PMC was located on a rubber-metal stack, which sat on an optical table, where the cavity was exposed to the air flow of the clean booth. Experimental results taken in this condition showed highly degraded frequency stability of the PMC, as shown in Figure 4.8. The plots are the frequency noise spectra of the master laser for the measurement in the air (upper curve) and in vacuum (lower curve). Comparing the spectra reveals that the upper curve is limited by the PMC stability, not by the laser.

In order to circumvent the degradation of the frequency stability, the PMC was housed in a vacuum chamber to isolate it from acoustic noises. A rotary pump was used to evacuate the chamber to achieve less than 10 Pa. It was turned off during the measurements of the frequency stability.

In addition to the vacuum environment, the PMC was located on a two-stage metal spring to isolate seismic motions. Since the spring was installed without any dampers, the spring oscillation at 6 Hz did not decay easily once it was excited. The resonance oscillation of the spring deteriorated the beam pointing of the transmitted light, which was observed by monitoring CCD images of the transmitted light.

Since external noises were found to degrade the PMC stability seriously, the experimental results shown hereafter were all measured in vacuum and on the seismic isolation system.

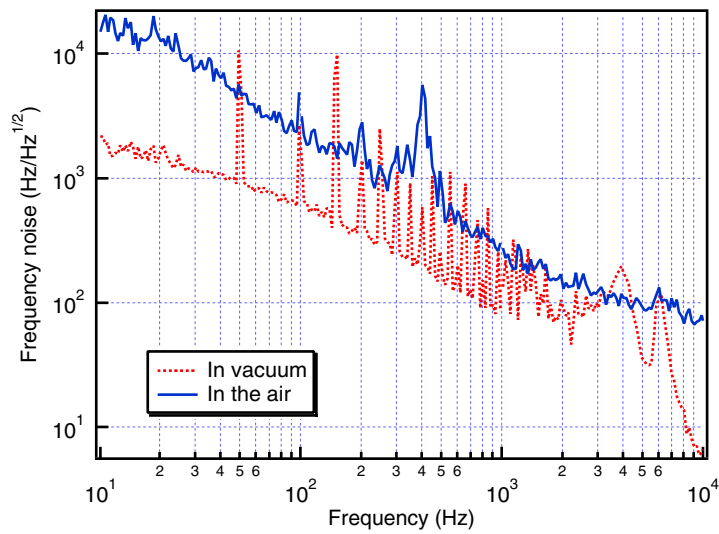


Figure 4.8: Frequency noise spectra of the master laser (s polarization): when the PMC was placed in the air (upper trace) and in the vacuum chamber (lower trace). This result shows that the frequency noise is determined by the frequency stability of the PMC, not by the laser frequency.

4.4.2 PDH signal

Error signals for s- and p-polarized light for the PMC using the PDH technique are shown in Figure 4.9 and Figure 4.10, respectively. The discrimination coefficient D_{disc} V/Hz corresponds to the slope of the zero-crossing line in the carrier resonance. The slope depends on the optical power, modulation depth and amplitude of the local oscillator signal; thus, stabilized frequency spectra were calibrated by each PDH signal slope.

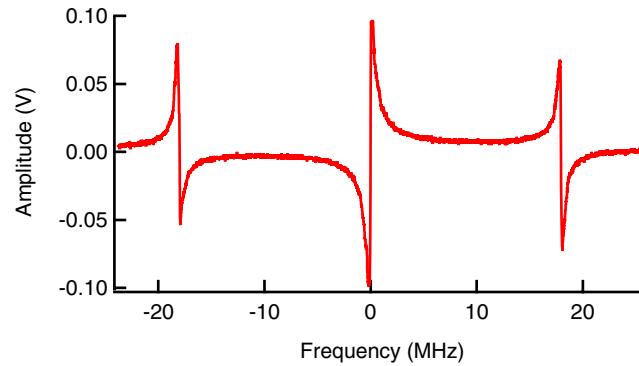


Figure 4.9: Error signal of the PDH technique for s polarization of the injection-locked laser.

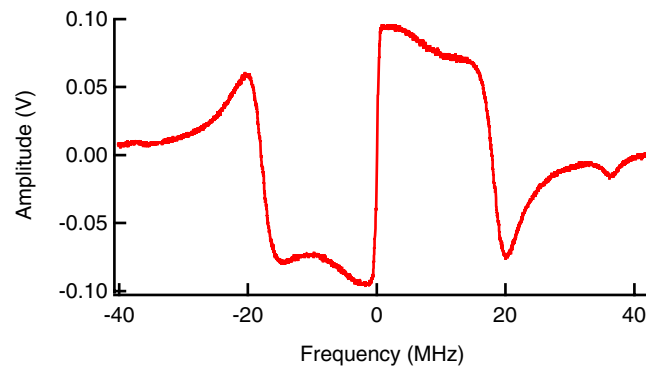


Figure 4.10: Error signal of the PDH technique for p polarization of the injection-locked laser.

4.4.3 Transmittance of the PMC

Figure 4.11 shows a spectrum of transmittance for the injection-locked laser through the PMC plotted as a function of sweeping time. There are two peaks of fundamental Gaussian modes, separated by the free spectral range of 714 MHz. The other higher-order Gaussian modes are suppressed below the noise level of the photodetector. The residual peaks correspond to the second- and fourth-order Gaussian modes, which are mainly caused by mismatching of the wavefront and the mirror curvature. Intensity of these modes are less than 1% respectively, confirming that the spatial mode of the injection-locked laser is excellent.

The separation between the transverse modes are not equal: this is due to the PZTs property, which exhibits nonlinear expansion when high voltage is applied. Taking the PZT behavior into account, the interval frequency between the transverse mode is in agreement with expected values.

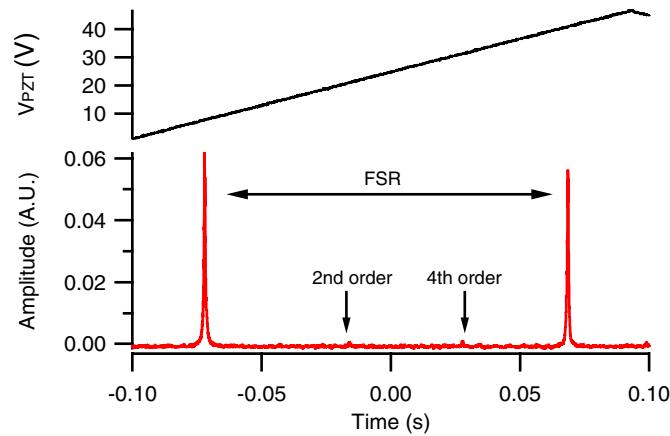


Figure 4.11: Transmittance characteristics of the PMC for p-polarized light. Upper trace is the triangle voltage applied to the PZT to sweep the PMC length.

Figure 4.12 shows a CCD image of the transmitted light of the injection-locked laser. The profile is analyzed by fitting a Gaussian function in Figure 4.13.

Figure 4.14 and Figure 4.15 show the transmittance spectra of the injection-locked laser for s and p polarization. Also shown in the graphs are fitted curves with Lorentzian functions. The linewidth for s-polarized light is 0.239 MHz and for p-polarized light is 3.21 MHz, coincident with the results of the master laser.

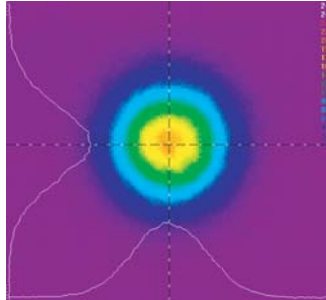


Figure 4.12: Spatial distribution of the Gaussian mode of the injection-locked laser.

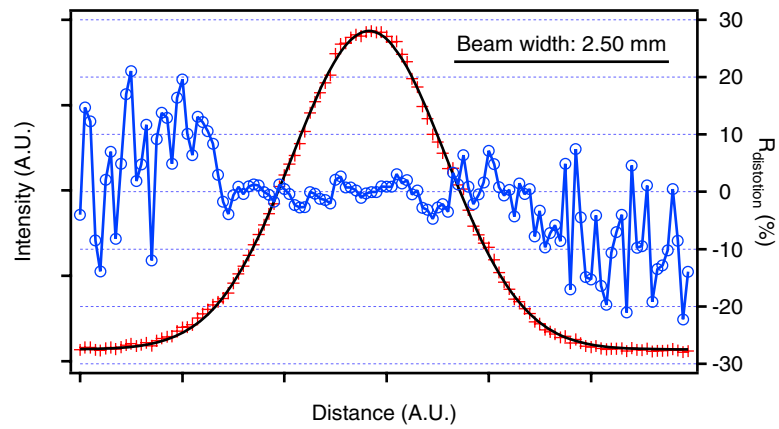


Figure 4.13: Gaussian fitting of Figure 4.12 in the vertical plane, which contains the peak of the profile.

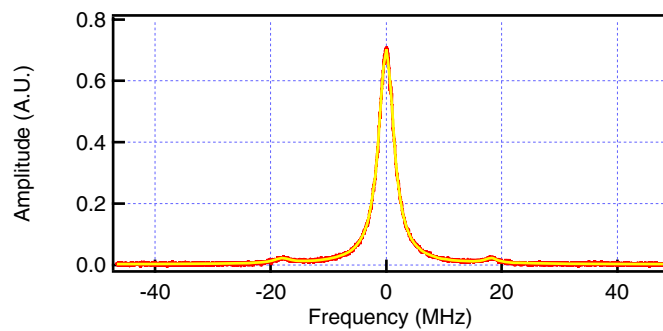


Figure 4.14: Transmitted light of the p-polarized injection-locked laser and a fitting curve.

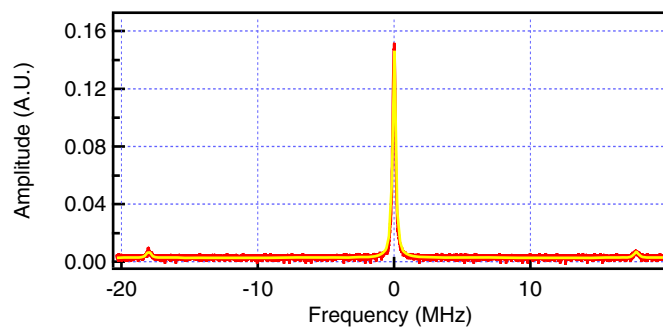


Figure 4.15: Transmitted light of the s-polarized injection-locked laser and a fitting curve.

4.4.4 Transfer function of the feedback loop

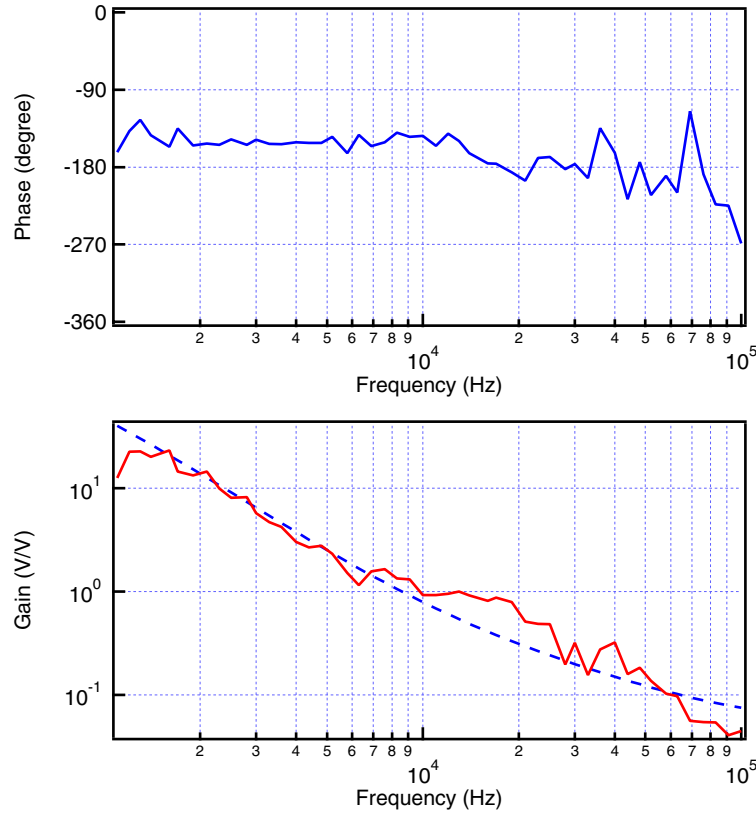


Figure 4.16: Bode diagram of the transfer function in the frequency stabilization servo. The dashed curve is the designed gain of the transfer function.

Transfer function of the feedback servo filter (for s polarization) is shown in Figure 4.16. There was no mechanical resonance due to the PZT within the measurement bandwidth. This plot is the result of the s-polarized light; the same Bode diagram (except the gain) was obtained for the p-polarized light. The UGF was approximately 7 kHz and the phase margin was about 30°.

4.4.5 Frequency stability of the injection-locked laser

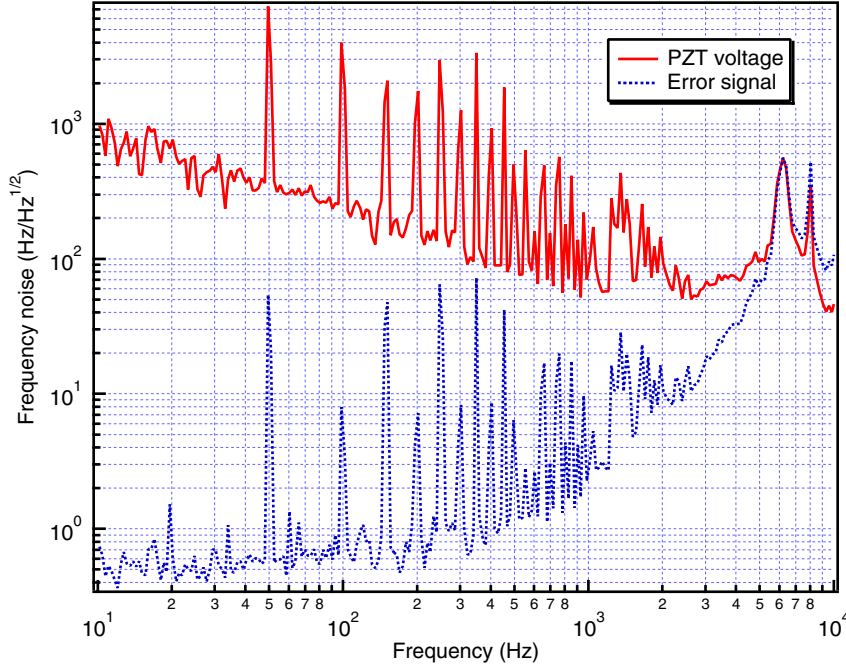


Figure 4.17: Frequency noise spectra for s-polarized light. The solid curve is the frequency noise of the injection-locked laser and the dotted curve is the stabilized frequency noise.

The frequency stability of the injection-locked laser (measured for s-polarized incident light to the PMC) is shown in Figure 4.17. The upper trace is the frequency noise of the injection-locked laser, evaluated by the voltage applied to the frequency actuator, and the lower trace is the spectrum of the stabilized frequency noise with respect to the PMC frequency stability, evaluated by the error signal. The frequency noise (upper trace) was calibrated by the PZT coefficient of the NPRO of 1 MHz/V and the gain of the PZT driver of 3. The stabilized frequency noise was calibrated by the slope coefficient of 2.46 V/MHz (calculated from the plot in Figure 4.9). The UGF in this measurement was 7 kHz.

The frequency noise of the injection-locked laser is $2 \times 10^2 \text{ Hz Hz}^{-1/2}$ at 100 Hz and the stabilized frequency noise relative the PMC reached $7 \times 10^{-1} \text{ Hz Hz}^{-1/2}$ at the same frequency. The noise floor exhibits no particular structure up to 5 kHz. The slope of the frequency noise spectrum rolls off more gently than f^{-1} .

When comparing the frequency stability (without stabilization) to the frequency fluctuation of the slave cavity (see Figure 3.26), the frequency noise was reduced by three orders of magnitude at 100 Hz. Thus, the frequency fluctuation of the slave laser was suppressed by injection locking, and the feedback to the optical cavity further stabilized the frequency of the injection-locked laser.

4.4.6 Expected frequency stability

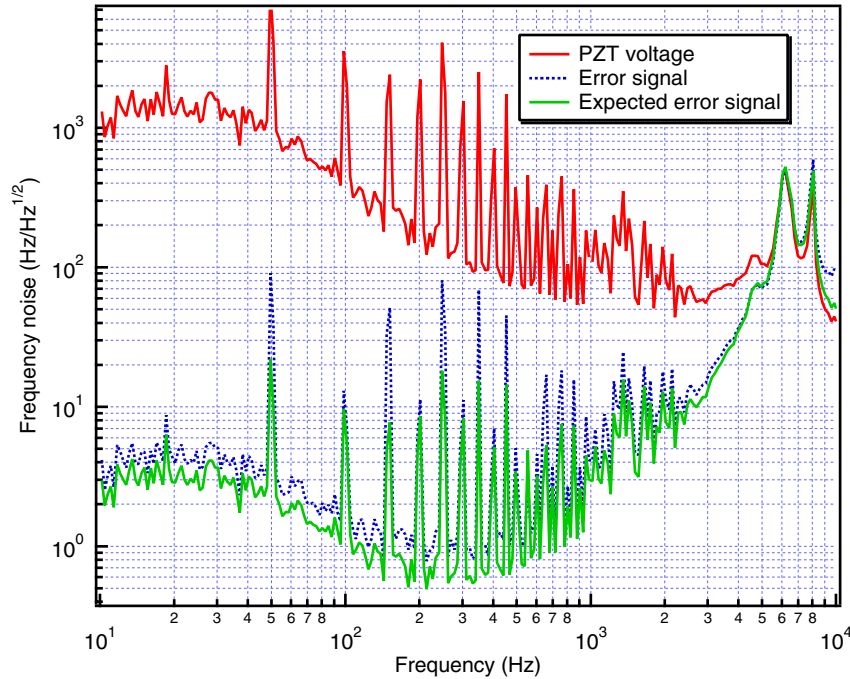


Figure 4.18: Expected stabilized frequency noise (lowest curve). The frequency stability (upper curve) and the stabilized frequency noise (dotted curve) are results for s-polarized light of the injection-locked laser. The frequency stability and the feedback servo are different from the ones shown in Figure 4.17.

The frequency noise spectrum stabilized by the feedback system ($\delta\nu_{\text{stab}}$) can be calculated by the relation

$$\delta\nu_{\text{stab}} = \frac{\delta\nu_{\text{laser}}}{|1 + T_{\text{ol}}|}, \quad (4.8)$$

where T_{ol} is the open-loop transfer function ($T_{\text{ol}} = KGD$). Figure 4.18 shows the expected stabilized frequency noise calculated by the transfer function. Also shown are the frequency noise spectra with and without stabilization, which were measured for s-polarized light. Here, the uppermost trace in Figure 4.18 corresponds to $\delta\nu_{\text{laser}}$ in Equation (4.8).

Note that the spectra shown in Figure 4.18 are different from the ones in Figure 4.17 (the servo filter at the lower frequencies is different as well). Although these spectra were measured in the same condition, we can see the frequency noise gets worse by a factor of 2.5 at 100 Hz for the measurement in Figure 4.18. Since the degradation of the frequency spectrum at the low frequencies was not always reproduced, it is attributable to some non-stationary external noise. Thus, the true frequency stability of the injection-locked laser is the one in Figure 4.17. The spectrum in Figure 4.18 includes perturbations to the PMC or the laser frequency.

The measured and the calculated spectra for the stabilized frequency noise are in good agreement to each other. Therefore, the frequency noise was suppressed as expected by the feedback servo and further suppression can be expected by improving the servo filter.

4.4.7 Frequency stability of the master laser

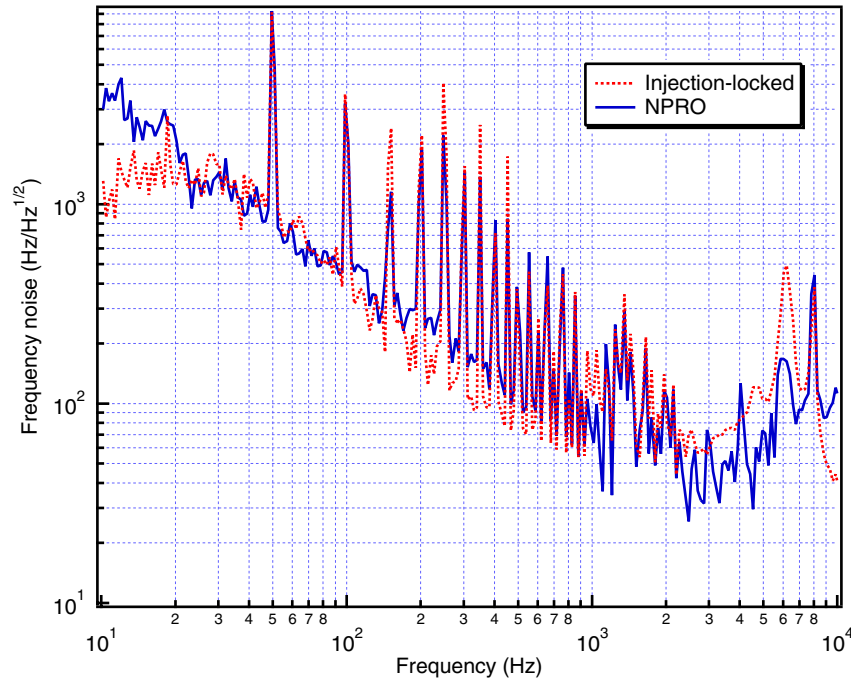


Figure 4.19: Frequency noise of the master laser and the frequency noise of the injection-locked laser. The result of the injection locking is the same as in Figure 4.18.

For reference, only the master laser was locked to the PMC: the frequency stability of the master laser is shown in Figure 4.19. The spectrum was measured for s polarization. Also the frequency stability of the injection-locked laser is shown in the graph (the same with the plot in Figure 4.18).

According to the result, the frequency stability of the injection-locked laser coincided with that of the master laser. Compared to the result in Figure 4.17, the master laser exhibited the same degradation of the frequency stability as the injection-locked laser. It is hence a common source both for the master and injection-locked laser.

The true frequency noise of the master laser should be the same as Figure 4.17; therefore, the frequency stability of the injection-locked laser is limited by the master laser, as predicted by the theoretical model of injection locking.

4.4.8 Frequency noise spectra for s and p polarization

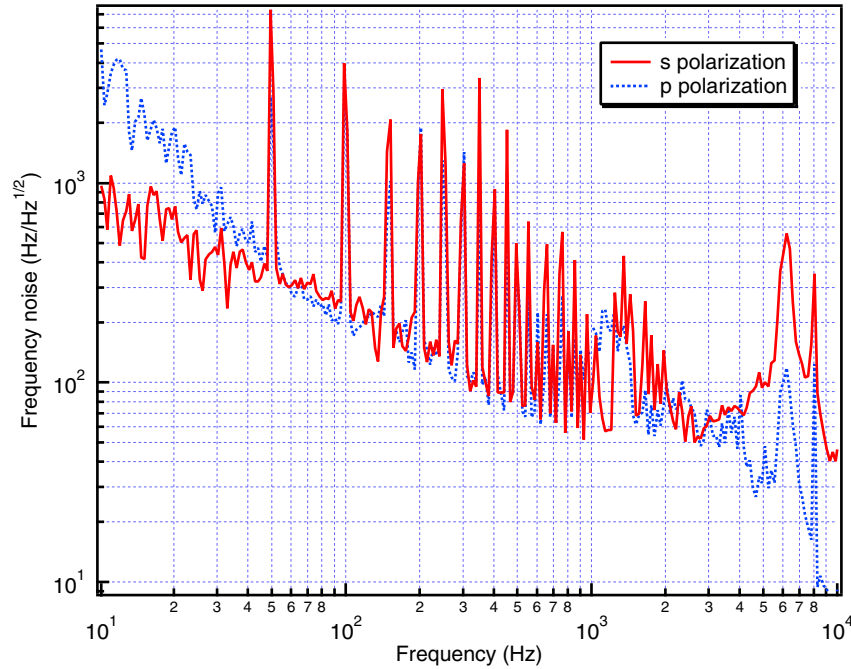


Figure 4.20: Frequency noise of the injection-locked laser for s- and p-polarized input light.

Figure 4.20 shows the frequency noise of the injection-locked laser for s- and p-polarized incident light into the PMC. The spectra for the two input polarizations matched each other; thus the measured spectra should be those for the same quantity because the spectrum was independent of the finesse, or the cavity sensitivity to the environmental perturbations.

4.5 Discussions

4.5.1 Mode cleaning effect of the PMC

According to Figure 3.17 and Figure 4.12, the spatial mode of the transmitted beam improved slightly at the center of the cross section, though not significantly.

The CCD image for the transmitted light exhibits a round beam shape compared to Figure 3.16. Though the effect is not as clear as the Willke's report, the mode cleaning for the transmitted light was achieved with the PMC.

4.5.2 Frequency stability of the injection-locked laser

The frequency noise of the injection-locked laser was $2 \times 10^2 \text{ Hz Hz}^{-1/2}$ at 100 Hz and was suppressed to $7 \times 10^{-1} \text{ Hz Hz}^{-1/2}$ at the same frequency as shown in Figure 4.17. The shot noise for the current configuration is $4 \times 10^{-4} \text{ Hz Hz}^{-1/2}$ assuming s-polarized input light of $P = 10 \text{ mW}$ and $\eta = 1$ for Equation (4.4). Since the feedback gain was 50 dB at 100 Hz, we need to increase the gain by three orders of magnitude to achieve a shot noise limited frequency stability.*

The noise level of $2 \times 10^2 \text{ Hz Hz}^{-1/2}$ is just comparable to the empirical frequency stability of NPRO, which is expressed in the form[†]

$$\delta\nu_{\text{NPRO}} \sim \frac{10^2}{(f/100 [\text{Hz}])} \left[\text{HzHz}^{-1/2} \right]. \quad (4.9)$$

Here, the prediction is based on reported experimental results^{37,38,78,107–109}. The actual frequency dependence of the NPRO can differ from the relation by a certain factor.

When comparing the measured frequency stability with the empirical prediction, we can see that the master laser completely controlled the frequency property of the injection-locked laser, since it suppressed the frequency fluctuation of the free-running slave laser to the stability level of the master laser, as shown in Figure 4.19.

Therefore, the requirement for the frequency noise of the injection-locked laser has been fulfilled. Also good controllability of the injection-locked laser has been confirmed since the relative frequency noise was suppressed by modulating the master laser frequency. Thus, the techniques currently adopted in the detectors can be applied to further frequency stabilization of the injection-locked laser.

To the best of my knowledge, this work is the first demonstration of frequency stabilization using a laser with an output power exceeding 100 W. Frequency stability investigation using a mode-analyzer-cavity was suggested by Frede⁴¹), however, the result has not been published yet.

The poor frequency stability at the lower frequencies in Figure 4.18 was caused by an unknown noise source. Although the source has not been identified, there are possible causes as follows:

First, the PZTs and the Viton attached to the spacer is one of the causes for the degradation of the cavity stability. The end mirror will be fixed to the spacer with epoxy to eliminate the possible instability by the structure.

*The frequency stability mentioned here is in absolute unit. Another more stable reference will be needed if the stability is to be evaluated.

[†]Note that there is no rigorous theoretical model to predict the frequency stability in the form of Equation (4.9).

Second, the beam undergoes a long path (more than 5 m) folded by steering mirrors before it is incident on the PMC, which should be vulnerable unexpected disturbance. It is also exposed to the air flow during the travel.

The spring stage for the seismic motion isolation should be improved in order to stabilize the PMC. Nakagawa⁷⁷⁾ reported similar frequency stabilization experiments using linear optical cavities that were suspended by pendulums. He compared the absolute frequency stabilities with and without the suspensions, which showed that the absolute stability of the stabilized laser was strongly dependent on the seismic isolation. Without any seismic isolation, the absolute frequency stability of the stabilized laser was on the order of $10^2 \text{ Hz Hz}^{-1/2}$, comparable to the typical stability of NPRO.

Another possible source might be the residual acoustic noise. The pressure in the sealed chamber was 10^1 Pa during the measurements in this work; further evacuation using an ion pump might affect the cavity stability.

For future work, the frequency stability of the injection-locked laser can be evaluated by measuring a beat note between the injection-locked output and the phase-shifted master laser, as conducted by Ottaway¹⁰⁵⁾. The output signal will show the residual phase difference between the master and injection-locked laser.

4.5.3 Possibility for application of the PMC in LCGT

Although the injection-locked laser has been fully characterized with the PMC, the stability of the PMC itself should be investigated more closely.

According to the estimation by Nagano and Moriwaki¹¹⁰⁾, the frequency stability after transmitted through the MC1 is approximately $10^0 \text{ Hz Hz}^{-1/2}$ at 1 kHz. The PMC fulfills this requirement because the upper limit of the stability is set by the frequency noise in Figure 4.17[‡]. Thus, the PMC stability is comparable to the noise level of $10^0 \text{ Hz Hz}^{-1/2}$ at worst.

Therefore, taking account of the experimental results and the requirement for the transmitted light through the MC1, both topologies of the PMC in Figure 4.2 are possible from the viewpoint of frequency stability.

However, the UGF in this experiment is limited to 7 kHz, and hence the frequency stability of the injection-locked laser or the PMC at higher frequencies can not be evaluated only by the results. Improvement of the feedback servo is required to extend the control bandwidth so that we can measure the frequency stability of the injection-locked laser and the PMC at higher frequencies.

Also, it is crucial to identify the cause for the non-stationary noise that appeared in the frequency noise spectra. If it is due to a perturbation to the PMC, it should be located in a quieter environment. Further study on the PMC performance is required.

[‡]If we assume a large fluctuation of the PMC, Equation (4.2) yields a signal of the frequency noise limited by the reference stability.

4.6 Summary

I have characterized the frequency performance of the injection-locked laser.

- Frequency stability of the injection-locked laser is limited by that of the master laser, as predicted by the theoretical model of injection locking.
- The frequency noise of the injection-locked laser has been suppressed to the level of $10^{-1} \text{ Hz Hz}^{-1/2}$ at 100 Hz, which is the first demonstration of frequency stabilization using an injection-locked laser with an output power exceeding 100 W.

Further investigation is needed for improving the frequency stabilization of the injection-locked laser. Also we need to investigate the PMC performance more closely to determine the control topology in LCGT.

Chapter 5

Conclusions

5.1 Conclusions

- The optimized linear cavity laser was expanded to the ring laser with another identical laser module and the expected laser performance was achieved. Thus, it has been proven to be feasible to construct a ring laser by expanding an optimized linear cavity laser.
- Unidirectional operation of the ring laser was achieved with the intracavity Faraday rotator. Complete suppression of the reverse wave and the gain competition was confirmed by the intensity noise. Enforcing unidirectional oscillation with an intracavity Faraday rotator is therefore suitable to characterize a bidirectional ring laser output.
- I have succeeded in generating an output power of 100 W for an excellent beam quality with injection locking.
 - Continuous wave with an output power of 100 W
 - Single-frequency oscillation
 - Spatial beam quality of diffraction limit ($M_{\text{hor}}^2 = 1.11$, $M_{\text{ver}}^2 = 1.13$)
 - Linearly polarized in the horizontal plane with the polarization ratio better than 1:35
 - Intensity stability comparable to those of the current lasers
 - Frequency stability limited by the master laser

Therefore, the injection-locked laser has fulfilled all the requirements for the first stage of the LCGT laser.

- Frequency controllability of the injection-locked laser has been confirmed, including the 100-W power level. The frequency stability of the injection-locked laser was limited by the master laser, as predicted by the theoretical model of injection locking.
- The relative frequency stability of $7 \times 10^{-1} \text{ Hz Hz}^{-1/2}$ at 100 Hz has been achieved for the 100-W, injection-locked laser. To the best of my knowledge, this is the first demonstration of frequency stabilization using an injection-locked laser with an output power of 100 W.
- The PMC performance has been proven to be sufficiently stable for the use in LCGT in terms of the frequency stability.

5.2 Future work

I will improve the injection locking system as follows:

- Install a wide dynamic-range frequency actuator in the slave cavity of the injection-locked laser to compensate for the frequency drift.
- Redesign the servo filter to achieve a higher UGF.

The frequency stabilization system will be improved as follows:

- Improve the servo filter to achieve a higher UGF and thus lower suppressed frequency noise at the error point.
- Extend the control bandwidth by using an external EOM.
- Install a damper in the two-stage spring of the PMC.
- Glue the end mirror of the PMC to the spacer to improve the frequency stability.
- Replace the PMC spacer with one made of ULE to reduce thermal expansion caused by temperature fluctuation.

I will construct a MOPA system using the injection-locked laser as a master laser.

- Achieve an output power of 150 W with a good beam quality.
- Stabilize the intensity fluctuation of the MOPA output by modulating the amplification ratio.
- Evaluate and improve the total performance of the laser with the injection locking and MOPA to fulfill all the requirements for the LCGT laser.

Appendix A

Other possible light sources for future detectors

In this work, a side-pumped Nd:YAG rod was used as the laser medium. However, there are other candidates for the laser source of LCGT. Characteristics of lasers are reviewed and possibilities of applying them to future detectors are examined in this section.

A.1 Factors to determine the laser configuration

In order to monitor small displacement with a Michelson interferometer, a laser with a short wavelength is preferable as the light source. On the other hand, light with shorter wavelengths are vulnerable to Rayleigh scattering, in which the scattered intensity is proportional to λ^{-4} . Therefore, for the purpose of a gravitational wave detector a laser with frequency from visible to infrared region are the best candidates.

In practice, decisions concerning which type of laser to use in an interferometric detector of gravitational waves depend on the following factors:

1. Laser material which is resistible to high internal power and possesses good optical quality.
2. Pumping source to generate continuous radiation with high output power.
3. A master laser at the wavelength of the light source, for either case of injection locking or MOPA (no laser should oscillate at a single frequency at 100 W without aid of these techniques).
4. Low intrinsic noise.
5. Reliability for long-term observation of gravitational waves, which will be on the order of several thousand hours continuously.
6. Compactness and efficiency.
7. Optical components of high quality for the interferometer, available at the wavelength of the selected laser material.

From a practical viewpoint, solid-state lasers, fiber lasers and diode lasers are the most promising light sources for gravitational wave detectors, and thus the topics concentrated in the following sections.

Material	λ_{LO} (nm)	λ_P (nm)	η_Q (%)	κ (W/cm K)	σ (cm ²)	τ (μ s)
Nd:YAG	1064	808	76	0.14	2.8×10^{-19}	230
Nd:YVO ₄	1064	808	76	0.05	15.6	90
Nd:Glass	~ 1060	~ 800	75	0.01	0.4	315
Yb:YAG	1030	940	91	0.14	0.21	850

Table A.1: Properties of laser materials. λ_{LO} is the wavelength of laser oscillation, λ_P is the wavelength of pumping radiation, η_Q is the quantum efficiency defined as the ratio of the laser oscillation wavelength to the pumping wavelength, κ is the thermal conductivity, σ is the stimulated emission cross section and τ is the fluorescence lifetime.

A.2 Laser materials

Table A.1 summarizes the properties of typical solid-state laser materials used for DPSSLs, fiber lasers and fiber amplifiers at $1 \mu\text{m}^{111,112}$.

In designing a laser system, one should take account of stimulated emission cross section (σ) and fluorescence lifetime (τ), which determine the property of a laser. A larger cross section is preferable to construct a compact and efficient laser or amplifier since the small signal gain g_0 is proportional to σ

$$g_0 = \sigma \Delta N, \quad (\text{A.1})$$

where ΔN is inverted population in a laser medium.

The saturation intensity of a four energy level laser is expressed in the form

$$I_s = \frac{h\nu}{\sigma\tau}, \quad (\text{A.2})$$

which shows that the saturation intensity is inversely proportional to $\sigma \times \tau$; a larger value of the cross product is thus desirable because saturated amplification can be achieved at relatively lower intensity in a MOPA system.*

Good thermal conductivity is also an important factor for a high-power laser due to the limit thermally-induced effects often have on the output power of a laser.

A.2.1 Nd-doped materials

Nd³⁺-doped materials have a good spectroscopic characteristics of a high absorption peak around 800 nm and can be excited efficiently by diode lasers at the frequency band.

Nd:YAG laser has an optically isotropic host material with high thermal conductivity and high thermal fracture limit; and thus it is widely accepted.

Nd:YVO₄ has a large cross section of stimulated emission and is suitable for a disc laser due to the high absorption coefficient at the pumping wavelength^{113–115}). The host material is a uniaxial crystal with the polarization of laser output determined by the natural birefringence. Nd:YVO₄ has, however, some drawbacks: the short fluorescence lifetime, which reduces the cross product of σ and τ , and low thermal conductivity. The VIRGO project is using a 20-W Nd:YVO₄ laser as the light source.

*However, a laser medium with larger σ has, in general, lower τ and it is not easy to increase both of the parameters independently.

Although thermal conductivity is less than Nd:YAG by an order of magnitude, Nd:Glass lasers have good properties of high concentration of the dopant, isotropic structure and flexibility to fabricate in a large size, suitable for application of laser fusion rather than precision metrology.

A.2.2 Yb-doped materials

Yb³⁺-doped materials have a large cross section of emission and thus a large absorption coefficient. This property enables laser oscillation with a thin crystal such as disc lasers.

Another merit to using a Yb-doped material involves the high quantum efficiency of as high as 91%. Due to the high quantum efficiency, thermal load in the Yb:YAG crystal can be reduced by a factor of 3 compared with Nd:YAG¹¹⁶⁾, which is a preferable characteristic when building a high-power laser.

In scaling the output power, the wide fluorescence linewidth of 8.5 nm (for Yb:YAG) is an obstacle to achieve single-frequency oscillation. The difficulty can be circumvented by using, for instance, an etalon in a disc laser or a distributed grating in a fiber laser. Also injection locking will, in principle, be able to suppress the other frequency modes across the wide spectral band.

A.2.3 Ceramic materials

Recently, the excellent optical quality of ceramic lasers has been improved. The output power from a ceramic Nd:YAG laser was proven to be comparable to the power from crystal Nd:YAG lasers^{112, 117, 118)}. The advantages of ceramic materials are: (1) easy and fast to fabricate, (2) flexible in designing the shape, (3) possible to highly concentrate a dopant material, (4) scalability of the material size (two-dimensional), (5) less expensive compared to crystalline materials, which are desirable for the purposes of industrial processing.

However, since the optical quality is just compatible to crystals', the advantages do not raise strong motivations to use ceramic materials for the side-pumped rod system. A possible application of ceramic materials would be mode controlling laser oscillation by making an internal gain distribution, which is difficult to fabricate with conventional method of crystal growth.

A.2.4 Diode lasers

Semiconductor lasers are now very reliable source of strong radiation and could be used for our purpose. High-power diode lasers are usually packaged in an array to increase the output power as a whole; the spatial distribution is broadened rather than diffraction-limited. Also, the frequency of the laser diodes are usually multi-mode. Little research has been conducted to operate it in a single longitudinal mode with high-power semiconductor lasers. Thus, diode lasers are not yet applicable to a gravitational wave detector.

However, there is a possibility that a diode laser itself can be used as a light source in gravitational wave detection, not as a pumping source, if issues of the output power and the frequency are solved in the future.

A.3 Laser configurations

A.3.1 Rod lasers

A rod medium is less expensive, easy to grow, polish and coat, simple and easy to obtain. Due to the axial-symmetric shape of the laser medium, the circular spatial distribution of the output intensity can be easily achieved.

A side-pumped rod laser system has the advantage of uniform pumping and scalability of the output power. On the other hand, there is no structure to avoid the thermal birefringence and thermal lensing and thus compensation for thermally induced effects is indispensable for a rod laser.

High efficiency and a gain-guided aperture are of great advantage to an end-pumped rod laser system due to the collinear geometry of the pump radiation to the laser oscillation. However, the non-uniform absorption along the optical axis makes it difficult to scale the output power in the end-pumped configuration. In recent years, thermal distortion in the end-pumped configuration is reduced by using a rod with diffusion-bonded end-caps, which contain no active material doped^{41,119}).

A.3.2 Slab lasers

Laser materials in slab shape are widely used in constructing high-power lasers or high-power MOPA systems in side-pumped¹²⁰⁻¹²²), edge-pumped^{123,124}) and end-pumped geometries¹²⁵).

Thermal effects in slab lasers are averaged and reduced by folding the optical path in the medium. However, the averaging effect in turn causes complex distribution of thermal load at higher pumping power. Since the complex thermal distortion is imposed on during the zigzag path in the medium, the effect can hardly be compensated for.

A.3.3 Disc lasers

A disc-shaped laser medium is used as an active mirror^{113,115}). Due to the geometry, the thermal load can be extracted from the back surface of the laser medium and the temperature can be stabilized by conduction cooling.

A 50-W, diffraction-limited, single-frequency laser in this configuration is commercially available¹²⁶). However, the active mirror configuration limits scalability of power with good beam quality. Also single frequency operation with an intracavity etalon decreases the output power significantly.

A.3.4 Fiber system

In a fiber laser, or a fiber MOPA system, there is no thermal distortions because of the extremely high aspect ratio. The main limitation imposed on a high-power fiber system is due to the nonlinear effect of stimulated Brillouin scattering (SBS) resulting from interaction with phonon and the optical power confined in the core dimension. Since the amplitude of nonlinear scattering is proportional to the internal power density, the highest output power available from the fiber system is dependent on the fiber core diameter; the larger the diameter is, the more the available power will be. On the other hand, the larger diameter allows propagation of higher-order spatial modes in the fiber. Therefore, dimension of the fiber for building a high-power laser system should be carefully chosen⁷⁰).

Fiber laser is a promising light source for future detectors. A fiber laser system has been investigated for the LCGT laser by a research group at the University of Electro-Communications.

A.4 Discussion

When one should design a laser system, there is no absolute criterion to determine the configuration. Advantages and drawbacks of a laser geometry are dependent on the way he or she thinks what is the best to achieve the goal.

In this work, the following criteria are the primary factors to choose the laser geometry:

- How much effort to achieve a 100 W, single-frequency, TEM₀₀ oscillation.
- Simplicity for the system so that it can be maintained easily.

I consider that there is no other choice but injection locking or MOPA to achieve single-frequency oscillation at 100 W, and thus I take no account of gratings and etalons. Inherent mode selectivity is desirable for a laser configuration, but intracavity apertures can be used if needed.

As mentioned previously, using Yb:YAG as a laser medium can reduce thermal load significantly compared to Nd:YAG. Since thermal lensing determines the maximum pumping power for the current design of the slave laser, the operation pumping power might be shifted even to a higher region by replacing the Nd:YAG rods with Yb:YAG rods. The problem which prevents us from investigating Yb:YAG as the promising laser medium for gravitational wave detectors is that the wavelengths of laser oscillation and optical pumping are different from those of Nd:YAG, which leads to absence of a master laser for injection locking or an efficient pumping source at the wavelengths. A Yb:YAG fiber laser could be used as the master laser for injection locking or MOPA. If these difficulties are circumvented, a Yb:YAG laser would be suitable for a future detector which is designed specifically for the wavelength of 1030 nm.

Figure A.1 shows a comparison between laser configurations: note that this is not a general discussion to compare laser geometries, but it focuses on high-power, single-frequency lasers with good beam quality suitable for the use in gravitational wave detectors. Therefore, the charts are based on the current status of high-power laser developments for each geometry as well as the inherent advantages.[†]

According to the charts, the end-pumped rod, side-pumped slab and disc lasers are apparently not suitable for a high-power laser system. Thermal distortion of the end-pumped rod laser can be circumvented by using an end-capped rod, which depends on, however, the quality of the bonding and thus not such a simple scheme to construct a high-power laser.

Intensity noise at high output power is determined by the pumping fluctuation in solid-state lasers. Since diode lasers are used to pump laser media in most cases, there is no significant difference in inherent intensity noise among the laser configurations.

A.5 Conclusion

Side-pumped Nd:YAG rod laser was the best choice in 2001, when the development of the LCGT laser started. However, progress in high-power lasers since then has brought possibilities of applying other lasers to future detectors. The most promising candidates are diode lasers, Yd:YAG lasers and fiber lasers. It is highly possible to use one of these lasers as the light source of next-generation gravitational wave detectors if all technical problems are solved in the future.

[†]For instance, a side-pumped rod system does not generally possess spatial mode selectivity. However, since single transverse mode oscillation was achieved in this work, SBQ of the side-pumped rod laser scores high.

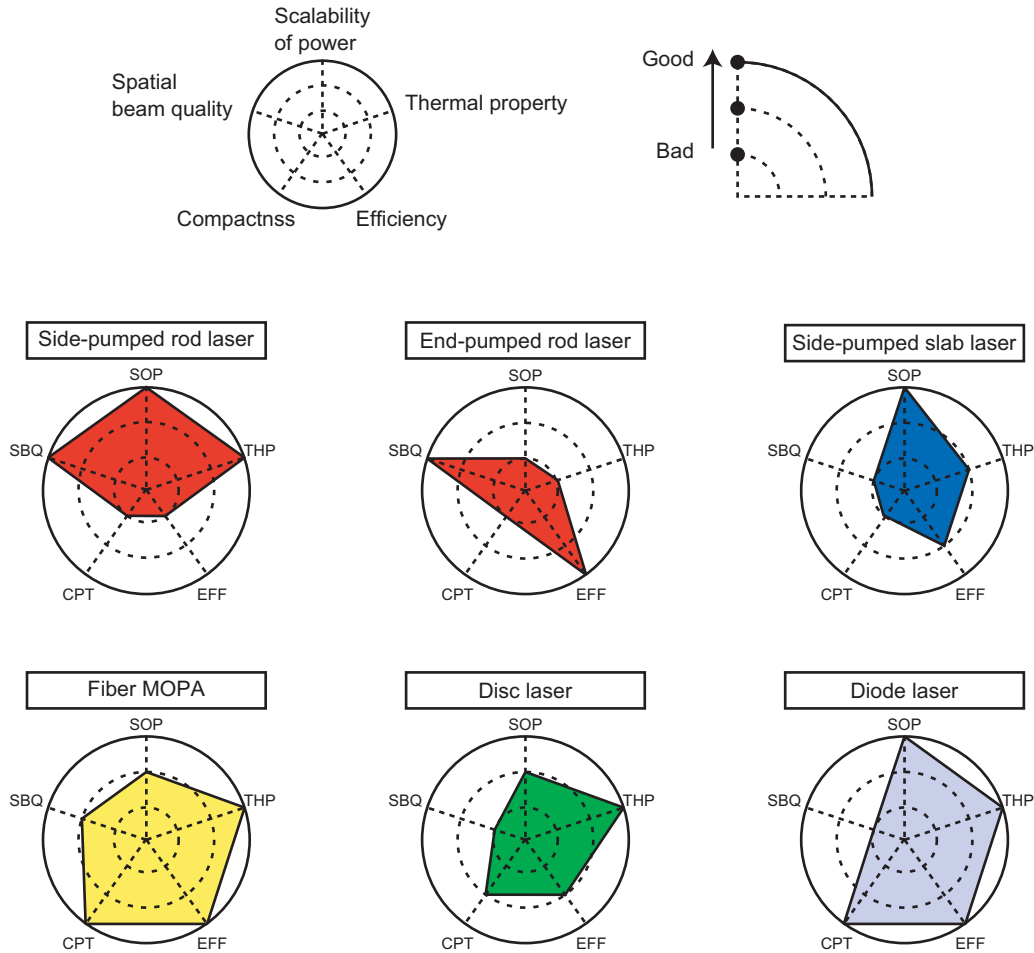


Figure A.1: Comparison between geometry-dependent performances at an output power of 100 W. The criteria to score each term are as follows: Scalability of power (SOC): capability of scaling the output power to over 100 W by adequate techniques and designs, which is not limited by the laser structure itself; Spatial beam quality (SBQ): inherent mode selectivity for the configuration; Thermal property (THP): capability of compensating for thermally induced distortions; Compactness (CPT): compactness of the device on the optical table to perform experiments; Efficiency (EFF): total efficiency of the system. Since good performance was achieved in this work, the side-pumped rod laser scores high.

Appendix B

Formulas of noise in LCGT

B.1 Seismic noise

The seismic noise at the LCGT site was measured to be as follows:

$$G_{\text{seismic}} = \frac{10^{-9}}{f^2} \left[\text{m Hz}^{-1/2} \right], \quad (\text{B.1})$$

which is lower by two orders of magnitude compared to the TAMA site. A seismic attenuation system and a SPI will reduce the seismic noise; the expected isolation ratio is

$$H_{\text{isolation}} = \frac{10^{-3}}{f^{10}}. \quad (\text{B.2})$$

Therefore, the seismic noise of LCGT is expected to be

$$h_{\text{seismic}} = \frac{2}{L} H_{\text{isolation}} G_{\text{seismic}} \quad (\text{B.3})$$

$$= 2 \times 10^{-12} \frac{1}{L} \frac{1}{f^{12}} \left[\text{Hz}^{-1/2} \right], \quad (\text{B.4})$$

where $L = 3$ km is the arm length of LCGT.

B.2 Thermal noise

Since thermally excited fluctuation of optical components of an interferometer can simulate a gravitational wave signal, the fluctuation should be reduced below the expected signal level of a target gravitational wave.

There are two sources of thermal noise: one is thermal noise of suspensions, the other is thermal noise of mirrors.

The thermal noise of the suspension can be calculated by

$$h_{\text{sus}} = \frac{2}{L} \sqrt{\frac{4k_{\text{B}} T_{\text{P}} (2\pi f_{\text{pen}})^2}{m Q_{\text{pen}} \omega^5}} \left[\text{Hz}^{-1/2} \right], \quad (\text{B.5})$$

where k_B is Boltzmann's constant, T_p is the temperature of the suspension system, f_{pen} is the resonant frequency of the suspension, m is the mass of the mirror and Q_{pen} is the Q value. The Q of the suspension is

$$Q_{\text{pen}} = \left(\frac{n \sqrt{T E_{\text{wire}} I}}{2mg l_{\text{sus}}} \phi_{\text{wire}} \right)^{-1} \quad (\text{B.6})$$

where n is the number of the suspending wire, E_{wire} , I_{sus} , ϕ_{wire} are Young modulus of the wire, length of the suspension and the loss angle of the wire, respectively. T is the tension of each wire:

$$T = \frac{mg}{n}, \quad (\text{B.7})$$

and I is the moment of the wire with a diameter of d_{wire} :

$$I = \frac{\pi d_{\text{wire}}^4}{64}. \quad (\text{B.8})$$

The thermal noise of a mirror of an isotropic medium is caused by structural damping ($h_{\text{mirror(structure)}}$) and thermoelastic damping ($h_{\text{mirror(thermo)}}$) of the substrate, and mechanical loss of the mirror coating ($h_{\text{mirror(coating)}}$). Each noise can be evaluated according to the formula:

$$h_{\text{mirror(structure)}} = \frac{2}{L} \sqrt{\frac{4k_B T_m (1 - \sigma^2)}{\sqrt{\pi} E_0 \omega_0 Q_{\text{mirror}} \omega}} \left[\text{Hz}^{-1/2} \right], \quad (\text{B.9})$$

$$h_{\text{mirror(thermo)}} = \frac{2}{L} \sqrt{\frac{2}{\sqrt{\pi}} \alpha^2 (1 + \sigma)^2 k_B T_m^2 \frac{1}{(\kappa \rho C)^{1/2}} \frac{1}{\omega^{1/2}}} \left[\text{Hz}^{-1/2} \right], \quad (\text{B.10})$$

$$h_{\text{mirror(coating)}} = \frac{2}{L} \sqrt{\frac{8k_B T_m (1 + \sigma)(1 - 2\sigma) d_{\text{coating}} \phi_{\text{coating}}}{\pi \omega_0^2 E_0 \omega}} \left[\text{Hz}^{-1/2} \right], \quad (\text{B.11})$$

where L is the arm length, T_m is the temperature, σ is the Poisson ratio, E_0 is the Young modulus, ω_0 is the radius of the beam size, Q_{mirror} is the Q factor, α is the expansion coefficient, κ is the thermal conductivity, ρ is the density, C is the specific heat (these parameters are all mirror's), ϕ_{coating} is the loss angle of the coating and d_{coating} is the thickness of the coating. The total thermal noise h_{thermo} is

$$h_{\text{thermo}} = \sqrt{h_{\text{sus}}^2 + h_{\text{mirror(structure)}}^2 + h_{\text{mirror(thermo)}}^2 + h_{\text{mirror(coating)}}^2}. \quad (\text{B.12})$$

B.3 Shot noise

For the configuration of LCGT, the shot noise can be calculated by the formula:

$$h_{\text{shot}} = \sqrt{\frac{\hbar \lambda f_{\text{cut}}}{2LP_{\text{cavity}}} \left(1 + \frac{f^2}{f_{\text{cut}}^2} \right)} \left[\text{Hz}^{-1/2} \right], \quad (\text{B.13})$$

where \hbar is Planck's constant, λ is the wavelength of the light, f_{cut} is the bandwidth of the interferometer, L is the arm length and P_{cavity} is the total circulating power in the arm cavity. f_{cut} and P_{cavity} are

connected to the interferometer parameter by

$$f_{\text{cut}} = G_{\text{SR}} f_{\text{cavity}}, \quad (\text{B.14})$$

$$P_{\text{cavity}} = \frac{2\mathcal{F}}{\pi} G_{\text{PR}} P_0, \quad (\text{B.15})$$

where G_{PR} is the power recycling gain, \mathcal{F} is the finesse of the arm cavity, G_{SR} is the signal recycling gain and P_0 is the incident power. f_{cavity} is the cut off frequency of the simple Michelson interferometer of

$$f_{\text{cavity}} = \frac{c}{4L\mathcal{F}}. \quad (\text{B.16})$$

B.4 Radiation pressure noise

The radiation pressure of LCGT can be calculated by

$$h_{\text{radiation}} = \frac{1}{L} \frac{4}{m\omega^2} \sqrt{\frac{hP_{\text{cavity}}}{\lambda L f_{\text{cut}}}} \frac{1}{\sqrt{1 + (f/f_{\text{cut}})^2}} \quad [\text{Hz}^{-1/2}], \quad (\text{B.17})$$

where m is the mass of the mirror.

According to the uncertainty principle, the shot noise and the radiation pressure noise cannot be independently reduced, but there is limitation imposed on the geometric mean of these noises, that is

$$h_{\text{SQL}} = \sqrt{2 h_{\text{shot}} h_{\text{radiation}}} \quad (\text{B.18})$$

$$= \frac{1}{L\omega} \sqrt{\frac{8\hbar}{m}}. \quad (\text{B.19})$$

Here, h_{SQL} is called the standard quantum limit (SQL) of the interferometer, which gives the theoretical limit of the sensitivity. The SQL cannot be reduced unless the mass of the mirror is increased or the arm length is extended. Although the amplitude of the SQL is independent of the laser power, the crossover frequency, at which the dominant noise is taken over by the other, is determined by the laser power and the power recycling gain. In LCGT, this crossover frequency is tuned around 100 Hz, and the shot noise dominates in the higher frequency region, on the other hand the radiation pressure noise dominates in the lower frequency region.

Acknowledgement

It was fortunate for me to join the project to construct a high-power laser system at the very stage when the project started. Since then I have struggled with many timeconsuming experiments, helped by many people. I would like to thank the people involved in this work.

First of all, I would like to thank my supervisor, Prof. Mio. He allowed most of the experiments I wished to do and gave me a lot of opportunities to experience state-of-the-art experiments over the world. I have found the studies on lasers pretty exciting in his laboratory. Also, I am grateful to the people in his laboratory.

The staff at TAMA helped me the work and gave me a lot of useful advice. I learned a lot through experiments with Dr. Arai, Dr. Nagano and Dr. Musha.

I picked up my skills of laser experiments at the University of Adelaide. I would like to express my gratitude to Prof. Munch, Dr. Veitch, Dr. Mudge and Mr. Hosken.

The laser modules used in this work was developed by the Mitsubishi laser group, Dr. Yasui, Dr. Nishimae, Dr. Konno and Mr. Katsura. I am grateful to their support.

I would like to thank Dr. Frede for his letting me look around the institute and kindly answering my questions in many situations.

I would like to thank Mr. Forgan to read and correct my English in this thesis, even when he is busy in preparing for the GRE examination.

Finally, I would like to say thank you to my wife Yoko and my family. Without their support, the results wouldn't be as it is.

Bibliography

- [1] T. H. Maiman. Stimulated optical radiation in ruby. *Nature*, Vol. 187, pp. 493–494, 1960.
- [2] Bernard F. Schutz. *A first course in general relativity*. Cambridge University Press, 1985.
- [3] Takashi Nakamura, Norikatsu Mio, and Masatake Ohashi, editors. *Detection of gravitational waves*. Kyoto University Academy Press, 1998. (in Japanese).
- [4] R. A. Hulse and J. H. Taylor. Discovery of a pulsar in a binary-system. *Astrophys. J.*, Vol. 195, No. 2, pp. L51–L53, 1975.
- [5] J. H. Taylor and J. M. Weisberg. Further experimental tests of relativistic gravity using the binary pulsar PSR 1913+16. *Astrophys. J.*, Vol. 345, No. 1, pp. 434–450, 1989.
- [6] Viviana Fafone. Resonant-mass detectors: status and perspectives. *Class. Quantum Grav.*, Vol. 21, pp. S377–S383, 2004.
- [7] T. Uchiyama *et al.* Present status of large-scale cryogenic gravitational wave telescope. *Class. Quantum Grav.*, Vol. 21, pp. S1161–S1172, 2004.
- [8] Masaki Ando and the TAMA collaboration. Current status of the TAMA300 gravitational-wave detector. *Class. Quantum Grav.*, Vol. 22, pp. S881–S889, 2005.
- [9] M. Ando *et al.* Observation results by the TAMA300 detector on gravitational wave bursts from stellar-core collapses. *Phys. Rev. D*, Vol. 71, No. 8, p. 082002, 2005.
- [10] Daniel Sigg. Status of the LIGO detectors, 2005. Talk at the 6th Edoald Amaldi conference on gravitational waves, Okinawa, Japan.
- [11] F. Acernese *et al.* Status of Virgo. *Class. Quantum Grav.*, Vol. 22, pp. S869–S880, 2005.
- [12] Stefano Braccini. The status of VIRGO, 2005. Talk at the 6th Edoald Amaldi conference on gravitational waves, Okinawa, Japan.
- [13] M. Hewitson (for the LIGO Scientific Collaboration). Preparing GEO 600 for gravitational wave astronomy – a status report. *Class. Quantum Grav.*, Vol. 22, pp. S891–S900, 2005.
- [14] Harald Lück. Status of the GEO 600 detector, 2005. Talk at the 6th Edoald Amaldi conference on gravitational waves, Okinawa, Japan.
- [15] K. Kuroda *et al.* Current status of large-scale cryogenic gravitational wave telescope. *Class. Quantum Grav.*, Vol. 20, pp. S871–S884, 2003.

- [16] LCGT design document (version 1.0), 2003.
- [17] Joseph A. Giaime. The advanced LIGO detector, 2005. Talk at the 6th Edoald Amaldi conference on gravitational waves, Okinawa, Japan.
- [18] James Ira Thorpe, Rachel Jean Cruz, Shannon Reynier Sankar, Guido Mueller, and Paul McNamara. First step toward a benchtop model of the Laser Interferometer Space Antenna. *Opt. Lett.*, Vol. 29, No. 24, pp. 2843–2945, 2004.
- [19] Gerhard Heinzl. The LISA technology package LTP, 2005. Talk at the 6th Edoald Amaldi conference on gravitational waves, Okinawa, Japan.
- [20] Seiji Kawamura. The Japanese space gravitational wave antenna - DECIGO, 2005. Talk at the 6th Edoald Amaldi conference on gravitational waves, Okinawa, Japan.
- [21] Presentation transparency at 2005 LCGT Technical Advisory Committee, available at <http://www.icrr.u-tokyo.ac.jp/gr/plans.html>.
- [22] S. Miyoki *et al.* Status of the CLIO project. *Class. Quantum Grav.*, Vol. 21, pp. S1173–S1182, 2004.
- [23] The VIRGO Collaboration (presented by Raffaele Flaminio). Interferometer signal detection system for the VIRGO experiment. *Class. Quantum Grav.*, Vol. 19, pp. 1857–1863, 2002.
- [24] Koji Arai. *Robust extraction of control signals for power-recycled interferometric gravitational-wave detectors*. Ph.D. dissertation, University of Tokyo, 2001.
- [25] J. Mizuno, K. A. Strain, P. G. Nelson, J. M. Chen, R. Schilling, A. Rüdiger, W. Winkler, and K. Danzmann. Resonant sideband extraction: a new configuration for interferometric gravitational wave detectors. *Phys. Lett. A*, Vol. 175, No. 5, pp. 273–276, 1993.
- [26] Osamu Miyakawa. *Development of a Variable-Bandwidth Laser Interferometer Gravitational Wave Detector*. Ph.D. dissertation, University of Tokyo, 2001.
- [27] Kentaro Somiya, Peter Byersdorf, Koji Arai, Shuichi Sato, Seiji Kawamura, Osamu Miyakawa, Fumiko Kawazoe, Shihori Sakata, Aya Sekido, and Norikatsu Mio. Development of a frequency-detuned interferometer as a prototype experiment for next-generation gravitational-wave detectors. *Appl. Opt.*, Vol. 44, No. 16, pp. 3179–3191, 2005.
- [28] Kentaro Somiya. *Investigation of radiation pressure effect in a frequency-detuned interferometer and development of the readout scheme for a gravitational-wave detector*. Ph.D. dissertation, University of Tokyo, 2004.
- [29] Y. Aso, M. Ando, K. Kawabe, S. Otsuka, and K. Tsubono. Stabilization of a Fabry-Perot interferometer using a suspension-point interferometer. *Phys. Lett. A*, Vol. 327, pp. 1–8, 2004.
- [30] Kazuhiro Yamamoto. The goal sensitivity of LCGT ver3.1. LCGT internal document, 2002.
- [31] B. Willke, N. Uehara, E. K. Gustafson, R. L. Byer, P. J. King, S. U. Seel, and Jr. R. L. Savage. Spatial and temporal filtering of a 10-W Nd:YAG laser with a Fabry-Perot ring-cavity premode cleaner. *Opt. Lett.*, Vol. 23, No. 21, pp. 1704–1706, 1998.

- [32] F. Nocera. LIGO laser intensity noise suppression. *Class. Quantum Grav.*, Vol. 21, pp. S481–S485, 2004.
- [33] M. W. Sasnet and T. F. Johnson, Jr. Beam characterization and measurement of propagation attributes. *SPIE Vol.1414 Laser Beam Diagnostics*, pp. 21–32, 1991.
- [34] W. Koechner. *Solid-State Laser Engineering*. Springer, fifth edition, 1999.
- [35] Amnon Yariv. *Optical Electronics*. Saunders College Publishing, fourth edition, 1991.
- [36] Seiji Kawamura, Alex Abramovici, and Michael E. Zucker. Improved multistage wide band laser frequency stabilization. *Rev. Sci. Instrum.*, Vol. 68, No. 1, pp. 223–229, 1997.
- [37] Shigeo Nagano *et al.* Development of a light source with an injection-locked Nd:YAG laser and a ring-mode cleaner for the TAMA 300 gravitational-wave detector. *Rev. Sci. Instrum.*, Vol. 73, No. 5, pp. 2136–2142, 2002.
- [38] Shigeo Nagano *et al.* Development of a multistage laser frequency stabilization for an interferometric gravitational-wave detector. *Rev. Sci. Instrum.*, Vol. 74, No. 9, pp. 4177–4183, 2003.
- [39] A. E. Siegman. *LASERS*. University Science Books, 1986.
- [40] Amnon Yariv. *Quantum Electronics*. Wiley, third edition, 1988.
- [41] Maik Frede, Ralf Wilhelm, Dietmar Kracht, Carsten Fallnich, Frank Seifert, and Benno Willke. 195 W injection-locked single-frequency laser system. In *Conference on Lasers and Electro-Optics/Quantum Electronics and Laser Science and Photonic Applications, Systems and Technologies 2005*. Optical Society of America, Washington, DC, 2005. CMA1.
- [42] Craig A. Denman, Paul D. Hillman, Gerald T. Moore, John M. Telle, and Joseph E. Preston and Jack D. Drummond and Robert Q. Fugate. 50-W CW single-frequency 589-nm FASOR. In *Advanced Solid State Photonics 2005*. Optical Society of America, Washington, DC, 2005. PD5-1.
- [43] David Shoemaker, Alain Brillet, C. Nary Man, Olivier Crégut, and Graham Kerr. Frequency fluctuations of a diode-pumped Nd:YAG ring laser. *Opt. Lett.*, Vol. 14, No. 12, pp. 993–995, February 1989.
- [44] R. W. P. Drever, J. L. Hall, F. V. Kowalski, J. Hough, G. M. Ford, A. J. Munley, and H. Ward. Laser phase and frequency stabilization using an optical resonator. *Appl. Phys. B*, Vol. 31, pp. 97–105, 1983.
- [45] K. Nakagawa, A. S. Shelkovich, T. Katsuda, and M. Ohtsu. Fast frequency stabilization of a diode-pumped monolithic Nd:YAG laser with an extra-cavity electro-optic modulator. *Opt. Commun.*, Vol. 109, pp. 446–450, 1994.
- [46] K. Nakagawa, A. S. Shelkovich, T. Katsuda, and M. Ohtsu. Absolute frequency stability of a diode-laser-pumped Nd:YAG laser stabilized to a high-finesse optical cavity. *Appl. Opt.*, Vol. 33, No. 27, pp. 6383–6386, 1994.

- [47] R. S. Abbott and P. J. King. Diode-pumped Nd:YAG laser intensity noise suppression using a current shunt. *Rev. Sci. Instrum.*, Vol. 72, No. 2, pp. 1346–1349, 2001.
- [48] Jameson Rollins, David Ottaway, Michael Zucker, Rainer Weiss, and Richard Abbott. Solid-state laser intensity stabilization at the 10^{-8} level. *Opt. Lett.*, Vol. 29, No. 16, pp. 1537–1539, 2004.
- [49] S. T. Yang, Y. Imai, M. Oka, N. Eguchi, and S. Kubota. Frequency-stabilized, 10-W continuous-wave, laser-diode end-pumped, injection-locked Nd:YAG laser. *Opt. Lett.*, Vol. 21, No. 20, pp. 1676–1678, 1996.
- [50] Shigeo Nagano. *Study of a Frequency and Intensity Stabilization System with a High-power Laser for the TAMA 300 Gravitational-wave detector*. Ph.D. dissertation, University of Tokyo, 1999.
- [51] D. Mudge, M. Ostermeyer, P. J. Veitch, J. Munch, B. Middlemiss, D. J. Ottaway, and M. W. Hamilton. Power scalable TEM₀₀ cw Nd:YAG laser with thermal lens compensation. *IEEE J. Sel. Top. Quantum Electron.*, Vol. 6, No. 4, pp. 643–649, 2000.
- [52] D Mudge, M Ostermeyer, D J Ottaway, P J Veitch, J Munch, and M W Hamilton. High-power Nd:YAG lasers using stable-unstable resonators. *Class. Quantum Grav.*, Vol. 19, pp. 1783–1792, 2002.
- [53] David J. Hosken, Damien Mudge, Christopher Hollitt, Kohei Takeno, Peter J. Veitch, Murray W. Hamilton, and Jesper Munch. Development of power scalable lasers for gravitational wave interferometry. *Prog. Theor. Phys. Suppl.*, No. 151, pp. 216–220, 2003.
- [54] David Hosken. 10 w nd:yag laser for tama 300, 2005. Talk at the 6th Edoald Amaldi conference on gravitational waves, Okinawa, Japan.
- [55] R. L. Savage, Jr., P. J. King, and S. U. Seel. A highly-stabilized 10-Watt Nd:YAG laser for the laser interferometer gravitational-wave observatory (LIGO), 1998. LIGO-P980002-00-D.
- [56] I. Zawischa, M. Brendel, K. Danzmann, C. Fallnich, M. Heurs, S. Nagano, V. Quetschke, H. Welling, and B. Willke. The GEO 600 laser system. *Class. Quantum Grav.*, Vol. 19, pp. 1775–1781, 2002.
- [57] B. Willke *et al.* The GEO 600 gravitational wave detector. *Class. Quantum Grav.*, Vol. 19, pp. 1377–1387, 2002.
- [58] F. Bondu, A. Brillet, F. Cleva, H. Heitmann, M. Loupias, C. N. Man, H. Tringuet, and the VIRGO Collaboration. The VIRGO injection system. *Class. Quantum Grav.*, Vol. 19, pp. 1829–1833, 2002.
- [59] Thomas J. Kane and Robert L. Byer. Monolithic, unidirectional single-mode Nd:YAG ring laser. *Opt. Lett.*, Vol. 10, No. 2, pp. 65–67, 1985.
- [60] I. Freitag, A. Tünnermann, and H. Welling. Power scaling of diode-pumped monolithic Nd:YAG lasers to output powers of several watts. *Opt. Commun.*, Vol. 115, pp. 511–515, 1995.

- [61] O. Cregut, C. N. Man, D. Shoemaker, A. Brillet, A. Menhert, P. Peuser, N. P. Schmitt, P. Seller, and K. Wallmeroth. 18 W single-frequency operation of an injection-locked, CW, Nd:YAG laser. *Phys. Lett. A*, Vol. 140, No. 6, pp. 294–298, 1989.
- [62] I. Freitag, D. Golla, S. Knoke, W. Schöne, H. Zellmer, A. Tünnermann, and H. Welling. Amplitude and frequency stability of a diode-pumped Nd:YAG laser operating at a single-frequency continuous-wave output power of 20 W. *Opt. Lett.*, Vol. 20, No. 5, pp. 462–464, 1995.
- [63] Maik Frede, Ralf Wilhelm, René Gau, Martina Brendel, Ivo Zawischa, Carsten Fallnich, Frank Seifert, and Benno Willke. High-power single-frequency Nd:YAG laser for gravitational wave detection. *Class. Quantum Grav.*, Vol. 21, pp. S895–S901, 2004.
- [64] Maik Frede, Ralf Wilhelm, Martina Brendel, Carsten Fallnich, Frank Seifert, Benno Willke, and Karsten Danzmann. High power fundamental mode Nd:YAG laser with efficient birefringence compensation. *Opt. Exp.*, Vol. 12, No. 15, pp. 3581–3589, 2004.
- [65] Russell F. Teehan, Joshua C. Bienfang, and Craig A. Denman. Power scaling and frequency stabilization fo an injection-locked Nd:YAG rod laser. *Appl. Opt.*, Vol. 39, No. 18, pp. 3076–3084, 2000.
- [66] Kohei Takeno, Takafumi Ozeki, Shigenori Moriwaki, and Norikatsu Mio. Development of a high-power laser source for large-scale cryogenic gravitational wave telescope. In *Conference on Lasers and Electro-Optics/Quantum Electronics and Laser Science and Photonic Applications, Systems and Technologies 2005*. Optical Society of America, Washington, DC, 2005. CMA2.
- [67] Kohei Takeno, Takafumi Ozeki, Shigenori Moriwaki, and Norikatsu Mio. 100 W, single-frequency operation of an injection-locked Nd:YAG laser. *Opt. Lett.*, Vol. 30, No. 16, pp. 2110–2112, 2005.
- [68] The MOPA system was reported by W. Wiechmann *et al.* at the Conference on Lasers and Electro-Optics (Optical Society of America, Washington, DC, 1998).
- [69] S. Höfer, A. Liem, J. Limpert, H. Zellmer, A. Tünnermann, S. Unger, S. Jetschke, H.-R. Müller, and I. Freitag. Single-frequency master-oscillator fiber power amplifier system emitting 20 W of power. *Opt. Lett.*, Vol. 25, No. 17, pp. 1326–1328, 2001.
- [70] A. Liem, J. Limpert, H. Zellmer, and A. Tünnermann. 100-W single-frequency master-oscillator fiber power amplifier. *Opt. Lett.*, Vol. 17, pp. 1537–1539, 2003.
- [71] Y. Jeong, J. Nilsson, J. K. Sahu, D. B. S. Soh, C. Alegria, P. Dupriez, C. A. Codemard, D. N. Payne, R. Horley, L. M. B. Hickey, L. Wanzcyk, C. E. Chryssou, J. A. Alvarez-Chavez, and P. W. Turner. Single-frequency, single-mode, plane-polarized ytterbium-doped fiber master oscillator power amplifier source with 264 W of output power. *Opt. Lett.*, Vol. 30, No. 5, pp. 459–462, 2005.
- [72] Tso Yee Fan and Robert L. Byer. Diode laser-pumped solid-state lasers. *IEEE J. Quantum Electron.*, Vol. 24, No. 6, pp. 895–912, 1988.
- [73] Ch. Salomon, D. Hils, and J. L. Hall. Laser stabilization at the millihertz level. *J. Opt. Soc. Am. B*, Vol. 5, No. 8, pp. 1576–1587, 1988.

- [74] J. Helmcke, S. A. Lee, and J. L. Hall. Dye laser spectrometer for ultrahigh spectral resolution: design and performance. *Appl. Opt.*, Vol. 21, No. 9, pp. 1686–1694, 1982.
- [75] J. Hough, D. Hils, M. D. Rayman, Ma. L.-S., L. Hollberg, and J. L. Hall. Dye-laser frequency stabilization using optical resonators. *Appl. Phys. B*, Vol. 33, pp. 179–185, 1984.
- [76] N. Uehara and K. Ueda. Ultrahigh-frequency stabilization of a diode-pumped Nd:YAG laser with a high-power-acceptance photodetector. *Opt. Lett.*, Vol. 19, No. 10, pp. 728–730, 1994.
- [77] K. Nakagawa, T. Katsuda, and M. Ohtsu. Short-term frequency stabilization of diode-laser-pumped Nd:YAG lasers using double-pendulum suspended cavities. *Appl. Phys. B*, Vol. 60, pp. 489–494, 1995.
- [78] F. Bondu, P. Fritschel, C. N. Man, and A. Brillet. Ultrahigh-spectral-purity laser for the VIRGO experiment. *Opt. Lett.*, Vol. 21, No. 8, pp. 582–584, 1996.
- [79] Mitsuru Musha, Ken'ichi Nakagawa, and Ken-ichi Ueda. Wideband and high frequency stabilization of an injection-locked Nd:YAG laser to a high-finesse Fabry-Perot cavity. *Opt. Lett.*, Vol. 22, No. 15, pp. 1177–1179, 1997.
- [80] D. J. Ottaway, P. J. Veitch, C. Hollitt, D. Mudge, M. W. Hamilton, and J. Munch. Frequency and intensity noise of an injection-locked Nd:YAG ring laser. *Appl. Phys. B*, Vol. 71, pp. 163–168, 2000.
- [81] M. Musha, T. Kanaya, K. Nakagawa, and K. Ueda. Intensity and frequency noise characteristics of two coherently-added injection-locked Nd:YAG lasers. *Appl. Phys. B*, Vol. 73, pp. 209–214, 2001.
- [82] Kohei Takeno. Development of a high-power, stable laser for gravitational wave detection. Master's thesis, University of Tokyo, 2002. (in Japanese).
- [83] H. Kogelnik and T. Li. Laser beams and resonators. *Appl. Opt.*, Vol. 5, No. 10, pp. 1550–1567, October 1966.
- [84] Susumu Konno. *Study of high-power, LD-pumped solid-state lasers*. Ph.D. dissertation, University of Tokyo, 2002. (in Japanese).
- [85] L. M. Osterink and J. D. Foster. Thermal effects and transverse mode control in a Nd:YAG laser. *Appl. Phys. Lett.*, Vol. 12, No. 4, pp. 128–131, 1968.
- [86] W. C. Scott and M. de Wit. Birefringence compensation and TEM₀₀ mode enhancement in a Nd:YAG laser. *Appl. Phys. Lett.*, Vol. 18, No. 1, pp. 3–4, 1971.
- [87] W. A. Clarkson, N. S. Felgate, and D. C. Hanna. Simple method for reducing the depolarization loss resulting from thermally induced birefringence in solid-state lasers. *Opt. Lett.*, Vol. 24, No. 12, pp. 820–822, 1999.
- [88] Q. Lü, N. Kugler, H. Weber, S. Dong, N. Müller, and U. Wittrock. A novel approach for compensation of birefringence in cylindrical Nd:YAG rods. *Opt. Quantum Elect.*, Vol. 28, pp. 57–69, 1996.

- [89] Jean-Charles Cotteverte, Guy Ropars, Albert Le Floch, and Fabien Bretenaker. Polarization dragging in injected lasers. *IEEE J. Quantum Electron.*, Vol. 30, No. 11, pp. 2516–2525, 1994.
- [90] Shuichi Fujikawa, Tetsuo Kojima, and Koji Yasui. High-power and high-efficiency operation of a cw-diode-side-pumped Nd:YAG rod laser. *IEEE J. Sel. Top. Quantum Electron.*, Vol. 3, No. 1, pp. 40–44, 1997.
- [91] Tetsuo Kojima and Koji Yasui. Efficient diode side-pumping configuration of a Nd:YAG rod laser with a diffusive cavity. *Appl. Opt.*, Vol. 36, No. 21, pp. 4981–4984, 1997.
- [92] Susumu Konno, Shuichi Fujikawa, and Koji Yasui. 80 W cw TEM₀₀ 1064nm beam generation by use of a laser-diode-side-pumped Nd:YAG rod laser. *Appl. Phys. Lett.*, Vol. 70, No. 20, pp. 2650–2651, 1997.
- [93] Susumu Konno, Shuichi Fujikawa, and Koji Yasui. 206W continuous-wave TEM₀₀ mode 1064nm beam generation by a laser-diode-pumped Nd:YAG rod laser amplifier. *Appl. Phys. Lett.*, Vol. 79, No. 17, pp. 2696–2697, 2001.
- [94] Eugene Hecht. *Optics*. Addison Wesley Longman, third edition, 1998.
- [95] Alejandro D. Farinas, Eric K. Gustafson, and Robert L. Byer. Frequency and intensity noise in an injection-locked, solid-state laser. *J. Opt. Soc. Am. B*, Vol. 12, No. 2, pp. 328–334, 1995.
- [96] R. Loudon, M. Harris, T. J. Shepherd, and J. M. Vaughan. Laser-amplifier gain and noise. *Phys. Rev. A*, Vol. 48, No. 1, pp. 681–701, 1993.
- [97] J. Jahanpanah. Stability theory of class-C (far-infrared) lasers with an injected signal. *J. Opt. Soc. Am. B*, Vol. 22, No. 4, pp. 680–688, 2005.
- [98] J. Jahanpanah and R. Loudon. Theory of laser-amplifier injection locking. *Phys. Rev. A*, Vol. 54, No. 6, pp. 5210–5226, 1996.
- [99] Timothy Day, Eric K. Gustafson, and Robert L. Byer. Sub-hertz relative frequency stabilization of two-diode laser-pumped Nd:YAG lasers locked to a Fabry-Perot interferometer. *IEEE J. Quantum Electron.*, Vol. 28, No. 4, pp. 1106–1117, 1992.
- [100] Eric Black. Note on the Pound-Drever-Hall technique, 1998. Technical Note of the LIGO project, LIGO-T980045-00-D.
- [101] Max Born and Emil Wolf. *Principles of Optics*. Cambridge, 7th (expanded) edition, 2001.
- [102] Robert Herloski. Strehl ratio for untruncated aberrated Gaussian beams. *J. Opt. Soc. Am. A*, Vol. 2, No. 7, pp. 1027–1030, 1985.
- [103] Virendra N. Mahajan. Strehl ratio of a Gaussian beam. *J. Opt. Soc. Am. A*, Vol. 22, No. 9, pp. 1824–1833, 2005.
- [104] J. Y. Wang and D. E. Silva. Wave-front interpretation with Zernike polynomials. *Appl. Opt.*, Vol. 19, No. 9, pp. 1510–1518, 1980.

- [105] D. J. Ottaway, P. J. Veitch, M. W. Hamilton, C. Hollitt, D. Mudge, and J. Munch. A compact injection-locked Nd:YAG laser for gravitational wave detection. *IEEE J. Quantum Electron.*, Vol. 34, No. 10, pp. 2006–2009, 1998.
- [106] Noboru Uehara. *Ultrahigh frequency stabilization and high power solid state laser for gravitational wave detection*. Ph.D. dissertation, University of Electro-Communications, 1996.
- [107] Thomas J. Kane, Alan C. Nilsson, and Robert L. Byer. Frequency stability and offset locking of a laser-diode-pumped Nd:YAG monolithic nonplanar ring oscillator. *Opt. Lett.*, Vol. 12, No. 3, pp. 175–177, 1987.
- [108] Peter Fritschel, Andrew Jeffries, and Thomas J. Kane. Frequency fluctuations of a diode-pumped Nd:YAG ring laser. *Opt. Lett.*, Vol. 14, No. 18, pp. 993–995, February 1989.
- [109] B. Willke, S. Brozek, K. Danzmann, V. Quetschke, and S. Gossler. Frequency stabilization of a monolithic Nd:YAG ring laser by controlling the power of the laser-diode pump source. *Opt. Lett.*, Vol. 25, No. 14, pp. 1019–1021, 2000.
- [110] Shigeo Nagano and Shigenori Moriwaki. Seismic isolation for the input and output optics, 2005. Internal document of the LCGT project, available at <http://www.icrr.u-tokyo.ac.jp/gr/plans.html>, (in Japanese).
- [111] Takao Kobayashi, editor. *Solid-state lasers*. Academic Press Center, 1997. (in Japanese).
- [112] Laser society of Japan, editor. *Laser handbook*. Ohmsha, second edition, 2005. (in Japanese).
- [113] T. Dascalu, N. Pavel, and T. Taira. 90 W continuous-wave diode edge-pumped microchip composite Yb:Y₃Al₅O₁₂ laser. *Appl. Phys. Lett.*, Vol. 83, No. 20, pp. 4086–4088, 2003.
- [114] A. Minassian and M. J. Damzen. 20 W bounce geometry diode-pumped Nd:YVO₄ laser system at 1342 nm. *Opt. Commun.*, Vol. 230, pp. 191–195, 2004.
- [115] Masaki Tsunekane, Traian Dascalu, and Takunori Taira. High-power, diode edge-pumped, single-crystal Yb:YAG/ ceramic yag composite microchip Yb:YAG laser for material processing. In *Conference on Lasers and Electro-Optics/Quantum Electronics and Laser Science and Photonic Applications, Systems and Technologies 2005*. Optical Society of America, Washington, DC, 2005. CTuZ3.
- [116] T. Y. Fan. Heat generation in Nd:YAG and Yb:YAG. *IEEE J. Quantum Electron.*, Vol. 29, No. 6, pp. 1457–2566, 1993.
- [117] Juanren Lu, Mahendra Prabhu, Ken-ichi Ueda, Hideki Yagi, Takakimi Yanagitani, and Alexander A. Kaminskii. Highly efficient 2% Nd:yttrium aluminum garnet ceramic laser. *Appl. Phys. Lett.*, Vol. 77, No. 23, pp. 3707–3709, 2000.
- [118] Juanren Lu, T. Murai, K. Takaichi, T. Uematsu, K. Misawa, M. Prabhu, J. Xu, H. Yagi, T. Yanagitani, A. A. Kaminskii, and A. Kudryashov. 72w Nd:Y₃Al₅O₁₂ ceramic laser. *Appl. Phys. Lett.*, Vol. 78, No. 23, pp. 3586–3588, 2001.
- [119] W A Clarkson. Thermal effects and their mitigation in end-pumped solid-state lasers. *J. Phys. D*, Vol. 34, pp. 2381–2395, 2001.

- [120] Norman Hodgson, Shalei Dong, and Qitao Lü. Performance of a 2.3kW Nd:YAG slab laser system. *Opt. Lett.*, Vol. 18, No. 20, pp. 1727–1729, 1993.
- [121] R. J. Shine, Jr., A. J. Alfrey, and R. L. Byer. 40-W cw, TEM₀₀-mode, diode-laser-pumped, Nd:YAG miniature-slab laser. *Opt. Lett.*, Vol. 20, No. 5, pp. 459–461, March 1995.
- [122] K. Tei, M. Kato, Y. Niwa, S. Harayama, Y. Maruyama, T. Matoba, and T. Arisawa. Diode-pumped 250-W zigzag slab Nd:YAG oscillator-amplifier system. *Opt. Lett.*, Vol. 23, No. 7, pp. 514–516, 1998.
- [123] Todd S. Rutherford, William M. Tulloch, Eric K. Gustafson, and Robert L. Byer. Edge-pumped quasi-three-level slab lasers design and power scaling. *IEEE J. Quantum Electron.*, Vol. 36, No. 2, pp. 205–219, 2000.
- [124] T. S. Rutherford, W. M. Tulloch, S. Sinha, and R. L. Byer. Yb:YAG and Nd:YAG edge-pumped slab lasers. *Opt. Lett.*, Vol. 25, No. 13, pp. 986–988, 2001.
- [125] Gregory D. Goodno, Stephen Palese, Joseph Harkenrider, and Hagop Injeyan. Yb:YAG power oscillator with high brightness and linear polarization. *Opt. Lett.*, Vol. 26, No. 21, pp. 1672–1674, 2001.
- [126] Elektronik Laser System manufactures Yb:YAG disc lasers named VersaDisk, details are available at <http://www.els.de/Products/vdisk.html>.